POLITECNICO DI TORINO

Master of Science in
Aerospace Engineering

Numerical and experimental comparison between a convergent and a convergent-divergent primary nozzle for a supersonic axisymmetric ejector

In collaboration with the
von Karman Institute for Fluid Dynamics

Supervisors:
Prof. Gioacchino Cafiero
Prof. Miguel Alfonso Mendez
Ph.D. Jan Van den Berghe

Student:
Tani Angiero

Academic Year 2022/2023

Abstract

Supersonic ejectors are simple devices which require limited maintenance that provide a combined effect of compression, mixing and entrainment without moving parts and without limitations concerning working fluids. Despite their simplicity, complex fluid dynamics phenomena occur in these devices, such as shear layer, shock train, turbulent mixing.

This study investigates the performance of a supersonic ejector for two primary nozzle configurations: convergent and convergent-divergent nozzle. To achieve this purpose, we conduct an experimental campaign for the convergent primary nozzle ejector configuration. Then, analytical and numerical models are used to compare the collected data. A CFD study is performed for the two geometries to compare the performance of the performances for the two different configurations.

The CFD results show that a convergent-divergent primary nozzle configuration leads to lower entrainment ratios than a simple convergent one on equal work conditions for the selected test cases. The outcomes obtained enrich the research in alternative energy conversion technologies to identify the most efficient configuration for a supersonic ejector to reduce the environmental and economic impact.

Contents

List of Abbreviations and Symbols

List of Figures

List of Tables

1 Introduction **1**
- 1.1 Context . . . 1
  - 1.1.1 Scope of the Study . . . 1
- 1.2 Ejector Fundamentals . . . 2
  - 1.2.1 Operational Characteristics . . . 4
  - 1.2.2 Flow Regimes and Internal Structures . . . 5
- 1.3 Conclusion . . . 9

2 Experimental Study: Convergent Primary Nozzle **10**
- 2.1 Experimental Set-up . . . 10
  - 2.1.1 Multi-Parameter Mass Flow Meters . . . 13
    - 2.1.1.1 Temperature . . . 14
    - 2.1.1.2 Pressure . . . 15
    - 2.1.1.3 Velocity . . . 15
  - 2.1.2 Thermocouples . . . 17
  - 2.1.3 Pressure Sensors . . . 18
    - 2.1.3.1 Calibration . . . 19
- 2.2 Experimental Campaign . . . 21
  - 2.2.1 Data Acquisition. . . . 22
  - 2.2.2 Post-Processing . . . 23
    - 2.2.2.1 Uncertainty Analysis . . . 23
    - 2.2.2.2 Error Propagation . . . 26
    - 2.2.2.3 Variables on Interest . . . 28
    - 2.2.2.4 Normalized Mass Flows . . . 28
  - 2.2.3 Results . . . 29

3 Analytical Model **33**
3.1 Thermodynamic Model Review . . . 34
3.2 Assumptions and Algorithm . . . 35
3.3 On-Design Thermodynamic Model . . . 36
3.3.1 Primary Nozzle . . . 37
3.3.2 Mixing Chamber . . . 38
3.3.2.1 Fabri-Choking . . . 38
3.3.2.2 Compound-Choking . . . 39
3.4 Off-Design Thermodynamic Model . . . 40
3.5 Results . . . 42
3.5.1 Effect of the Velocity at the Outlet . . . 43
3.6 Comparison between experimental data and analytical model . 46
3.6.1 Thermodynamic Model Calibration . . . 46
3.6.1.1 Global Fitting . . . 48
3.7 Conclusion . . . 49

4 CFD Analysis **51**
4.1 Introduction . . . 51
4.1.1 Physics of the Problem . . . 52
4.1.2 Computational Method . . . 53
4.2 Pre-processing . . . 54
4.2.1 Mesh Generation . . . 54
4.2.2 Numerical Solver . . . 57
4.2.3 Control . . . 60
4.2.4 Boundary and Initial Conditions . . . 61
4.2.4.1 Pressure . . . 62
4.2.4.2 Velocity . . . 63
4.2.4.3 Temperature . . . 63
4.2.4.4 Turbulent Kinetic Energy . . . 63
4.2.4.5 Specific Turbulence Dissipation . . . 64
4.2.5 Grid Convergence . . . 64
4.3 Results . . . 67
4.3.1 Flow topology features . . . 69

5 Conclusion **75**

A Analytical Model **81**
A.1 Listing: Metsue's 0D thermodynamic model Python code . . . 81
A.2 On-Design Model . . . 88
A.3 Off-Design Model . . . 90
A.4 Velocity Outlet Diffuser . . . 91

B Experimental Study **92**
B.1 Calibration Curve Pressure Transducers. 92
B.2 Error Propagation in the measuring chain. 92
B.3 Normalized Mass Flow Rate 94

List of Abbreviations and Symbols

Abbreviations

VKI	Von Karman Institute
ER	Entrainment Ratio
CFD	Computational Fluid Dynamics
RANS	Reynolds-Averaged Navier–Stokes equations
NXP	Nozzle Exit Position
CPM	Constant-Pressure Mixing ejector
CAM	Constant-Area Mixing ejector
PRTD/RTD	Platinum/Resistance Temperature Detector sensor
RC	Resistance-Capacitance
DPI	Digital Pressure Indicator
TC	Thermocouple
FV	Finite Volume method
CFL	Courant–Friedrichs–Lewy condition
C/CD	Convergent/ Convergent-Divergent primary nozzle
U.M.	Units of Measurement
BL	Boundary Layer
BC	Boundary Condition

Alpha numeric symbols

D_t	Primary Nozzle Throat Section	$[m]$
D_e	Primary Nozzle Exit Section	$[m]$
D_d	Diffuser Exit Section	$[m]$
D_m	Constant-area Mixing Section Exit Section	$[m]$
L_m	Constant-area Mixing Section Exit Length	$[m]$

θ	Nozzle Exit Area Ratio	$[-]$
$p_{p,0}$	Primary Flow Total Pressure	$[Pa]$
$T_{p,0}$	Primary Flow Total Temperature	$[K]$
p_p	Primary Flow Static Pressure	$[Pa]$
T_p	Primary Flow Static Temperature	$[K]$
$p_{s,0}$	Secondary Flow Total Pressure	$[Pa]$
$T_{s,0}$	Secondary Flow Total Temperature	$[K]$
p_s	Secondary Flow Static Pressure	$[Pa]$
T_s	Secondary Flow Static Temperature	$[K]$
$\dot{m}_p$	Primary Mass Flow Rate	$[kg/s]$
$\dot{m}_s$	Secondary Mass Flow Rate	$[kg/s]$
ω	Entrainment Ratio	$[-]$
p^*_{out}	Critical Outlet Static Pressure	$[Pa]$
p_{BD}	Breakdown Static Pressure	$[Pa]$
η_p	Primary Nozzle Isentropic Efficiency	$[-]$
η_s	Secondary Nozzle Isentropic Efficiency	$[-]$
η_{py}	Mixing Losses Factor	$[-]$
η_m	Mixing Chamber Isentropic Efficiency	$[-]$
η_d	Diffuser Isentropic Efficiency	$[-]$
h_0	Total Enthalpy	$[J/kg]$
h	Specific Enthalpy	$[J/kg]$
G	Mass Flux	$[kg/(m^2 \cdot s)]$
M	Mach Number	$[-]$
Re	Reynolds Number	$[-]$
St	Strouhal Number	$[-]$
C_f	Skin Fritcion	$[-]$
ρ	Mass Density of Fluid	$[kg/m^3]$
$\boldsymbol{U}$	Velocity Vector Field	$[m/s]$
V	Longitudinal Velocity Component	$[m/s]$
μ	Dynamic Viscosity	$[kg/m \cdot s]$
ν	Kinematic Viscosity	$[m^2 \cdot s]$
f_s	Vortex Shedding Frequency	$[Hz]$
d_s	Shedder Bar Width	$[m]$
R	Gas Constant	$[J/(kg \cdot K)]$
R_T	Resistence od the sensor at temperature T $[^\circ C]$	$[\Omega]$
α	Temperature-Dependent Resistance	$[\Omega/\Omega \cdot^\circ C]$
k_T	Calibration Constant	$[bar/V]$
γ	Specific Heats Ratio	$[-]$
$c_p,\ c_v$	Specific heat capacity at constant pressure/volume	$[J/(kg \cdot K)]$
E	Total Energy Density	$[J/kg]$
e	Specific Internal Energy	$[J/kg]$

k	Turbulence Kinetic Energy	$[J/kg]$
$\boldsymbol{I}$	Identity Matrix	$[-]$
Pr	Prandtl Number	$[-]$
u_*	Friction/Shear Velocity	$[m/s]$
y^+	Dimensionless Wall Distance	$[-]$
$\underline{\boldsymbol{\tau}}$	Viscous Stress Tensor	$[N/m^2]$
τ_w	Wall Shear Stress	$[N/m^2]$
$\underline{\boldsymbol{D}}$	Deformation Gradient Tensor	$[\cdot/t]$
$\boldsymbol{q}$	Heat Flux	$[W/m^2]$
A_s	Sutherland Coefficient	$[kg \cdot \sqrt{K}/(m \cdot s)]$
T_s	Sutherland Temperature	$[K]$
H_f	Heat Fusion	$[J/kg]$

Subscripts

t	Primary Nozzle Throat Section
e	Primary Nozzle Exit Section
m	Mixing Section
N	Normal Shock Section
2	Downstream Normal Shock/Inlet Diffuser Section
d	Diffuser Exit Section
out	Outlet of Ejector

Operators

$\bar{\cdot}$	Time Average
$\cdot'$	Time Fluctuation
$\hat{\cdot}$	Normalized Value
$\boldsymbol{\nabla}(\cdot)$	Gradient
$\boldsymbol{\nabla} \cdot (\cdot)$	Divergence
$dev(\cdot)$	Deviator Component
$tr(\cdot)$	Trace

List of Figures

1.1 Geometry of the ejector. [Reprinted from *"Numerical Investigation of Miniature Ejector Refrigeration System Embedded with a Capillary Pump Loop"*, by Dong J., Song H., Yu M., Yu M.G. and Wang W.N. [5]. © Copyright 2008-2023 by ResearchGate GmbH.] 3
1.2 Ejector theoretical characteristic curve. 5
1.3 Flow regimes in a supersonic nozzle: (a) unprimed nozzle flow; (b) over-expanded flow; (c) under-expanded flow. [Reprinted from *"Etude numérique et expérimentale de l'interaction entre deux écoulements compressibles dans un éjecteur supersonique"*, by Bouhanguel A. [10]. Université de Franche-Comté, 2013.] 6
1.4 Internal ejector flow structures: (a) Fully developed supersonic flow; (b) Supersonic flow with secondary sonic throat; (c) Supersonic saturated regime; (d) Supersonic regime with double choking. [Reprinted from *"Current Advances in Ejector Modeling, Experimentation and Applications for Refrigeration and Heat Pumps"*, by Aidoun, Z., Ameur, K., Falsafioon, M. and Badache, M. [2]. © Copyright 1996-2023 by MDPI.] 8

2.1 Convergent Primary Nozzle. 10
2.2 Von Karman Institute bench test for supersonic ejector. 12
2.3 Supersonic ejector: Convergent primary nozzle. 13
2.4 Heinrichs Series DVH in-line Mass Flow Meters. 14
2.5 Reynolds Number Range. [Reprinted from "Vortex Flow Meter: Instruction Manual", by Heinrichs KOBOLD Group [14]. © Copyright by HEINRICHS Messtechnik GmbH.] 16
2.6 Primary Inlet Flow Sensors. 17
2.7 DP15 Validyne Differential Pressure Transducer. [Reprinted from "DP15 Variable Reluctance Differential Pressure transducer: Instruction Manual" [15]. © Copyright by Validyne Engineering. 18

2.8 DPI 601 Digital Pressure Indicator. 19
2.9 "Validyne 1" Curve Calibration. 21
2.10 "Validyne 1" Usage Curve. 22
2.11 Primary static pressure time series for "Test100". 25
2.12 PDF Primary static pressure for "Test100". 26
2.13 Primary static temperature time series for "Test100". 27
2.14 Results of the experimental campaign for convergent primary nozzle configuration 30
2.15 Normalized Mass Flows. 32

3.1 Schematic diagram of the model (top half). [Reprinted from *"An improved thermodynamic model for supersonic real-gas ejectors using the compound-choking theory"*, by Metsue A., Debroeyer R., Poncet S., Bartosiewicz Y. [4]. © Copyright 2023 by Elsevier B.V.] 36
3.2 Schematic diagram for the model of Fabri-choking. [Reprinted from "Numerical and experimental evidence of the Fabri-choking in a supersonic ejector", by Lamberts O., Chatelain P., Bartosiewicz Y. [21]. © Copyright 2018 by International Journal of Heat and Fluid Flow] 39
3.3 Illustration of the streams considered in the compound-choking theory. [Reprinted from *"The compoundchoking theory as an explanation of the entrainment limitation in supersonic ejectors."*, by O.Lamberts, P.Chatelain, N.Bourgeois, and Y.Bartosiewicz. © Copyright 2023 by Elsevier B.V.] 40
3.4 0D Model Operating Curves. 42
3.5 Comparison of the Fabri-choking and Compound-choking with the experiment. 44
3.6 Comparison between the operating curves (secondary flow maximization criterion) constructed for zero outlet velocity ["Case 1"] and non-zero outlet velocity ["Case 2"]. 45
3.7 Influence of losses factors on the characteristic curve. 47
3.8 Comparison entrainment ratios between experimental and theoretical data. 48
3.9 Comparison entrainment ratios Data for only choked operational conditions. 50

4.1 Geometry Domain Detail: (a) Convergent Primary Nozzle Configuration; (b) Convergent-Divergent Primary Nozzle Configuration. 54

4.2 Turbulent boundary layer for a typical incompressible flow over a smooth flat plate showing various layers. [Reprinted from *"Numerical and experimental investigations of the noise and performance characteristics of a radial fan with forward-curved blades"*, by Darvish M. [34]. © Copyright 2023 by ResearchGate GmbH.] 55
4.3 y^+ close to wall for "Test012". 58
4.4 An overall vision and detail of the grid structure of the computational domain for the numerical simulations: (a) Convergent Primary Nozzle; (b) Convergent-Divergent Primary Nozzle. . . 59
4.5 Centerline Mach number for "Test012". 66
4.6 CFD Results for C and CD configurations compared with experimental data. 68
4.7 Upper half: Mean-flow Mach number field and sonic line for Convergent configuration. Lower half: Mean-flow Mach number field and sonic line for Convergent-Divergent configuration. 71
4.8 Numerical schlieren (axial derivative of the density field) image of the flow. Shock-wave and compression regions are shown in dark, expansion fans and regions are shown in light. Upper half: Convergent configuration. Lower half: Convergent-Divergent configuration. 72
4.9 Numerical schlieren (radial derivative of the density field) image of the flow. The shear layers are shown in light. Upper half: Convergent configuration. Lower half: Convergent-Divergent configuration. 73
4.10 Primary nozzle and secondary pipe exit flow fields for "Test012". Exit primary nozzle (CD): $[0; 15]\,mm$; Exit secondary pipe (CD): $[17.02; 30]\,mm$ Exit primary nozzle (C): $[0; 14]\,mm$; Exit secondary pipe (C): $[16.02; 30]\,mm$ Solid Line: C configuration; Dash Line: CD configuration. 74

A.1 Flowchart of the model for on-design operation using the Fabri-choking criterion. 88
A.2 Flowchart of the model for on-design operation using the compound-choking criterion. 89
A.3 Flowchart of the model for off-design operation conditions. . . 90
A.4 Flowchart of "Case 1" and "Case 2" for the diffuser outlet velocity. 91

B.1 Calibration Curve: (a) "Validyne 2"; (b) "Valydine 3". 92
B.2 Normalized Mass Flows for $p_{s,0}/p_{p,0} = 0.90$. 94

List of Tables

2.1 DP15 Validyne Specifications 19
2.2 Pressure-Voltage calibration data. 20
2.3 "Test001" Calibration parameters. 23
2.4 Sampling Parameters. 24

3.1 Predictions of the entrainment ratio for the current ejector using the Fabri-choking and Compound-choking criterions. . . 43
3.2 Comparison of the diffuser exit conditions. 45

4.1 Overview of the hexahedra elements for the three mesh for C and CD primary nozzle configuration. 65
4.2 Input values for CFD simulations related to the experimental campaign (temperature u.m.: $[K]$; pressure u.m.: $[Pa]$; mass flow rate u.m.: $[kg/s]$). 67
4.3 Primary and secondary mass flow rates, and entrainment ratios from CFD results. 70

Chapter 1

Introduction

1.1 Context

Supersonic ejectors are devices widely used in the past century, but only in the last decade have they acquired particular interest due to the urgent need to reduce environmental impact.
An ejector is a passive device that utilizes high-stagnation conditions to expand a driving fluid, which, in turn, entrains and compresses a low-pressure secondary flow to an intermediate back pressure. This compression is achieved through the partial transfer of momentum occurring in the shear layer formed between the two streams. Additionally, other gas dynamics interactions, such as shock waves and expansion waves, may also occur.
Considering the absence of moving parts and the simple production, they become an attractive alternative to other more complex devices. Ejectors are virtually maintenance-free, and their operating costs are significantly lower due to the absence of electrical power consumption, unlike compressors. For these reasons, ejectors have found many applications in engineering including refrigeration systems [1] and heat pumps in industrial, aeronautical and aerospace sectors [2].
The recent interest in these devices has led to numerous results in simulations and analytical models to optimize their geometry. Even though the structure is simple, decidedly complex fluid-dynamic phenomena occur inside the supersonic injectors, which depend on their internal geometry [3].

1.1.1 Scope of the Study

This study aims to investigate the performance of a supersonic ejector with a convergent and a convergent-divergent primary nozzle.

Ejector study is, however, still challenging due to the complex flow process taking place, such as supersonic conditions, shock wave formation, possible condensation and turbulent mixing of two streams in dynamic and thermal non-equilibrium in a very short time and restricted space.
For these reasons, in the following work, we employ a simplified analytically validated model, experiments and Computational Fluid Dynamics (CFD).

In the remainder of Chapter 1, we provide an overview of the subject under study and its key operational characteristics, emphasizing the fluid dynamic phenomena that impact the ejector's performance in the two examined configurations.

Following that general sight, Chapter 2 presents the results of the experimental campaign for the convergent primary nozzle configuration conducted at the von Karman Institute, Belgium.

In fact, the Chapter 3 offers a review of the main thermodynamic models found in the literature, as applied to supersonic ejectors, with particular focus on the analytical model implemented based on Metsue's 0D model [4], used in this work. At the end of that, we present a comparison of the theoretical operating curves with the experimental results obtained in the last Chapter 2.

Finally, the last Chapter 4 introduces the computation model and meshes employed to obtain the results of the CFD simulations, which are then compared for the two configurations and with the experimental values of the convergent configuration.

The final purpose of developing this work is to provide a comparison between the two ejector configurations using various approaches, leveraging the advantages of each and highlighting their respective drawbacks.

1.2 Ejector Fundamentals

The typical layout of an ejector is shown in Figure 1.1. The first main part is a nozzle that allows the primary fluid to reach high velocity. The second part is the suction pipe for the secondary fluid, the third is the mixing chamber and the last one is the diffuser.
Furthermore, depending on the relative position between the nozzle exit section and the constant area section of the mixing chamber, one generally distinguishes two different main layouts. If the primary nozzle lies in the converging part of the mixing pipe, it is called a *constant-pressure mixing* (CPM) ejector otherwise if it lies in the constant area section, it is termed *constant-air mixing* (CAM) one. The internal geometry of the nozzle is intrinsically linked to the performance of the ejector, therefore these two config-

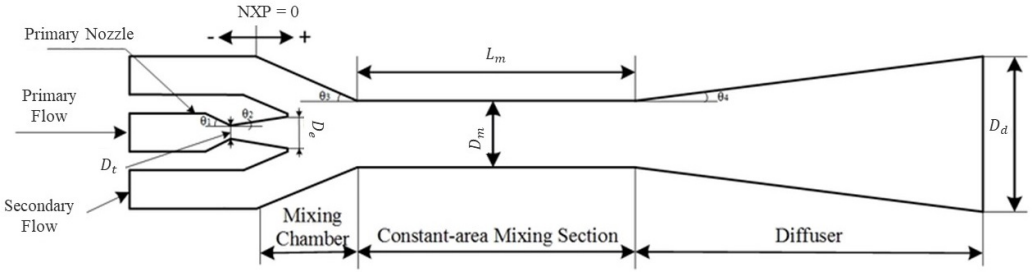

Figure 1.1: Geometry of the ejector.
[Reprinted from *"Numerical Investigation of Miniature Ejector Refrigeration System Embedded with a Capillary Pump Loop"*, by Dong J., Song H., Yu M., Yu M.G. and Wang W.N. [5]. © Copyright 2008-2023 by ResearchGate GmbH.]

urations will have different pressure contours. Extensive studies on constant area mixing (CAM) and constant pressure (CPM) ejectors concluded that constant pressure mixing improves the cooling effect, overall efficiency and coefficient of performance and reduces power consumption [6]. The nozzle exit position (NXP) then constitutes a prominent parameter of research to enhance ejector performance.
This study is focused on the Constant-Pressure Mixing ejector.
Generally, the primary flow is choked. The static pressure at the exit of the nozzle may differ from the surrounding pressure in the mixing chamber, which gives rise to a shock train (cf. an under- or over- expanded jet).
By the second connection point, the low-pressure flow is sucked into the suction chamber in which the driven flow causes a constriction driven by shear effects.
Provided that the velocities of the two flows are remarkably different, there is a significant momentum transfer, and the secondary flow velocity increases while the primary one decreases. Here, numerous fluid dynamic phenomena can occur due to under- or over-expanded primary flow, such as shock or expansion waves and their respective reflections on the duct walls, as illustrated in Section 1.2.2. At that point, the primary stream transfers partially its energy and momentum to the secondary stream through viscous shearing, leading to complex turbulent mixing phenomena. The mixing of the two flows takes place along the constant section zone, otherwise called the mixing section.
In normal working conditions, the mixed flow is generally supersonic and at least a shock wave occurs before the diffuser and due to the increase in the transversal area, a total pressure recovery occurs until the outlet section where the mixed flow has an intermediate pressure between the initial ones. If the conditions of the ejectors do not result in the formation of any shock-

waves before the beginning of the diffuser, the flow remains supersonic and expands along it, but the back pressure would have to be etremely low, so this never occurs in practice.

1.2.1 Operational Characteristics

The purpose of a supersonic ejector for fixed total primary pressure, $p_{p,0}$, is to drive a maximum amount of secondary fluid, at the highest possible back-pressure and with the lowest possible energy losses. Therefore, its performance is primarily determined by the induced secondary mass flow rate $\dot{m}_s$.
The performance of the ejector is inherently dependent on the operating conditions in which it is working, which can be categorized as *on-design* and *off-design* conditions. As previously introduced, a high energy (high stagnation conditions -pressure and temperature-) primary flow expands in a convergent/convergent–divergent nozzle to produce a sonic/supersonic jet, creating a zone of low pressure around its outlet and initiating secondary flow suction at lower pressure. Under these circumstances, since the signal cannot travel upstream, the primary nozzle is choked and it is only sensitive to its inlet conditions and it only depends on the reservoir conditions and the throat cross-section area. According to de Laval nozzle theory, it is well-known that under these conditions, the primary flow mass flow rate is at its maximum.
The primary high velocity jet carries the slow moving, low-pressure secondary flow at its boundary, transferring to it part of its energy by momentum exchange, mainly through shear effect but also by suction effect into the low pressure zone created by the primary flow.
If the secondary inlet and the outlet pressure conditions are favourable, the secondary stream accelerates until to reached sonic conditions, while mixing increases progressively. In this scenario, the secondary mass flow rate is also maximum and the ejector's operating conditions is in the so called *on-design*, *double-chocked* or *critical mode* condition, since both the flows are chocked. After that, ideally, both flows eventually complete mixing to form a unique stream before the end of the mixing chamber. The combined flow resulting from this process then undergoes recompression by going through a series of shock waves before the diffuser. At this point, the flow has become subsonic with a pressure increase across the shock waves. In the diffuser, the flow pressure increases by further deceleration to match the imposed back-pressure.
If the back pressure increases above the critical value, the secondary flow is not choked anymore. The ejector is in the *off-design* or *sub-critical mode* operation condition and only the primary flow is choked. The secondary mass

flow rate decreases decreases as the back pressure increases up to a point of ejector malfunction.

It is convenient and meaningful to use dimensionless quantities. Hence, to fully characterize the operating conditions, the variables $\Pi = p_{s,0}/p_{p,0}$ and $\tau = p_b/p_{p,0}$ are used, where p_b denotes the back pressure. The performance of the ejector is closely related to the mass flow rate $\dot{m}_s$, or more conveniently by the dimensionless entrainment ratio defined as $\omega = \dot{m}_s/\dot{m}_p$.
Introducing these dimensionless parameters, a typical operating curve of the ejector and its corresponding operating conditions are depicted in the Figure 1.2 for a fixed Π value.

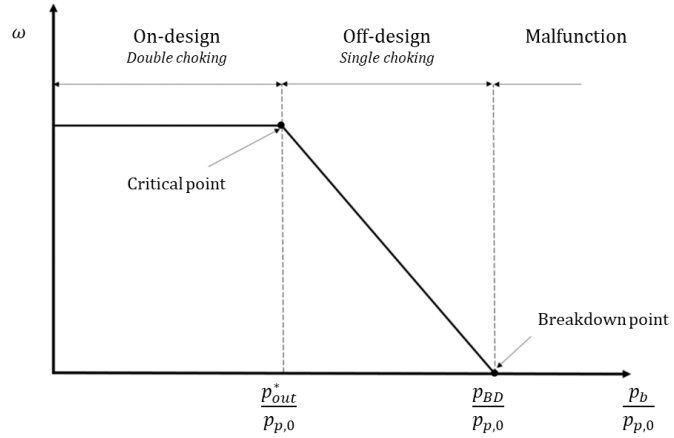

Figure 1.2: Ejector theoretical characteristic curve.

1.2.2 Flow Regimes and Internal Structures

In general, the internal geometry of the ejector depends on numerous factors [7], such as the configuration of the primary nozzle and its geometric characteristics. This one is typically expressed in terms of the nozzle exit area ratio defined as $\theta = (D_e/D_t)^2$, given by the ratio of cross-sectional areas. In Eames et al.' [8] study, ejectors with different θ values are tested, while keeping the throat section constant. It can be observed that for different exit areas, the ejector's performance, in terms of ω, changes under the same operating conditions.
In light of this result, it is immediately apparent that for the two different primary nozzle configurations under consideration, distinct performances are expected, all others operating conditions being equal.
As known from the canonical study of nozzles connected to a reservoir, widely

documented in the literature [9], a simply convergent nozzle exhibits always a increasing velocity and the pressure becomes lower along it. However, in the case of the divergent-convergent configuration of the primary nozzle, various flow regimes can occur. The three most common regimes, shown in Figure 1.3, that can occur in a supersonic ejector are well described by Bouhanguel [10] and depend on the pressure conditions:

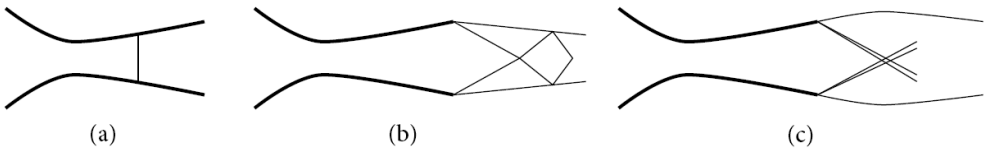

Figure 1.3: Flow regimes in a supersonic nozzle: (a) unprimed nozzle flow; (b) over-expanded flow; (c) under-expanded flow.
[Reprinted from *"Etude numérique et expérimentale de l'interaction entre deux écoulements compressibles dans un éjecteur supersonique"*, by Bouhanguel A. [10]. Université de Franche-Comté, 2013.]

(a) **Shockwave regime in the divergent section**. For low primary inlet pressure, the flow reaches $M = 1$ at the throat section, travels through a portion of the divergent section in supersonic flow, but due to the presence of the shockwave, the efflux from the nozzle is subsonic.

(b) **Over-expanded flow**. When the primary pressure increase, the efflux from the nozzle is supersonic, the pressure at the nozzle's exit section is lower than the ambient pressure, and the flow reaches ambient pressure outside the nozzle through an oblique shock wave.

(c) **Under-expanded flow**. The primary pressure further increases, the efflux from the nozzle is supersonic, the pressure at the nozzle exit section is higher than the ambient pressure, and the flow completes its expansion to ambient pressure outside the nozzle through an expansion fan.

When the exit pressure is slightly closed to the inlet pressure, the so-called Venturi regime can occur, where the flow is subsonic throughout the nozzle with a minimum in pressure (maximum in velocity and Mach number) at the throat section. However, this is an abnormal operating condition for ejectors.
Predicting the flow regime established in the ejector is significantly more challenging. If the flow at the exit of the primary nozzle is supersonic, various flow configurations can occur in the secondary nozzle depending on the

generating conditions and the geometry of the ejector. Several studies [11] [12], have thus highlighted the emergence of the different flow regimes inside the supersonic ejector.
The shaping of the primary stream at its outlet depends on the primary nozzle's operation, influenced by the expansion ratio determined by the primary and secondary inlet conditions. Specific ejector geometries and the overall operating conditions define the flow regimes in which the primary and secondary streams interact, leading to intricate flow patterns. Figure 1.4 shown the typical internal structures of an ejector, characterized by a pattern of expansion and compression waves with varying reflection angles.
Below are briefly described some of the notable cases [10]:

(a) **Supersonic Fully Developed Regime**. This regime occurs for high values of the generating pressure p_p and low induced flow rates ($\dot{m}_2$). Under these conditions, the primary stream fully expands within the mixing chamber. The secondary flow entrained by the primary jet is also in a supersonic regime.

(b) **Flow in which the secondary throat becomes sonic under supersonic conditions**. The expansion of the primary jet is less pronounced compared to the previous regime, and the induced flow is greater, resulting in sonic conditions in the mixing chamber at a point where the effective cross-sectional area is at its minimum. Beyond this point, both flows remain supersonic.

(c) **Saturated supersonic regime**. Also known as the *mixed regime*, it is characterized by a supersonic primary flow at the exit of the driving nozzle and a continuously subsonic secondary flow. This regime originates for moderately low values of the generating pressure p_p, which are insufficient to allow the supersonic initiation of the induced flow. A pseudo-shock is then localized between the exit of the primary nozzle and the throat of the ejector. It is worth noting that in the case of a flow regime separated in the primary nozzle (Figure1.3-(b)), this flow regime is referred to as the *separated mixed regime*.

(d) **Supersonic regime with double sonic throats**. The regime emerges for small values of the mixing chamber section in the ejector. The flow is characterized by the presence of a double sonic throat. This leads to the formation of two distinct pseudo-shocks, with the first one located at the exit of the primary nozzle and the second one forming at the exit of the mixing chamber and the entrance of the diffuser (Figure 1.4-(c)).

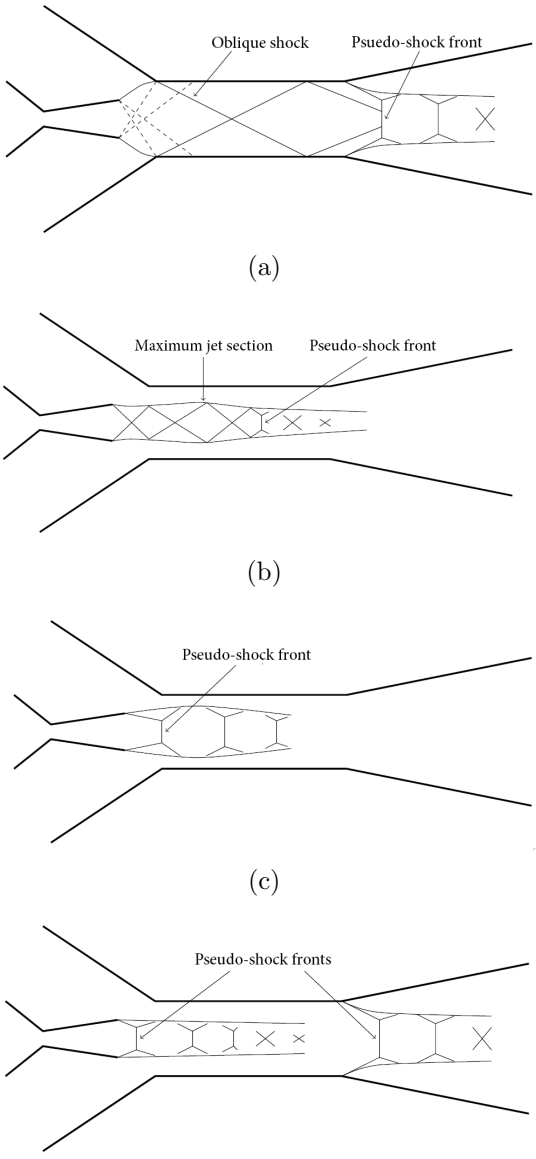

Figure 1.4: Internal ejector flow structures: (a) Fully developed supersonic flow; (b) Supersonic flow with secondary sonic throat; (c) Supersonic saturated regime; (d) Supersonic regime with double choking.
[Reprinted from *"Current Advances in Ejector Modeling, Experimentation and Applications for Refrigeration and Heat Pumps"*, by Aidoun, Z., Ameur, K., Falsafioon, M. and Badache, M. [2]. © Copyright 1996-2023 by MDPI.]

Along the mixing chamber, it takes plce a shock train of oblique waves that create high and low-pressure zones involving the secondary flow. Furthermore, in the case of strong interactions between the boundary layer and shocks, boundary layer separations can occur. These fluid dynamic structures influence the interaction between the primary and secondary flow and thus play a fundamental role in the overall performance of the ejector.
According to Matsuo's study [13], the presence of a single shockwave is unlikely due to the confinement of the flow within the ejector structure.

1.3 Conclusion

In this first Chapter, a comprehensive overview of the subject under study and its primary operating conditions is presented. These operating conditions are appropriately described by dimensionless parameters (ω, Π, τ), which will be extensively discussed in the upcoming chapters as they effectively represent the performance of an ejector.
Additionally, a general insight into the fluid dynamic structures that can develop within an ejector and their implications on the device's entrainment (ω) capacity based on pressure values (Π, τ) and a general insight has been provided into internal geometric characteristics.

Chapter 2

Experimental Study: Convergent Primary Nozzle

2.1 Experimental Set-up

In general, in the experimental approach, reference is made to a real physical experiment or a scaled model to conduct measurements of fluid dynamic quantities relevant for the study of a specific problem. In the present case, the quantities of interest pertain to the mass flow rates and the static pressure in the mixing pipe under static conditions of the two involved flows, while imposing the static pressures of both the primary and secondary flows, along with their respective temperatures, and the backward static pressure. The test rig in question was designed and constructed at the Von Karman Institute.

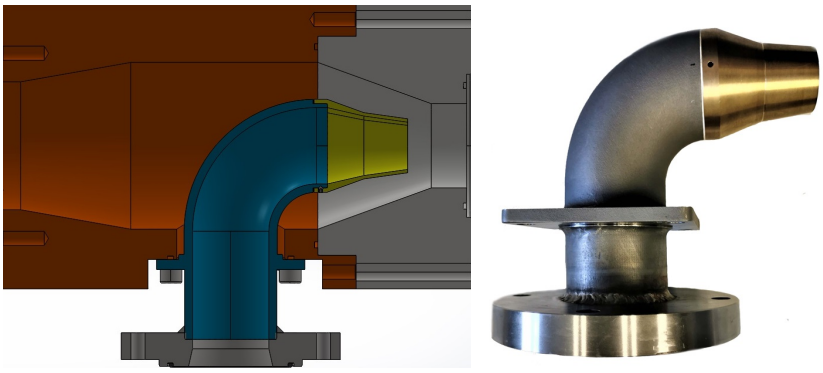

(a) (b)

Figure 2.1: Convergent Primary Nozzle.

The schematic diagram of the test rig for static measurements is depicted in Figure 2.2. The experimental test bench comprises the following components:

1. **Dry air compressor**: the compressor allows a dry compressed air generation system that allows storing a significant amount of compressed air up to 7 bar in an external tank. This system consists of the power generator, the dryer, and the compressor. The dryer is a special type of filtration system designed specifically for removing water from compressed air. The presence of the dryer is crucial because removing water vapor from the compressed air prevents condensation in the tank, pipes, hoses, and tools connected downstream from the compressor, which can be damaging, and it prevents moisture from interfering in sensitive industrial processes.
2. **Connectors and valves**:these allow the passage of air into the facility of interest and its proper branching into the two lines, the primary one and the secondary one.
3. **Pressure Regulators**: Aircom R11 Piloted Pressure Regulators are installed, which are a heavy-duty, rugged regulator that provides accurate pressure regulation. They are ideally suited to handle the most demanding industrial applications. This pilot-operated regulator can be controlled remotely. It is ideal for continuous high-capacity requirements where reduced pressure must be held constant over wide variations in flow, thanks to a piston.
4. **Electrical Heater**: this device allows for separate control of the temperature of the primary flow or the secondary flow, enabling the investigation of temperature effects on the performance of an ejector. The heater comprises two 75 kW elements, providing a maximum heating power of 150 kW. This heating power enables the attainment $200°C$ at the specified maximum mass flow rate. The heater has a maximum operating pressure of 8 bars, consistent with the pressure values within the facility.
5. **Mass flow meter**.
6. **Ejector**: the primary nozzle is floating in the T-connection and ejector (maintained on the left solid flange of the T-connection) and drives the primary stream into the ejector main body. The latter is divided in three parts: the secondary converging nozzle, the mixing duct and the diffuser. The ejector is air single-phase, compressible, circular cross section shaped, single nozzle and Constant-Pressure Mixing ejector configuration, in detail in Figure 2.1 and Figure 2.3.

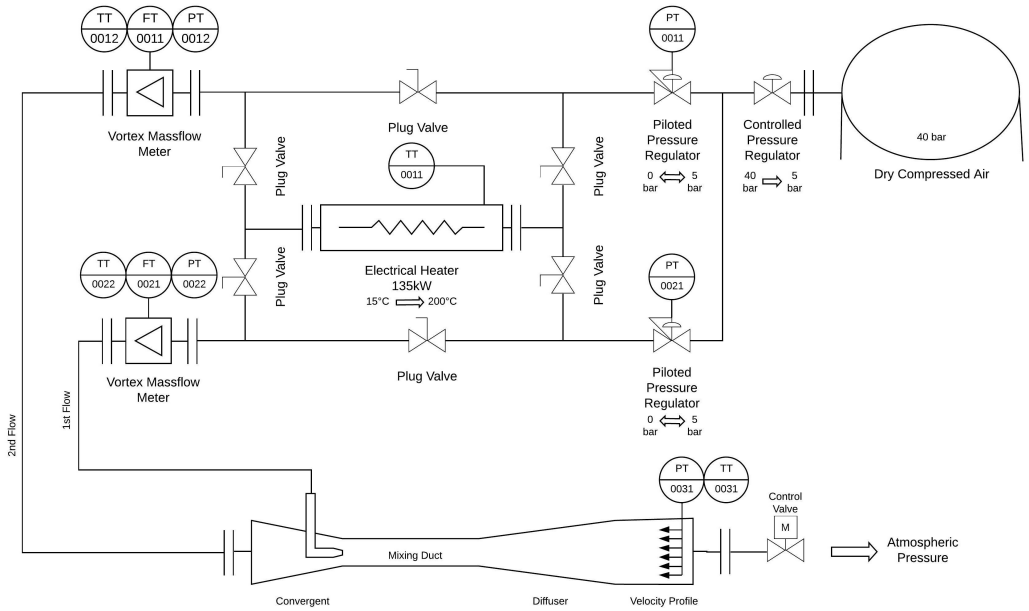

(a) Scheme.

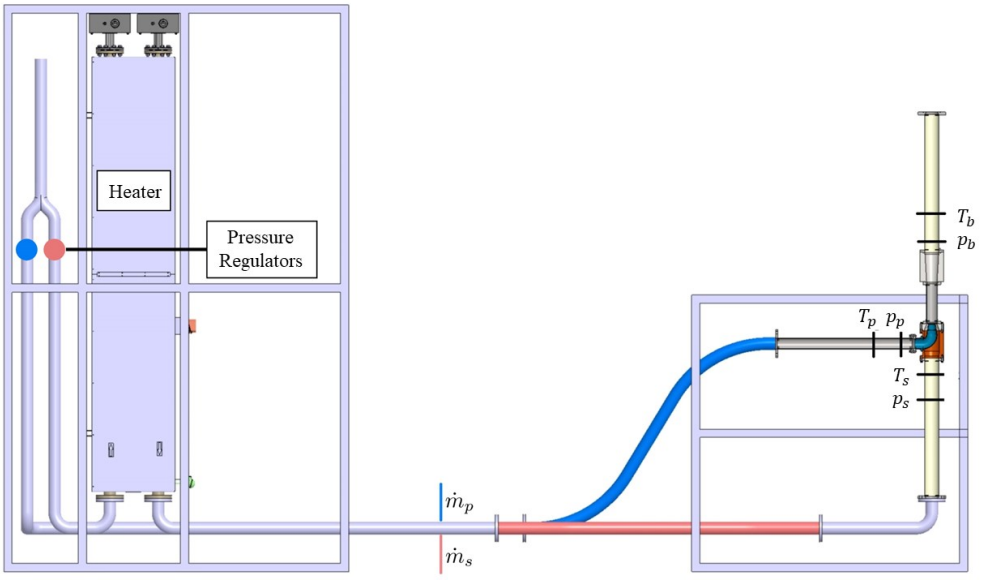

(b) Model.

Figure 2.2: Von Karman Institute bench test for supersonic ejector.

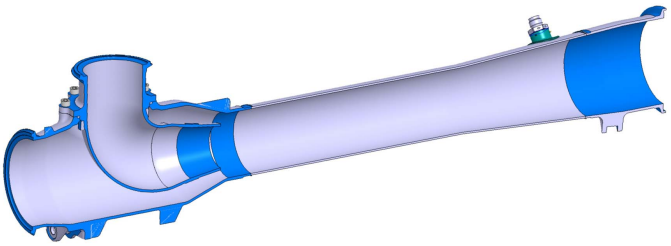

(a)

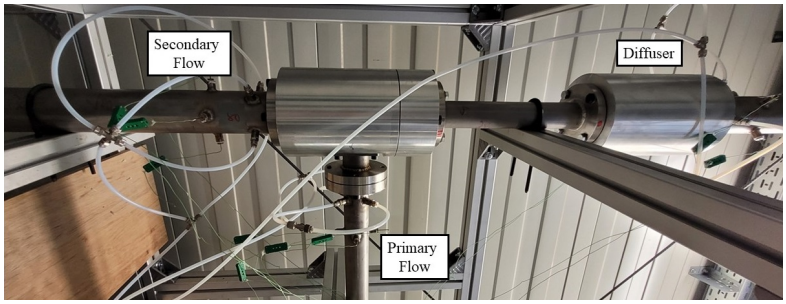

(b)

Figure 2.3: Supersonic ejector: Convergent primary nozzle.

7. **Thermocouples**.
8. **Pressure sensors**.
9. **Data Acquisition System (DAS) and notebook**.

Below, some of the components that make up the facility's equipment are further explored.

2.1.1 Multi-Parameter Mass Flow Meters

Mass flow meters are devices that accurately measures mass flow rate of a fluid traveling through a duct. They evaluate the amount of mass per unit time of the fluid passing through the pipeline.
Two Heinrichs Series DVH in-line Mass Flow Meters [14] are mounted for each line, Figure 2.4. Each of them uses a unique sensor head to monitor mass flow rate by directly measuring three variables–fluid velocity, temperature and pressure. Starting from these, the built-in flow computer calculates the mass flow rate. Vortex mass flow meters use three primary sensing elements: a vortex shedding velocity sensor, an RTD temperature sensor, and a solid state pressure sensor to measure the mass flow rate of gases, liquids, and steam.

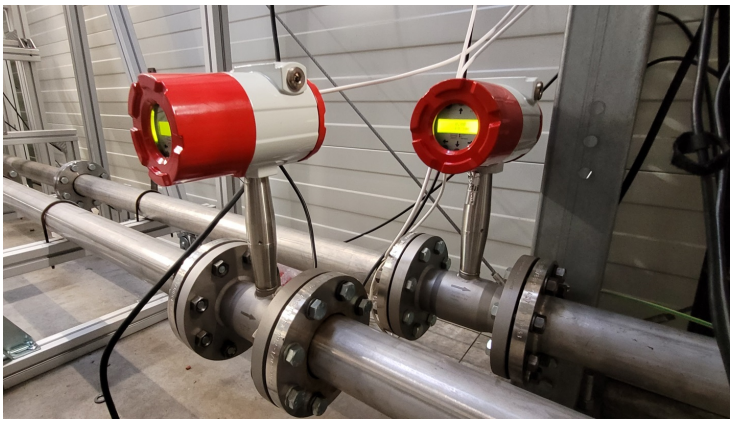

Figure 2.4: Heinrichs Series DVH in-line Mass Flow Meters.

Three distinct mass flow meters are available. These multivariable meters have been selected to encompass the necessary range of mass flows. It's noteworthy that these mass flow meters are engineered to operate efficiently with high-temperature gases, and they exhibit an accuracy level of 1.5% of the Full Scale for mass flow rate measurements.

2.1.1.1 Temperature

Temperature is measured with a Platinum Resistance Temperature Detector (PRTD). RTD sensors comprise a length of fine wire, typically composed of pure platinum, wound around a core with exceptional heat resistance. Temperature measurements are predicted on the fluctuations in electrical resistance within the sensing element. Specifically, as the temperature of the medium surrounding the sensor increases, so too does the resistance. Notably, the platinum wire exhibits a resistance of 1000 ohms at the temperature of $0°C$. In contrast to thermocouples, which exhibit nonlinear characteristics in relation to temperature, RTDs demonstrate an almost linear relationship between temperature and resistance across an extensive temperature range. One notable feature of metallic materials employed as resistive elements is their tendency to exhibit a linear relationship between resistance and temperature within the range of 0 to 100°C. This temperature-dependent resistance characteristic is often represented by the symbol α:

$$\alpha = \frac{R_{100} - R_0}{100°C \cdot R_0}$$

Where R_0 is the resistance of the sensor at $0°C$ and R_{100} at $100°C$.
Pure platinum has $\alpha = 0.003925\,\Omega/(\Omega \cdot {}^{\circ}\,C)$.

In industrial applications, specific standards are established by intentionally introducing impurities through a process known as doping, which results in varying α values for platinum.

2.1.1.2 Pressure

Pressure measurement is achieved using a solid-state pressure transducer. The pressure transducer operates by generating pulse train outputs to measure pressure through the creation of strains in a silicon diaphragm. This diaphragm incorporates piezoresistive sensing elements, which are essentially distributed resistance-capacitance (RC) networks diffused onto the diaphragm surface. These elements function as the control components of phase shift oscillators. This innovative approach allows for the transmission of a digital (frequency) signal from the source without being constrained by noise or distance limitations. Additionally, it eliminates the necessity for precise analog-to-digital conversion. Consequently, this device offers significant advantages in terms of reliability, accuracy, size, and cost when compared to conventional analog devices in use today.

2.1.1.3 Velocity

The velocity measurement principle relies on the widely recognized Von Karman vortex shedding phenomenon. In this process, vortices are generated from a shedding bar, and the vortex velocity sensor, positioned downstream from the shedding bar, detects the passage of these vortices. The frequency of vortex shedding is thus known, which characterizes the phenomenon of Von Karman vortices.
This velocity measurement technique offers several notable advantages, such as inherent linearity, a high turndown ratio, reliability, and simplicity. Von Karman vortices are created downstream of a shedder bar, forming two distinct wakes. Within one wake, the vortices exhibit a clockwise rotation, while in the other, they rotate counterclockwise. These vortices form one at a time, alternating their generation from the left side to the right side of the shedder bar. They exert influence on the surrounding space by dominating any nearby swirls that are on the verge of developing. In close proximity to the shedder bar, the distance, or wavelength, between vortices remains consistently uniform and quantifiable. Consequently, the volume enclosed by each vortex remains constant. The DVH/DVE Flow Meter calculates the total fluid volume by detecting the number of vortices passing the velocity sensor.
The linear range is defined by the Reynolds number. The Reynolds number

is the ratio of the inertial forces to the viscous forces in a flowing fluid and is defined as:

$$Re = \frac{\rho V D}{\mu}$$

Where ρ is the mass density of the fluid being measured, V is the velocity, D the internal diameter of the flow channel and μ is the viscotity of the involved fluid. The Strouhal number is the other dimensionless number that quantifies the vortex phenomenon:

$$St = \frac{f_s d_s}{V}$$

Where f_s is the frequency of vortex shedding, d_s shedder bar width and V is the fluid velocity.

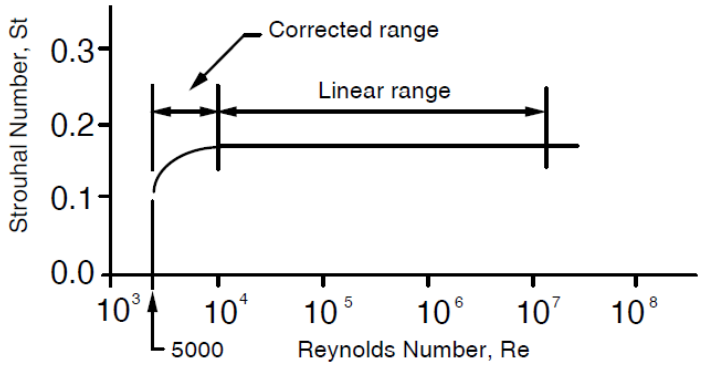

Figure 2.5: Reynolds Number Range.
[Reprinted from "Vortex Flow Meter: Instruction Manual", by Heinrichs KOBOLD Group [14]. © Copyright by HEINRICHS Messtechnik GmbH.]

As depicted in Figure 2.5, DVH/DVE meters demonstrate a consistent Strouhal number across a broad spectrum of Reynolds numbers. This consistency signifies a steady linear output that encompasses a wide array of flow rates and fluid compositions. Beneath this linear range, the advanced electronics embedded in DVH/DVE meters automatically rectify deviations in the Strouhal number concerning the Reynolds number. The meter's intelligent electronics achieve this correction by simultaneously monitoring the temperature and pressure of the process fluid. This real-time data is then employed to compute the Reynolds number. These meters autonomously correct down to a Reynolds number as low as 5000.

2.1.2 Thermocouples

A thermocouple is a temperature-measuring sensor comprised of two dissimilar metallic elements conjoined at a common terminal. When subjected to temperature fluctuations, the junction of these metals generates a voltage, as a result of the Seebeck effect, that may be effectively associated with the prevailing temperature. A thermocouple, on the other hand, is a device utilized to gauge the variation in electric potential between a hot and a cold junction involving dissimilar materials. This electric potential disparity is directly proportional to the temperature contrast between the hot and cold junctions.
The thermocouple, valued for its straightforwardness, durability, and cost-efficiency, finds extensive utilization across diverse temperature measurement applications.
They are available in different combinations of metals or calibrations. Among the most commonly used types, Type K thermocouples are favored due to their affordability and broad temperature range. In general, a Type K thermocouple encompasses temperature sensors featuring Chromel and Alumel conductors, designed to meet stringent output specifications mandated by prevailing regulations. The actually Type K thermocouples used, produced by the Von Karman Institute itself, are also employed within the facility.
In the facility, four thermocouples are used in three different stations, each placed in distinct radial positions to capture temperature profiles inside the different lines.

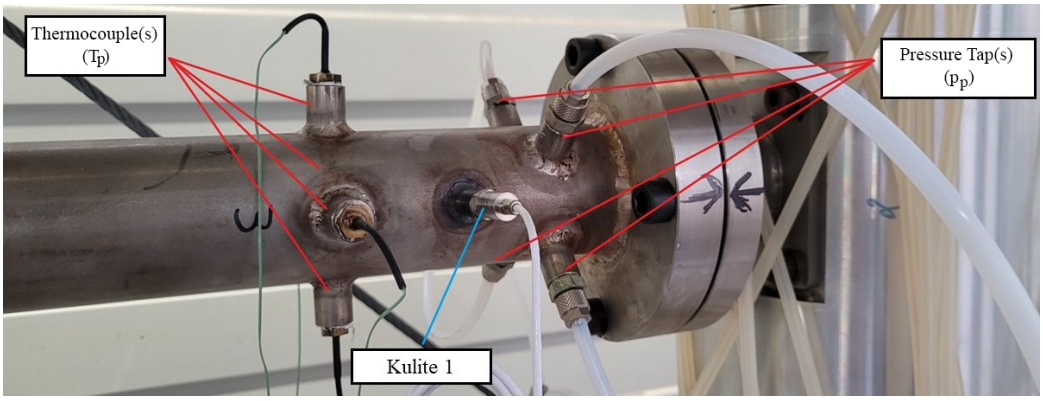

Figure 2.6: Primary Inlet Flow Sensors.

2.1.3 Pressure Sensors

Static pressure measurements are carried out using pressure tabs and DP15 Validyne Differential Pressure Transducer.
Pressure tabs consist of holes perpendicular to the wall exposed to the flow from which the measurement is taken. Through steel spout connectors, they are connected to flexible rubber tubes that transmit the pressure signal to the transducer. Consequently, when a wall is exposed to a flow, the pressure acts perpendicular to the wall itself.
The Validyne DP15 pressure sensors, shown Figure 2.7, function as electric pressure transducers, converting the input physical pressure jump signal, Δp, into an analog electrical signal, specifically a voltage jump, ΔE.
The pressure sensing component consists of a flat diaphragm made of mag-

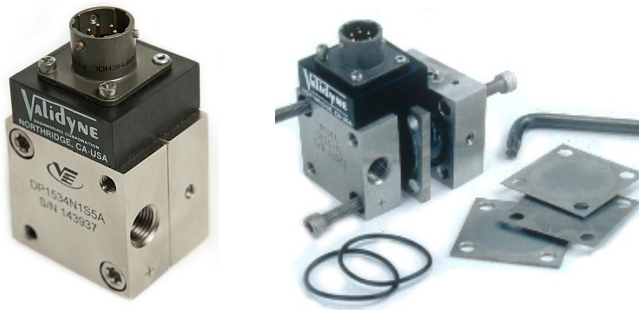

(a) Assembled. (b) Membrane details.

Figure 2.7: DP15 Validyne Differential Pressure Transducer.
[Reprinted from "DP15 Variable Reluctance Differential Pressure transducer: Instruction Manual" [15]. © Copyright by Validyne Engineering.

netic stainless steel, securely clamped between two case halves constructed from the same material in a symmetrical configuration. Embedded within the case halves are pick-off coils that detect the deflection of the diaphragm. These coils are shielded with a non-magnetic stainless steel layer, ensuring that the pressure cavity maintains an entirely stainless steel surface exposed to the working fluid. Vent valves are included to facilitate thorough liquid filling for dynamic measurements.
As shown in the Figure 2.2, there are 3 pressure transducers: one for the primary flow (Validyne 1), located before the primary nozzle inlet, one for the secondary flow (Validyne 2), just before the converging duct that forms the secondary pipes, and one for the backward outlet conditions (Validyne 3), after the divergent.
In-situ calibration of the pressure transducer is necessary. This calibration

process involves associating known input pressure jump measurements, facilitated by a comparison instrument, with unknown output values.

DP15 Validyne	
Full Scale	±7.05 Pa
Accuracy	±0.5% FS

Table 2.1: DP15 Validyne Specifications

2.1.3.1 Calibration

The comparison instrument used is the pneumatic version of the DPI 601 Digital Pressure Indicator, shown in Figure 2.8, which is a portable device serving as both a pressure indicator and handy calibrator.

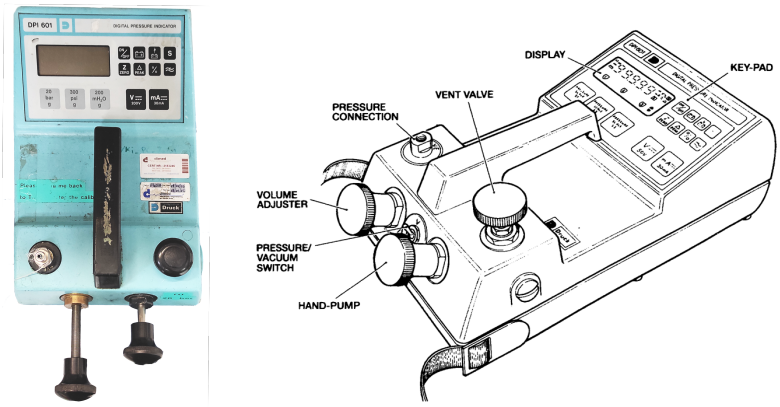

(a) Equipment. (b) Instrument Controls.

Figure 2.8: DPI 601 Digital Pressure Indicator.

This microprocessor-based instrument employs an internal transducer to measure and display pneumatic pressure applied to the connection port. Additionally, it generates voltages for externally connected transducers and transmitters while measuring their resulting output. Input and output sockets allow for the connection of external transmitters and transducers. The instrument can be equipped with a hand-pump, volume adjuster, vent valve, or any combination of these components to facilitate pressure generation. When the pneumatic system is connected and the instrument is set to pressure measurement mode, the vent valve should be closed, and the hand-pump can be used to generate the required pressure. The volume adjuster can be

manipulated to make fine adjustments to the pressure as needed.
In the calibration process of the transducer, the input quantity is known thanks to the use of the DPI 601 Digital Pressure Indicator, but not its relationship with the output voltage jump. The purpose of this phase is to determine, through sequential acquisition of sample values, the parameters involved in the mathematical relationship between the known pressure data and the voltage data acquired through measurements. The governing law is of a linear nature for the transducer mounted in the measurement chain:

$$\Delta p = k_T \cdot \Delta E$$

Where $\Delta E = E - E_0$, where E_0 is the so-called offset voltage value obtained under wind-off conditions, which corresponds to $\Delta P = 0$ bar. The calibration constant k_T is determined through a linear regression between pressure and tension, represented by the slope of the resulting line.
In the Table 2.2, data is collected for 11 different pressure values ranging from $[0; 5]$ bar, along with the corresponding electrical output signals lies in $[0; 10]$ Volt range, for the three pressure transducers present in the experimental setup.

Validyne 1		Validyne 2		Validyne 3	
$\Delta E[V]$	$\Delta p[bar]$	$\Delta E[V]$	$\Delta p[bar]$	$\Delta E[V]$	$\Delta p[bar]$
0.001	0.000	0.020	0.000	0.001	0.000
1.001	0.498	1.595	0.800	0.851	0.432
1.912	0.954	1.983	1.000	1.834	0.927
2.930	1.466	3.175	1.600	2.739	1.381
4.264	2.132	3.959	2.000	4.019	2.023
5.165	2.583	4.954	2.500	5.005	2.515
5.829	2.910	5.961	3.000	5.959	2.987
6.972	3.473	6.970	3.500	6.942	3.472
8.181	4.069	7.983	4.000	7.847	3.915
9.059	4.492	9.008	4.500	9.041	4.499
10.096	4.995	10.042	5.000	9.991	4.952

Table 2.2: Pressure-Voltage calibration data.

The calibration curve for Valydine 1 is shown in the Figure 2.9 and is constructed based on the values collected for the respective transducer through linear regression. The curves for the other two transducers are provided in the Appendix B. The first-degree polynomial fitting yields the calibration constants, which are the slopes of each line and their corresponding zero-input voltage offset values, i.e., the voltage values recorded with zero input

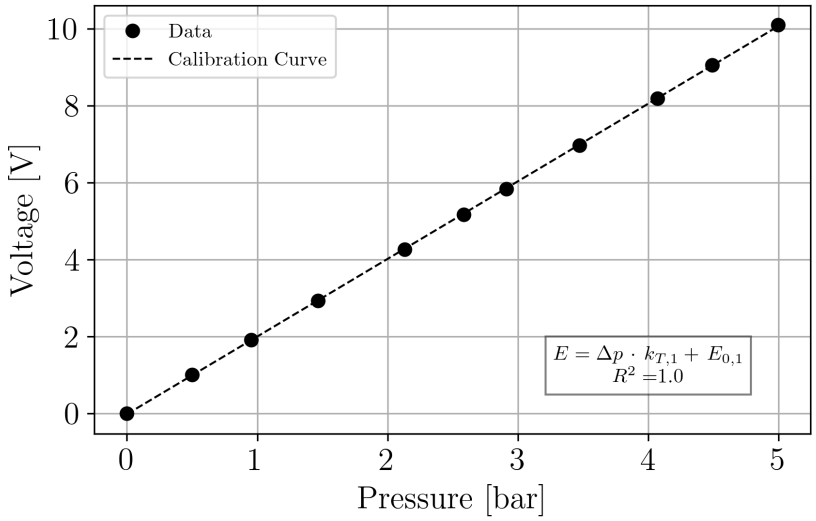

Figure 2.9: "Validyne 1" Curve Calibration.

pressure:

$$\begin{cases} \Delta p_1 = E_{0,1} + E \cdot k_{T,1} & k_{T,1} = 0.496\,bar/V \quad E_{0,1} = 10\,mmV \\ \Delta p_2 = E_{0,2} + E \cdot k_{T,2} & k_{T,2} = 0.499\,bar/V \quad E_{0,2} = 11\,mmV \\ \Delta p_3 = E_{0,3} + E \cdot k_{T,3} & k_{T,3} = 0.496\,bar/V \quad E_{0,3} = 17\,mmV \end{cases}$$

The usage curve of the Valydine 1 pressure transducer is shown in the Figure 2.10, along with its associated error range that might affect the measurement due to instrument uncertainty.

2.2 Experimental Campaign

The experimental procedure can be divided into several phases in order to obtain the fluid dynamic data of interest for various upstream operating conditions. These phases can be summarized as follows:

1. Generation and storage of compressed air.
   First and foremost, it is necessary to generate the compressed fluid that will be supplied to the facility for experimental testing. Dry air (single-phase) is used for both involved flows.
   - Activation of devices for generating dry compressed air at 7 bar (power generator, dryer, and finally the compressor).
   - Storage of compressed air maintained at 7 bar in an external tank outside the laboratory.

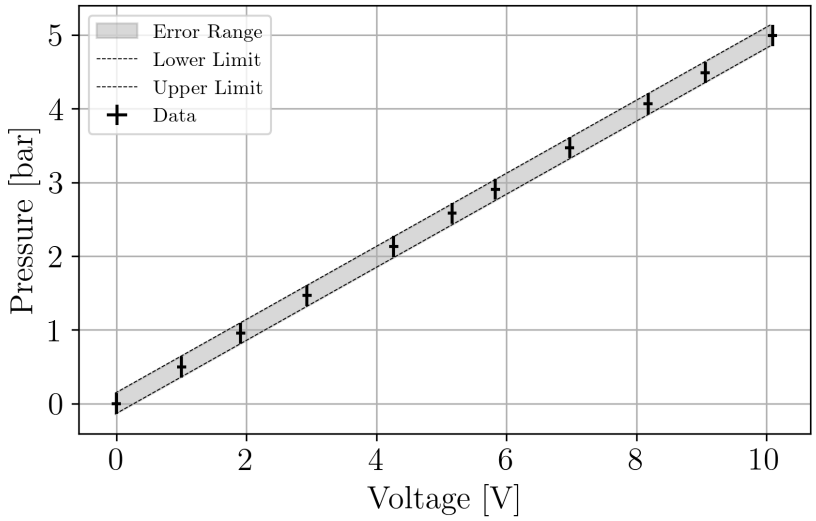

Figure 2.10: "Validyne 1" Usage Curve.

2. Routing of compressed air.
   Once the compressed air has been stored, it can be used to power the facility installed in the laboratory. This is done by manually opening and closing valves to direct the compressed air to the specific facility where experimental tests are to be conducted.

3. Setting operating conditions.
   After directing the compressed air to the facility, it is possible to set the input parameters of the facility: the values of static pressure for the primary, secondary, and outlet flows, and optionally, their respective static temperatures. In this context, the use of the electric heater is not necessary, as the temperature's effect on the operational curves of the ejector is negligible under the imposed operating conditions [16] beacuse the temperature acts on the density (and hence the mass flow rate), but the flow field is mainly dependent on the pressure. Therefore, precise temperature control is not required for the ejector's performance. The facility is controlled and data is acquired remotely through the graphical interface of the notebook using LabView software, which allows for the adjustment of the necessary parameters and variables.

2.2.1 Data Acquisition.

A LabView software is used for the specific facility to control, manage, and acquire input and output signals from the entire instrumentation installed

within the facility.

Quantity	Scale	Offset
$Q_{m,cold}$	62500	-250
$T_{m,cold}$	6250	-75
$P_{m,cold}$	375	-1.5
$Q_{m,hot}$	62500	-250
$T_{m,hot}$	21875	-87.5
$P_{m,hot}$	375	-1.5
P_1	0.4956	0.0102
P_2	0.4992	0.0108
P_3	0.4963	0.0172
p_{atm}	100508.673 [Pa]	

Table 2.3: "Test001" Calibration parameters.

1. Scaling Window: Data for calibration curves (sensitivity and offset) for pressures, temperatures, and flow rates of the two mass flow meters and the three Validyne pressure transducers.
   Calibration values are provided in the Table 2.3 for "Test001".

2. Global Window: This graphical interface is where input conditions for the facility and acquisition sampling data are set.
   The inputs include voltage values within the range of $[0 \pm 5]$ Volts for the pressure control valves: the hot and cold regulators, corresponding to the primary and secondary flows, which regulate static pressures at the inlet, and a percentage range of $[0 \pm 100]\%$ for the closure of the outlet pressure valve.

2.2.2 Post-Processing

The conducted experimental campaign facilitated the acquisition of raw data. Post-processing of experimental data involves a varied array of techniques, ranging from statistical analyses to normalization procedures, aimed at deriving meaningful insights and drawing scientifically sound conclusions. Below, the stages of post-processing carried out subsequent to the experimental campaign are outlined.

2.2.2.1 Uncertainty Analysis

By setting the voltages of the pressure regulating valves for the hot and cold lines and the closing percentage of the output valve, the hot and cold flow

mass rates adapt to the operating conditions and are measured and recorded at the frequency and sampling time set in the Global Window. The Table 2.4 shows the values of the sample acquisitions of the quantities of interest. These sampling values were chosen as a trade-off between measurement time and accuracy, taking into consideration the characteristic time of the sensors; for instance, a thermocouple is slow. The outgoing data is recorded in a

Device	**Time**	**Frequency**	**N. Samples**
Mass Flow Meter(s)	20 s	10 Hz	200
Pressure Sensor(s)	20 s	10 Hz	200
Thermocouple(s)	20 s	1 Hz	20

Table 2.4: Sampling Parameters.

TMDS file, which is a structured binary file format developed by National Instruments. In a structured format, it organizes measurements into channels. Each channel belongs to a channel group, and a file contains multiple channel groups. The generated TMDS file includes four channel groups: *Constants*, which contains all calibration parameters and ambient pressure values; *TC Data*, with thermocouple temperature values; *P-T Data*, housing all channels related to mass flow meters (mass flow, temperature, and pressure) and pressure transducers, both calibrated and raw data; and finally, *Kulite Data*, which provides specifications for the pressure sensor for dynamic testing but it is not utilized in this work, as the focus is primarily on steady-state conditions.
The acquired data consists of a time series of measurements. From these samples, the best estimate of the output quantity and the associated error are determined. Here, we present the evaluation of the best estimate and the respective uncertainty of the static pressure of the primary flow for "Test100". The sample size allows for a statistical treatment. The best estimate of the measured quantity is provided by the mean value of the N measurements taken:

$$\overline{p}_p = \frac{1}{N} \sum_{i=0}^{N} p_i(t)$$

To assess the uncertainty, we utilize the concept of the standard deviation of the measurements. In general, the standard deviation measures the amount of variation or dispersion in a set of data points. It quantifies how much individual data points deviate from the mean (average) of the data set. In mathematical terms, in this particular case, the standard deviation is the

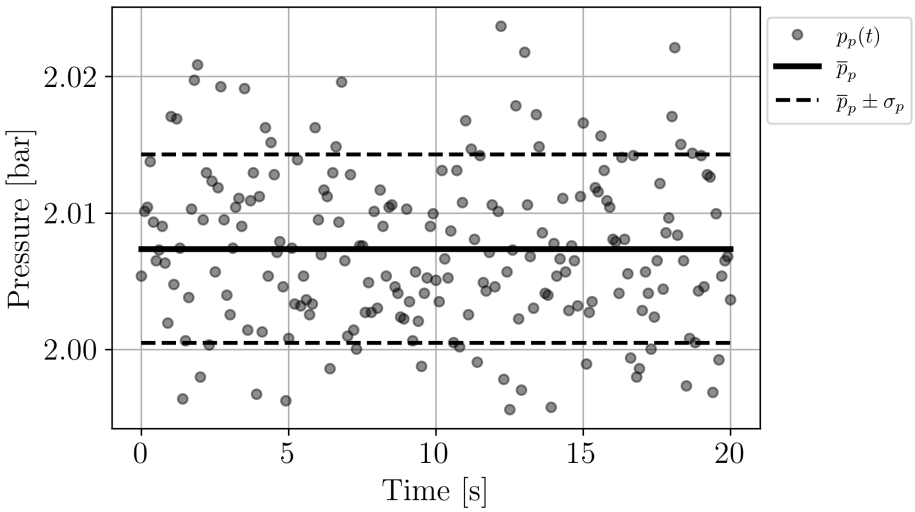

Figure 2.11: Primary static pressure time series for "Test100".

square root of the variance:

$$\sigma_p = \sqrt{\frac{1}{N}\sum_{i=0}^{N}\left(p_i(t) - \overline{p}_p\right)^2}$$

The Figure 2.11 displays measurements taken over the sampling time of static pressure in the primary flow for Test100, along with their corresponding best estimate subject to uncertainty.
The standard deviation, σ_p, is related to the probability density function (PDF) $P(x)$ of the values obtained from the N measurements. This represents the probability $p(x)$ that a given value x of the continuous variable falls within the interval $x/(x+\Delta x)$, divided by the width of the interval Δx, as this width approaches zero:

$$P(x) = \lim_{\Delta x \to 0} \frac{p(x+\Delta x) - p(x)}{\Delta x} = \frac{dp(x)}{dx}$$

In practice, one does not have access to an infinite set of real values, but rather a discrete set N of real numbers x_j. When dividing the interval $[x_{min}, x_{max}]$ into a certain number N_c of subintervals (bins or channels) with a width Δx, taking into consideration the definition of probability as the ratio of favorable cases to possible cases, we have:

$$P(x_i) = \frac{n_i \Delta x}{N}$$

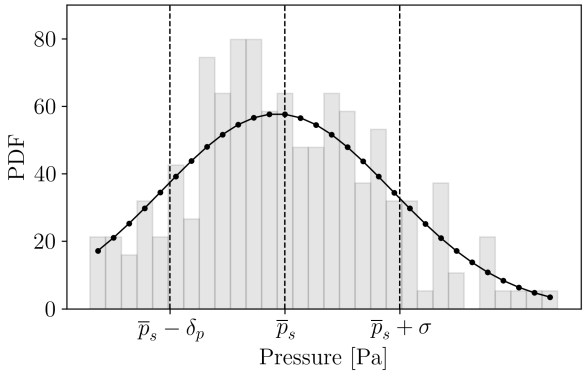

Figure 2.12: PDF Primary static pressure for "Test100".

Here, n_i represents the number of x values that fall within the i-th subinterval. The computation of the Probability Density Function (PDF) involves partitioning the interval $[x_{min}, x_{max}]$ into N_c subintervals and determining how many values of x_j fall within each of these subintervals (i.e., evaluating ni for each subinterval). Subsequently, each count is divided by $\Delta x\, N$.
The probability density function of the data comprising the time series in the Figure 2.11, is depicted in Figure 2.12.
The statistical analysis discussed here is not feasible for thermocouple data due to the limited number of samples, despite the presence of four sensors installed radially at each station. When dealing with scattered temperature measurements, the best estimate is taken as the mean value, with the associated uncertainty represented by the range within which all measurements fall, denoted as $(T_{max} - T_{min})$. Figure 2.13 shown the temporal measurements for the primary flow in Test100, its best estimate and the uncertainty, $\delta_T = (T_{max} - T_{min})/2$.

2.2.2.2 Error Propagation

Experimental measurements are subject to their respective random errors, which propagate into the assessment of ER and pressure ratios.
As previously introduced, the error of independent physical quantities with known uncertainties propagates to the final quantity through the mathematical relationship defining it. We explicitly refer to Equation 2.1:

$$p_0 = p\left[1 + \frac{\gamma - 1}{2}\left(\frac{\sqrt{R}}{S\sqrt{\gamma}}\,\frac{\dot{m}\sqrt{T}}{p}\right)^2\right]^{\frac{\gamma}{\gamma-1}} \tag{2.1}$$

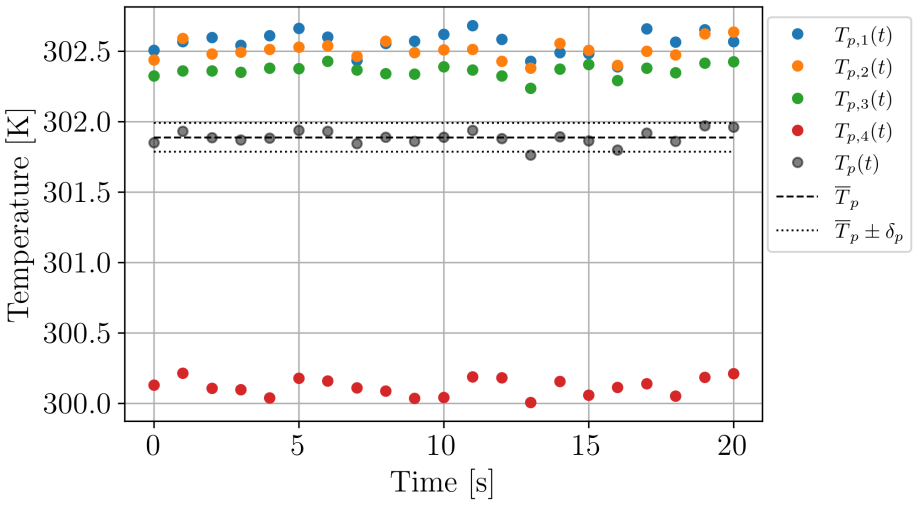

Figure 2.13: Primary static temperature time series for "Test100".

In this formula, the measurements of mass flow rate, static temperature, and static pressure all feature instrument errors that propagate along the measurement chain.
Following error theory, the uncertainty in total pressure is given by:

$$\delta p_0 = \sqrt{\left(\frac{\partial p_0}{\partial p} \cdot \delta p\right)^2 + \left(\frac{\partial p_0}{\partial T} \cdot \delta T\right)^2 + \left(\frac{\partial p_0}{\partial \dot{m}} \cdot \delta \dot{m}\right)^2}$$

Here, $\frac{\partial p_0}{\partial p}$, $\frac{\partial p_0}{\partial T}$, $\frac{\partial p_0}{\partial \dot{m}}$ represents the sensitivity of the total pressure with respect to changes in static pressure, static temperature, and mass flow rate measurements, respectively. This error, in turn, accumulates in the assessment of the total pressure ratio Π:

$$\delta \Pi = \sqrt{\left(\frac{\partial \Pi}{\partial p_{p,0}} \cdot \delta p_{p,0}\right)^2 + \left(\frac{\partial \Pi}{\partial p_{s,0}} \cdot \delta p_{s,0}\right)^2}$$

And for the second pressure ratio $p_b/p_{p,0}$:

$$\delta(p_b/p_{p,0}) = \sqrt{\left(\frac{\partial (p_b/p_{p,0})}{\partial p_{p,0}} \cdot \delta p_{p,0}\right)^2 + \left(\frac{\partial (p_b/p_{p,0})}{\partial p_b} \cdot \delta p_b\right)^2}$$

As for ER (Entrainment Ratio):

$$\delta \omega = \sqrt{\left(\frac{\partial \omega}{\partial \dot{m}_p} \cdot \delta \dot{m}_p\right)^2 + \left(\frac{\partial \omega}{\partial \dot{m}_s} \cdot \delta \dot{m}_s\right)^2}$$

2.2.2.3 Variables on Interest

The experimental process and data acquisition have enabled the creation of a database of experimental values for the main static parameters and mass flow rates. At this stage, it becomes of interest to construct dimensionless graphs related to the ejector's performance using the data acquired during the experimental tests. Particularly, our focus lies on the Ejector Ratio (ER), defined as the ratio of secondary to primary mass flow rates, as a function of certain pressure ratios while neglecting the influence of temperature ratios. This relationship can be expressed as:

$$\omega = \frac{\dot{m}_s}{\dot{m}_p} = f\left(\frac{p_b}{p_{p,0}}, \frac{p_{s,0}}{p_{p,0}}, \frac{T_{s,0}}{T_{p,0}}\right)$$

Processing the acquired data is necessary to derive the respective total parameters. To summarize:

1. Set the input operating conditions (hot and cold pressure regulator valve voltages and valve closure percentages).
2. Acquire static parameters (mass flow rates, pressures, and temperatures for the hot line, cold line, and outlet).
3. Process the data to evaluate the respective total parameters.

Total pressures can be determined using the following formula applicable to compressible fluids:

$$\frac{p_0}{p} = \left(1 + \frac{\gamma - 1}{2} M^2\right)^{\frac{\gamma}{\gamma - 1}} \tag{2.2}$$

Where $M = V/\sqrt{\gamma RT}$ is the Mach number of the flow at the station of interest for evaluating total pressure. Preliminary evaluation of density is required to determine the velocity for Mach number calculation, as per Formula 2.2. Density, as per the ideal gas law, is given by $\rho = p/(RT)$.
Finally, velocity is derived from the conservation of mass equation:

$$V = \frac{\dot{m}}{S\rho}$$

Here, S represents the flow passage area at the specific station in the facility's circuit.

2.2.2.4 Normalized Mass Flows

As previously introduced, the key data regarding the performance of the ejector pertains to the mass flow rates and their ratio. Therefore, it is advisable

to assess the normalized mass flow in order to determine if the primary nozzle is choked. This consideration is necessary because the thermodynamic model presented in the next Chapter 3 is valid only for double-choked or single-choked operating conditions, in which at least the primary nozzle is always choked.
The normalized mass flow of a calorically perfect gas through the choked primary is given by:

$$\hat{\dot{m}}_p = \frac{\dot{m}_p}{p_{p,0} A_{p,t} \sqrt{\frac{\gamma}{RT_{p,0}}} \left(\frac{\gamma+1}{2}\right)^{-\frac{\gamma+1}{2(\gamma-1)}}}$$

Where $A_{p,t}$ is the throat area for the primary nozzle. The denominator is the maximum value of the primary mass flow $\dot{m}^*$.
The total temperature is evaluated via the following isentropic relationship from the experimental data:

$$T_{p,0} = T_p \left(\frac{p_{p,0}}{p_p}\right)^{\frac{\gamma-1}{\gamma}}$$

The normalized secondary mass flow:

$$\hat{\dot{m}}_s = \frac{\dot{m}_s}{p_{s,0}(A_y - A_{p,t}) \sqrt{\frac{\gamma}{RT_{s,0}}} \left(\frac{\gamma+1}{2}\right)^{-\frac{\gamma+1}{2(\gamma-1)}}} \qquad T_{s,0} = T_s \left(\frac{p_{s,0}}{p_s}\right)^{\frac{\gamma-1}{\gamma}}$$

Where $A_y - A_{p,t}$ is the minimum cross section area for the secondary flow duct.

2.2.3 Results

The Figure 2.14 shown the dimensionless quantities obtained in the experimental campaign for the convergent configuration of the primary nozzle and the relative errors.

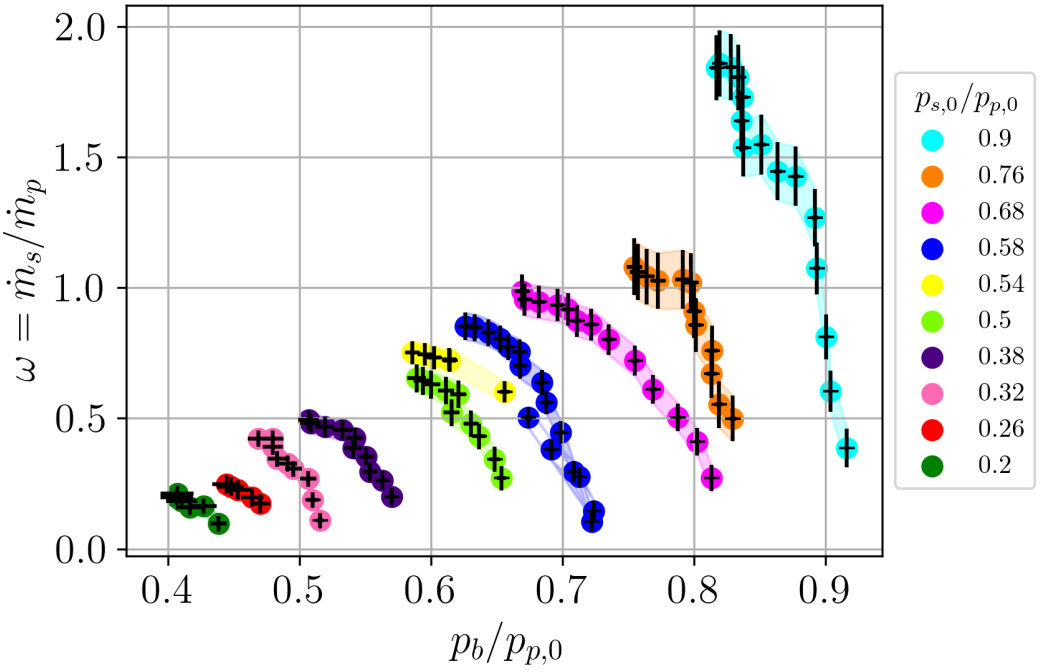

(a) $\omega = \omega(\Pi, \tau)$

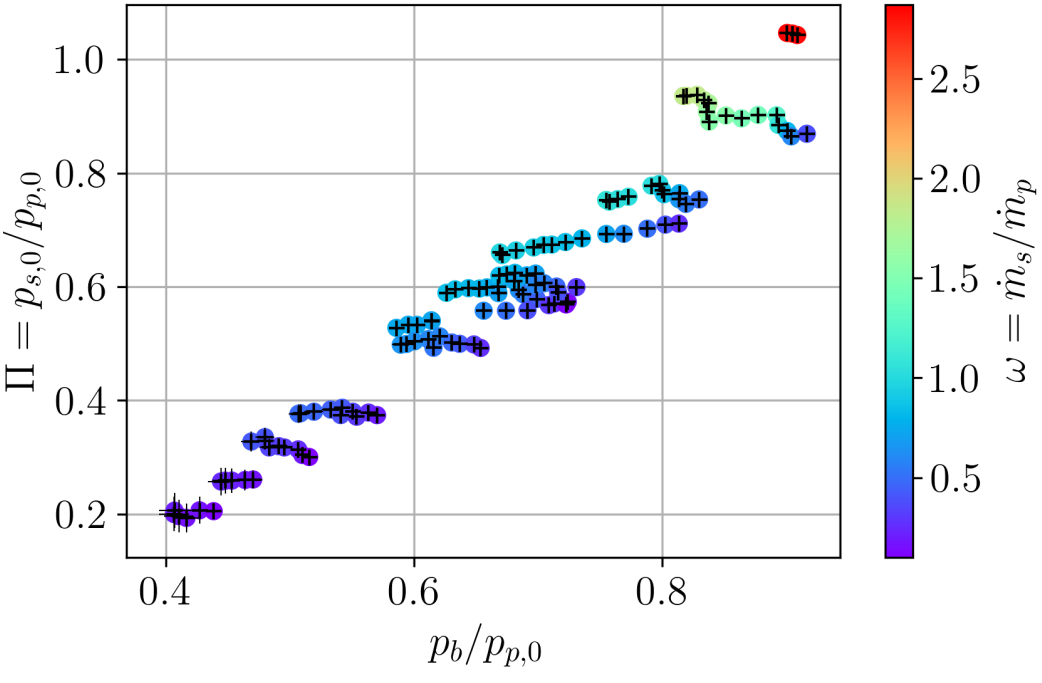

(b) $\Pi = \Pi(\tau, \omega)$

Figure 2.14: Results of the experimental campaign for convergent primary nozzle configuration

As mentioned in Section 2.2.2.4, it is imperative to analyze the normalized mass flow rates.
Set the pressure ratio $p_{s,0}/p_{p,0}$, the normalized mass flow is evaluated for each test while varying the backpressure through the opening and closing of the outlet pressure valve. The Figure 2.15 presents the $\hat{\dot{m}}$ values for the cases where $\Pi = 0.76$, in (a), and $\Pi = 0.20$, in (b).
For $p_{s,0}/p_{p,0} = 0.76$, the normalized mass flow values for the primary stream are below unity, indicating that the flow is not choked under these operating conditions, and the corresponding analytical curves are not suitable for such a scenario. Conversely, for example, for the ratio $p_{s,0}/p_{p,0} = 0.20$, the operating conditions with the primary nozzle choked is also provided, and the normalized mass flow values for the primary stream are equal to the unity.
Similarly, for the total pressure ratio $\Pi = 0.90$, the primary mass flow is not choked, and the normalized values are shown in the Figure B.2 in the Appendix B.

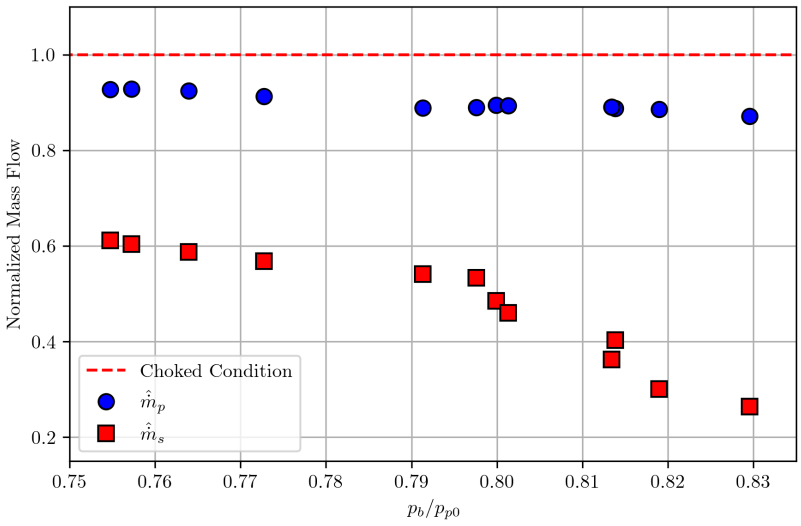

(a) $p_{s,0}/p_{p,0} = 0.76$

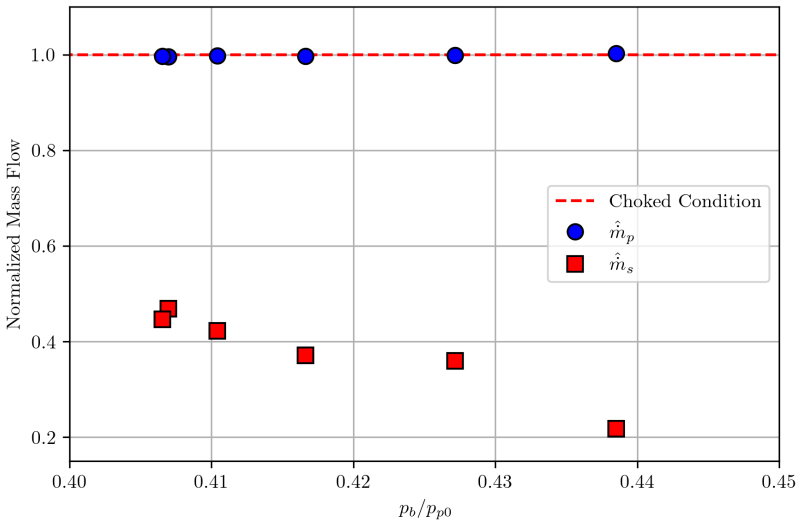

(b) $p_{s,0}/p_{p,0} = 0.20$

Figure 2.15: Normalized Mass Flows.

Chapter 3

Analytical Model

Ejector design may be performed at various levels of complexity.
Thermodynamic models are economical and efficient for simulating fluid dynamic phenomena which take place along the ejector and get operating curves to carry out a basic internal design study which would otherwise be computationally more expensive.
Here is considered a zero-dimensional, thermodynamic model that represents a suitable alternative for design and development applications. That allows a fast evaluation of the performance of an ejector starting from its basic geometry characteristic in terms of instantaneous thermodynamic parameters, such as pressure and temperature. However, they use simplifying hypotheses which lead, in some cases, to a lack of accuracy or a limited predictive capability.
In 0D models, the mass, momentum and energy conservation equations are used to evaluate ejector performances over large volumes to compute flow variables in key sections, such as the throat. All these equations are coupled and some assumptions are postulated in order to simplify the problem and this analytical model is only capable of evaluating global information, like mass flow rates.
With this type of model it is not possible to simulate complex fluid dynamics structures, like oblique shock waves or the turbulent mixing of the two flows, but it is possible to include mixing and friction losses to improve the performance of ideal models. Regardless, correctly calibrated and validated, the proposed 0D model is suitable for the accurate calculation of the pressure evolution with the purpose of predicting ejector performances and secondary mass flow entertainment for a fixed geometry.

3.1 Thermodynamic Model Review

The first thermodynamic model dates back to the early 1950s, developed by Keenan and Newman [17]. Their model was able to predict the performance of a constant area mixing ejector (without a diffuser), based on ideal gas dynamics and the principles of conservation of mass, momentum, and energy. The critical condition is incorporated into the model, but it does not account for pressure losses and assumes constant-area mixing, considering the gas as ideal. Keenan et al. [18] later refined this model, proposing the concept of constant pressure in wich the pressures of the primary and induced flows are identical at the exit of primary nozzle, and that the mixing of both streams starts at a uniform pressure up to the inlet of the constant area section without heat and friction losses. This model however only provided limited information about the choking phenomenon.
Since then, analytical models now take into account isentropic and mixing losses with efficiency coefficients. A few years later, based on shadowgrams of the flow within a rectangular ejector, Fabri and Siestrunck [11] formulated a new phenomenology concerng the choking of the secondary flow. According to the authors, when the stagnation pressure of the secondary fluid is sufficiently high, the maximum induced mass flow rate may be limited by the geometric throat located in the primary nozzle exit plane. In other words, in such cases, the secondary stream reaches sonic conditions at the location where it comes into contact with the primary stream. This choking phenomenolgy is referred as *Fabri-choking* criterion.
Though somewhat unrealistic, this criteria has been subsequently used by a vast majority of thermodynamic. Based on those early works, a number of first generation thermodynamic models were proposed; Eames et al.[8] introduced in 1995 a model that included irreversibilities due to friction losses by using isentropic efficiencies; Huang et al. [19] developed a model of double-choking that also took irreversibilities into account, but for which they considered that the mixing phenomenon occurred inside the constant area duct. In this case, the induced secondary stream accelerates as it flows along the primary jet and reaches unity Mach number at the section of maximum expansion of the primary flow, i.e. in a sort of aerodynamic throat located some distance downstream of the exit of the primary nozzle. Both streams remain separated by a perfect slip surface until a certain section where the secondary flow is choked, at a so-called *hypothetical throat* located in the constant area part of the ejector. The mixing process then takes place downstream.
All of the above theoretical models were helpful in obtaining the ejector performance when the ejector was in critical operation, and the results agreed

well with the experimental data. But predicting performance when the ejector is at sub-critical operation is also important for fields in industry, and the models mentioned above do not include such information.
In the early 2010s, Chen et al. [20] proposed a model to predict the entrainment ratio at sub-critical operation, but the information given on the model is not sufficient to evaluate its formulation or effectiveness. Their model was also based on the presence of an hypothetical throat inside the constant area duct. For the sub-critical operating regime, this hypothesis was conserved. The off-design performance was obtained by using a mixing efficiency dependant on the back-pressure of the ejector
Hence, the Fabri-choking is not necessarily representative of the actual phenomena occurring inside of a doubly choked ejector. In their article, Lamberts et al. [21] described a new choking theory for perfect gas based on the early work of Bernstein et al. [22] about the so-called compound-choking theory, which is further explored in Section 3.3.2.2. The model of Chen et al. [23] is modified to integrate the *compound-choking* theory in the Metsue [4] 0D model.

3.2 Assumptions and Algorithm

In this work is used the thermodynamic model presented by Metsue et al. [4].
The process is based on an iterative procedure where a series of compressible flow equations is solved step-by-step for selected zones. The calculated variables are assumed to be uniformly distributed in the radial direction.

The following assumptions are fundamental to the thermodynamic model in order to simplify the modeling of the fluid dynamic phenomena that occur in the ejector. The assumptions underlying the model uses are:

- The flow is one-dimensional, steady, and adiabatic. The inlet velocities of the primary and secondary flows, as well as the outlet velocity, are assumed to be negligible.
- The gas is treated as an ideal gas.
- Friction losses along the walls and within the shear layer between the primary and secondary streams are considered, are accounted for through isentropic efficiencies.
- As the primary nozzle exhausts, the primary and secondary flows do not mix before a specific section known as the *mixing section*, situated inside the constant area duct. This region starts at the so called *hy-*

pothetical throat, which will be detailed later, and it is stipulated that the pressures of both flows are equal at this point.

A schematic representation of the ejector, along with the notations that will be employed in subsequent discussions, is depicted in Figure 3.1.

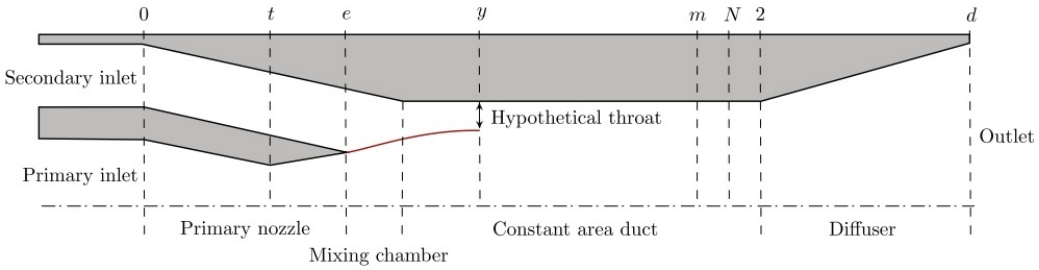

Figure 3.1: Schematic diagram of the model (top half).
[Reprinted from *"An improved thermodynamic model for supersonic real-gas ejectors using the compound-choking theory"*, by Metsue A., Debroeyer R., Poncet S., Bartosiewicz Y. [4]. © Copyright 2023 by Elsevier B.V.]

As the primary flow is assumed to be choked, the primary mass flow rate ($\dot{m}_p$) remains constant, unaffected by any downstream variables; it depends on solely upon primary stagnation conditions. The primary flow expands in the primary nozzle, and then continues to expand further within the mixing chamber until it reaches section y. Simultaneously, the secondary flow also expands upon reaching section y, at which point the mixing process commences. In essence, the two flows remain independent of one another until they both reach section y. It is noteworthy that the location of the mixing section y is assumed to be situated within the constant area section, whether the ejector operates under on-design or off-design conditions.
Subsequently, the two flows commence their mixing. If the flow is supersonic at section m, it subsequently experiences a normal shock at section N, which is positioned within the constant area section as well. As a result, the flow reaches the diffuser inlet – section 2 – at a subsonic velocity. Further compression takes place in the diffuser, where flow velocity is further reduced, and pressure is subsequently recovered.

3.3 On-Design Thermodynamic Model

The thermodynamic model is developed in two phases. Firstly, the on-design performance is evaluated based on the assigned stagnation conditions of the primary and secondary flows. Subsequently, the off-design segment of the

model is developed, which also relies on the predefined downstream pressure. The prediction of the entrainment ratio under on-design conditions involves the primary nozzle, which is always choked, and the mixing chamber where the two flows meet at the exit of the primary nozzle. Additionally, the secondary flow becomes choked at the hypothetical throat.

3.3.1 Primary Nozzle

Upstream of the primary nozzle and the mixing pipes of the secondary flow, the velocities of the two streams is assumed to be zero. The thermodynamic states upstream are considered known, corresponding to the stagnation conditions of the two fluids in this initial section, which would be the conditions along both conduits if there were no isoentropic losses until the exit section of the primary nozzle.
In particular, the flow in the primary nozzle can be solved from the stagnation conditions and the isentropic efficiency governing the flow in this part, by maximizing the mass flow rate instead of imposing a Mach number M equal to unity at the throat, which constitute the primary definition of a choked flow.
The relationships governing an isoentropic expansion of the fluid, corrected by the isoentropic efficiency factor of the primary nozzle η_p, which accounts for fluid dynamic losses along this duct, are employed to determine the thermodynamic conditions resulting from a non-isoentropic expansion process:

$$h_p = h_{p,0} - \eta_p(h_{p,0} - h_{p,is})$$

By using the ideal gas law:

$$p = \rho RT$$

And the conservation equations for mass flow and total enthalpy along the primary nozzle:

$$h_0 = h + \frac{V^2}{2} = const.$$
$$\dot{m} = GA = \rho VA = const.$$

The static conditions in the primary throat are iteratively determined to maximize the primary flow rate:

$$\dot{m}_p = G_{p,max} A_{p,t}$$

The primary nozzle is thereby defined as choked. Subsequently, starting from the conditions at the throat, the exit conditions of the primary nozzle are evaluated through a non-isentropic expansion process in the converging-diverging case.
The most challenging issue is to model the mixing phenomena.

3.3.2 Mixing Chamber

Due to their simplicity, analytical models are widely used for predicting the operation of an ejector. However, as of today, there is no universally accepted methodology due to the complexity of the choking phenomenon in the mixing chamber.
As previously mentioned, the absence of a globally accepted thermodynamic model can be attributed to the complexity of the flow phenomena at play in supersonic ejectors. One of the challenges lies in predicting the occurrence of choked flow conditions within the ejector. The interaction process between motive and suction streams in the mixing chamber is rather involved and plays a major role in ejector performance . It gives rise to a momentum exchange through turbulence, formation of a shock train and boundary layer interactions along the mixing chamber length. The shear mixing layer grows along gradually, to eventually form with the wall a minimum cross-section for secondary flow passage. This minimum cross-section is referred to differently by researchers, usually as a *thermodynamic throat* or critical section but all corresponding to the concept of effective area. However, the area of said hypothetical throat is unknown, and the primary and secondary flows in the mixing chamber thus have to be solved simultaneously.
The choking phenomenon will be interpreted according to two different approaches in this study: either the Fabri-choking or the compound-choking criterion.

3.3.2.1 Fabri-Choking

At the core of the Fabri-choking criterion approach, it is assumed that the secondary flow is choked at the hypothetical or aerodynamic throat, as shown in Figure 3.2. Both independent flows up to this section are considered, the area of which is unknown, necessitating the simultaneous resolution of both flows.
Initially, employing the same method as described for the primary flow and starting from the fixed stagnation conditions upstream, $G_{s,max}$ for the secondary flow is iteratively evaluated concerning the static conditions of the flow at section y. Subsequently, the expansion evolution conditions of the primary flow from the respective nozzle exit are evaluated such that the secondary flow is choked.
A flowchart of the model for on-design operation using the Fabri-choking criterion is shown in Figure A.1 in the Appendix A.
Nevertheless, Fabri-choking has been witnessed experimentally only once in

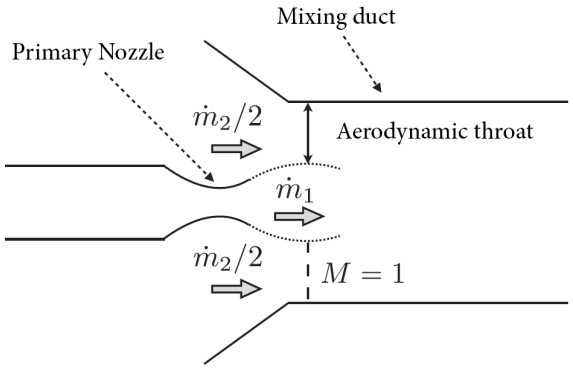

Figure 3.2: Schematic diagram for the model of Fabri-choking.
[Reprinted from "Numerical and experimental evidence of the Fabri-choking in a supersonic ejector", by Lamberts O., Chatelain P., Bartosiewicz Y. [21]. © Copyright 2018 by International Journal of Heat and Fluid Flow]

the research conducted by Lamberts et al. [21]. In fact, as stated by the authors, in numerous studies exploring on-design ejectors, there is no clear indication of a sonic section in the core of the secondary stream. Therefore, Fabri-choking might not accurately represent the real phenomena taking place within a doubly choked ejector.

3.3.2.2 Compound-Choking

Within their publication, Lamberts et al. [24] elucidate a novel choking theory that builds upon the initial concepts of compound-compressible nozzle flow theory proposed by Bernstein and others [22] in their work. The concept is illustrated in Figure 3.3 for an arbitrary number of streams n. As opposed to the Fabri-choking theory which considers each stream individually, the compound-choking theory — as its name suggest— uses a criterion based on the compound flow formed by n streams. Instead of assuming a sonic section in the secondary stream, the theory assumes the blockage of axially propagating acoustic waves when the compound-flow is said to be choked. According to the theory presented by Bernstein et al. [22], choking of the flow doesn't demand all sub-streams to reach sonic conditions at the throat. Instead, choking occurs under specific conditions where some of the streams achieve supersonic velocities at the throat while others maintain subsonic speeds. From an ejector's point of view, the theory suggests that the ejector reaches a choked state when one of its streams attains a specific supersonic speed while the other stream achieves a particular subsonic speed,

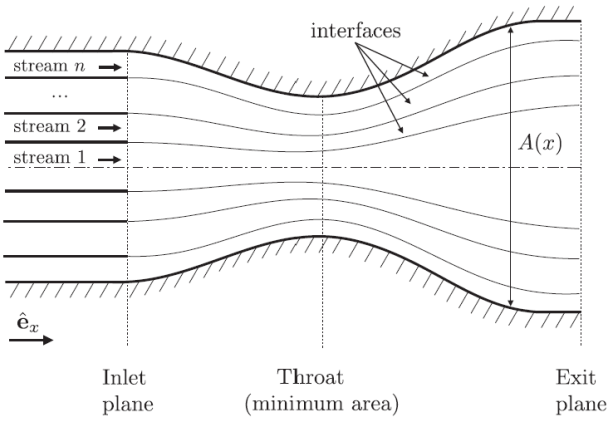

Figure 3.3: Illustration of the streams considered in the compound-choking theory. [Reprinted from *"The compoundchoking theory as an explanation of the entrainment limitation in supersonic ejectors."*, by O.Lamberts, P.Chatelain, N.Bourgeois, and Y.Bartosiewicz. © Copyright 2023 by Elsevier B.V.]

that ensures the following relations:

$$\beta = p_y \left[\frac{A_{p,y}}{\rho_{p,y} V_{p,y}^2} \left(1 - M_{p,y}^2\right) + \frac{A_{s,y}}{\rho_{s,y} V_{s,y}^2} \left(1 - M_{s,y}^2\right) \right] = 0$$

Where β is the compound-flow indicator in the ejector case. For $\beta = 0$ the flow is compound-sonic.
In supersonic ejectors, the primary flow becomes supersonic, and the secondary flow becomes subsonic in the choked section. This is due to the primary flow already achieving supersonic speeds following its expansion in the primary nozzle, thereby necessitating the model to have the secondary stream as subsonic. The secondary flow becomes supersonic downstream of the choked section as it expands further.
The solution is unique and the primary flow is supersonic and the secondary one is subsonic. The flowchart shown in the Figure A.2 in the Appendix A is solved iteratively with respect to the value of the static pressure at the hypothetical throat p_y.

3.4 Off-Design Thermodynamic Model

In accordance with the design results obtained in Section 3.5, the 0D thermodynamic model is developed using the criterion of maximizing the secondary mass flow rate.
Outside the operational conditions of the critical regime scenario, the ejector's operation depends on downstream conditions, particularly the back

pressure p_{out}.
Under off-design conditions, information travels upstream from the diffuser to the mixing section. This impacts the mixing conditions of the two flows, affecting the secondary mass flow rate and pressure p_y, while the primary flow remains choked. The pressure p_y increases while the secondary mass flow rate decreases. The entrainment ratio is dependent on the back pressure, which under on-design conditions corresponds to the critical pressure, below which the operation is considered off-design:

$$p_{out} < p^*_{out}$$

With initial conditions set upstream and evaluating thermodynamic states and velocities using the Fabri choking criterion, the thermodynamic state at station m, located within the duct of constant cross-section, is assessed. The two flows at station m are fully mixed and are no longer distinguishable separately. At the mixing section, assuming:

$$p_m = p_y$$

Here, the thermodynamic quantities of interest and the velocity of the completely mixed flow are assessed using the laws of conservation of total enthalpy and momentum.
The flow can exist as a single-state and may be either subsonic or supersonic. A check is necessary, and in the case where $M_m > 1$, normal shock wave relations are utilized to resolve the flow at station 2 before proceeding along the diffuser. Due to the flow being choked, the pressure calculated at the end of the diffuser is the critical pressure, noted as p^*_{out}.
Given a downstream pressure as the initial condition p_b, it's possible to determine whether the ejector is functioning under on or off-design conditions. For the latter scenario, the pressure at the end of the diffuser must align with the back pressure. This necessitates an iterative approach to solve the flow until finding the pressure p_y that satisfies the equation:

$$\varepsilon = \frac{p_{out} - p_b}{p_b}$$

where ε denotes the error tolerance.
The Flowchart illustrating the entire off-design model is depicted in the Figure A.3 in Appendix A and the Python code for the model implementation is reported in Listing A.1.

3.5 Results

In this section, a review of the accuracy of the models under on-design conditions for both choking criteria is now provided.
The Figure 3.4 shown the operational curves constructed using the two choking criteria. The reference geometry used is that of the ejector from the experimental bench at the von Karman Institute, under the same operating conditions in which the experimental tests were conducted, and with the following trial values for the loss coefficients, used in the Metsue's 0D model:

$$\eta_p = 0.977 \quad \eta_s = 0.71 \quad \eta_{py} = 1 \quad \eta_m = 0.995 \quad \eta_d = 1$$

The predictions of the model for the entrainment ratio will be compared to the experimental results. The relative error is defined as:

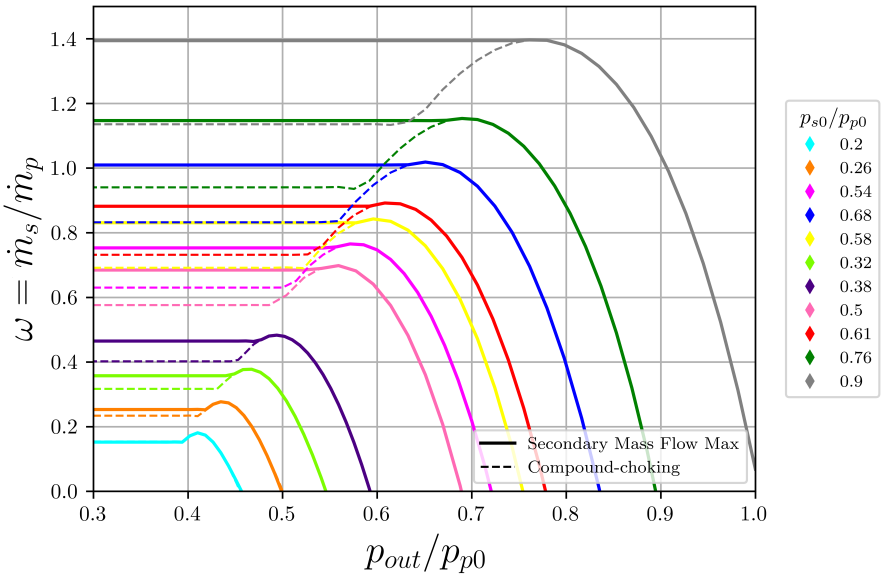

Figure 3.4: 0D Model Operating Curves.

$$\varepsilon_{model} = \frac{\omega_{model} - \omega_{exp}}{\omega_{model}} \cdot 100\%$$

with ω_{model} and ω_{exp} the entrainment ratios obtained from the experiment and the model, respectively.
Results provided by the models, using the Fabri-choking and Compound-choking criteria, are compared to the experimental data in Table 3.1.
The Compound-choking model provides poor results, with the maximum relative error about -27.59% for Test 001 and an average error of 16.70% in

Test	$p_{p,0}\,[Pa]$	$p_{s,0}$ [Pa]	ω_{exp}	ω_{F-C}	ε_{F-C} [%]	ω_{C-C}	ε_{C-C}[%]
001	515443.9	106262.9	0.213	0.152	-28.501	0.154	-27.594
007	397165.5	102264.8	0.247	0.253	2.588	0.234	-5.161
012	394583.8	208244.3	0.751	0.753	0.265	0.630	-16.091
036	310640.2	205123.2	0.987	1.010	2.295	0.832	-15.669
049	352079	207513.6	0.852	0.831	-2.508	0.692	-18.853
069	483689.4	158522.5	0.422	0.358	-15.193	0.317	-24.820
078	408455.7	153820.7	0.493	0.465	-5.637	0.402	-18.362
088	307740.2	153296.1	0.653	0.685	4.858	0.576	-11.751
098	253509.3	157028.3	0.831	0.882	6.061	0.732	-11.993

Table 3.1: Predictions of the entrainment ratio for the current ejector using the Fabri-choking and Compound-choking criterions.

module. It also appears very clearly that the model tends to underestimate the entrainment ratio, in fact all relative error values are negative, below the experimental data.
Instead, for the Fabri-choking criterion, one may observe a better prediction of the results, with a maximum relative error value of 28.50% for the Test 001 and an average mean value of 7.55%.
Figure 3.5 shows the entrainment ratio predicted by the model versus the experimental results. Although the maximum error is slightly higher for the Fabri-choking criterion, on average the model predicts the experimental data much better than Compound-choking.
For the Fabri-choking case, the model appears to become less accurate as the entrainment ratio gets lower, although it does not diverge with higher ω values. The opposite appears for the Compound-choking model based.

3.5.1 Effect of the Velocity at the Outlet

In Section 3.5, the assumptions underlying the analytical model utilized in this study are outlined. One of these assumptions is that the exit velocity from the ejector is zero. This simplifying assumption does not accurately represent the real phenomenon. In fact, in the results depicted in the figure, the operational curves are obtained by assuming a zero velocity at section *d*, causing the static and total pressure to coincide, except for losses along the diffuser. For a gas that is nearly perfect, quasi-one-dimensional, quasi-steady, isoenergetic, and isoentropic, the following relationship holds for the

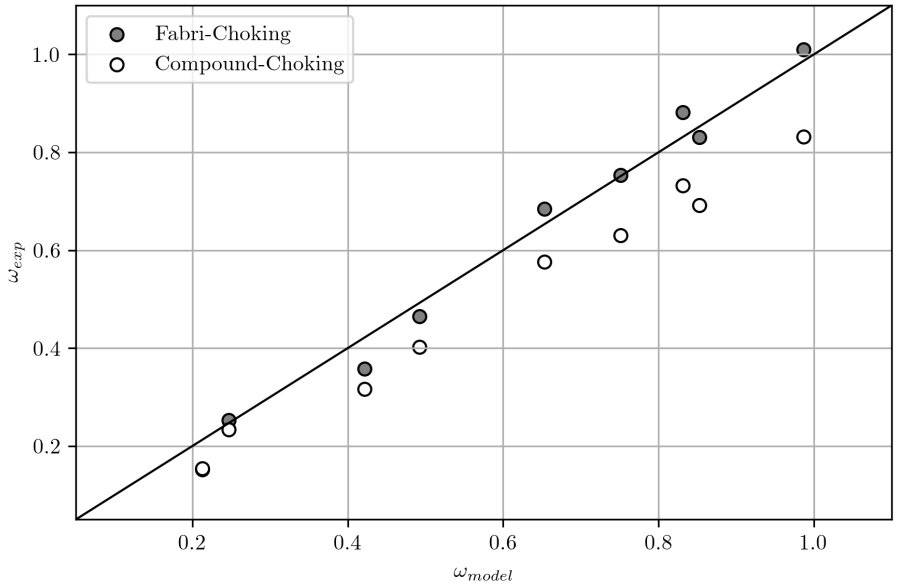

Figure 3.5: Comparison of the Fabri-choking and Compound-choking with the experiment.

area ratio as a function of the Mach number for a generic nozzle:

$$\frac{A}{A^*} = \frac{1}{M}\left[\frac{2}{\gamma+1}\left(1+\frac{\gamma-1}{2}M^2\right)\right]^{\frac{\gamma+1}{2(\gamma-1)}} \tag{3.1}$$

Where A^* is the hypothetical section where the flow reaches sonic conditions isentropically from the inlet conditions of the duct.
Thanks the Equation 3.1, it's possible to assess the diffuser's exit velocity, eliminating the assumption imposed earlier. The geometry of the diffuser is known (inlet and outlet areas). Additionally, the inlet conditions of the diffuser are known, particularly the Mach number M_2, allowing the derivation of the hypothetical section A^* from the Equation 3.1. At this stage, the critical ratio of sections A_d/A^* is known, allowing the derivation of the outlet Mach number M_d. The implicit relationship is iteratively solved:

$$\frac{A_d}{A^*} = f(\gamma, M_d)$$

A non-zero velocity at section d results in a different outlet pressure value compared to the initial assumption of zero velocity.The different pressure values evaluated for cases of zero (Case 1) and non-zero outlet (Case 2) velocities are compared for the ejector illustrated in Section 3.5.

For the operating condition dictated by the pressure ratio $p_{p,0}/p_{s,0}$, the corresponding results are presented in Table 3.2.

	$\boldsymbol{M_d}\,[-]$	$\boldsymbol{p_{out}}\,[\boldsymbol{Pa}]$
Case 1	0	164189.25
Case 2	0.11	162784.60

Table 3.2: Comparison of the diffuser exit conditions.

The corresponding relative error is:

$$\Delta p_{out} = \frac{p_{out,1} - p_{out,2}}{p_{out,1}} = 0.86\%$$

The operating curves for different operational conditions are shown in the Figure 3.6.

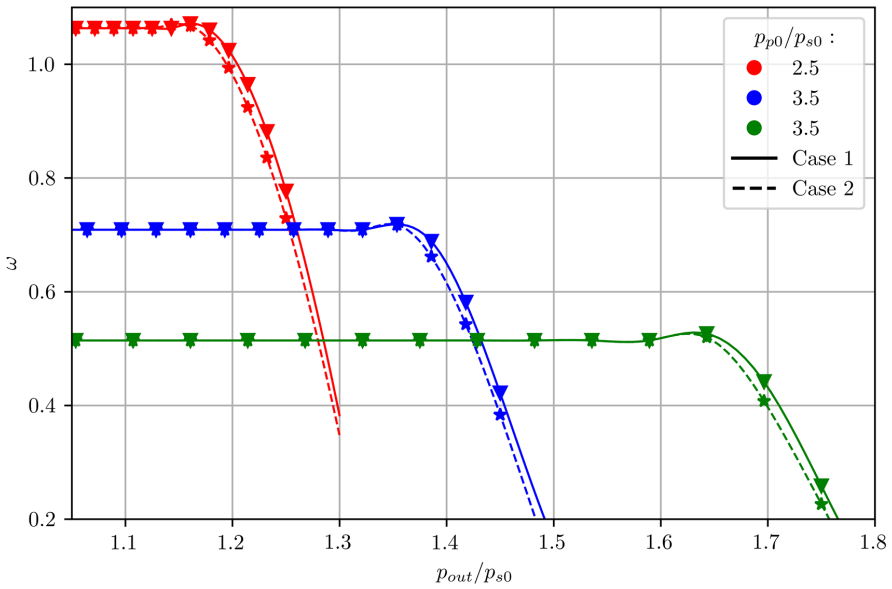

Figure 3.6: Comparison between the operating curves (secondary flow maximization criterion) constructed for zero outlet velocity ["Case 1"] and non-zero outlet velocity ["Case 2"].

The results do not differ significantly. However, following this analysis, the model with a non-zero outlet velocity is used because it is closer to the real phenomenon. Additionally, the algorithm, depicted in the flowchart in Figure A.4 in Appendix A, offers advantages in terms of computational efficiency, involving a smaller number of implicit equations to be solved compared to "Case 1".

3.6 Comparison between experimental data and analytical model

The experimental results obtained must undergo validation through comparison with data of a different nature. To facilitate the comparison between experimental and analytical results, it is imperative to calibrate the 0D model. In the realm of thermodynamic models, it is noted that predictive coefficients differ from one ejector to another due to variations in geometries leading to diverse losses. The internal fluid dynamics of the device varies depending on the internal geometrical characteristics of the ejector.

3.6.1 Thermodynamic Model Calibration

In the next Chapter, it is described the thermodynamic model used in this work. It needs to b calibrated with respect to five efficiencies, such as η_p, η_s, η_{py}, η_m and η_d.
The objective of this section is to determine the combination of these five parameters that best fits the experimental results with the model. This is accomplished through manual exploration by simultaneously varying these five parameters.
In this simplified approach, the focus is placed on the entire operating curve, assuming that the efficiencies are independent of back pressure. Thus, it can be observed that at least one set of efficiencies can adequately fit the entire operating curves. As a result, the five intervals for the variables to be entered into the optimizer are:

$$\eta_p \in [0.7, 1.0] \quad \eta_s, \eta_{py}, \eta_d \in [0.0, 1.0] \quad \eta_m \in [0.9, 1.0]$$

Figure 3.7 illustrates the operating curves of the ejector while keeping four efficiencies constant and individually varying one at a time. It becomes evident that only certain parameters have an impact on the on-design portion of the curves. The influence of the loss factor η_d is not reported, as, given the nature of the thermodynamic model, it does not affect the ejector's performance.
Delbecque's dissertation [25] on the calibration of thermodynamic models suggests a two-part optimization approach to avoid excessively long computation times. The first part of the calibration process involves aligning the on-design segments of the analytical curves with the experimental data by adjusting three loss factors: η_p, η_s, and η_{py}. The remaining two efficiencies do not influence the constant portion of the curves and are, therefore, not included in the initial phase of this fitting process.

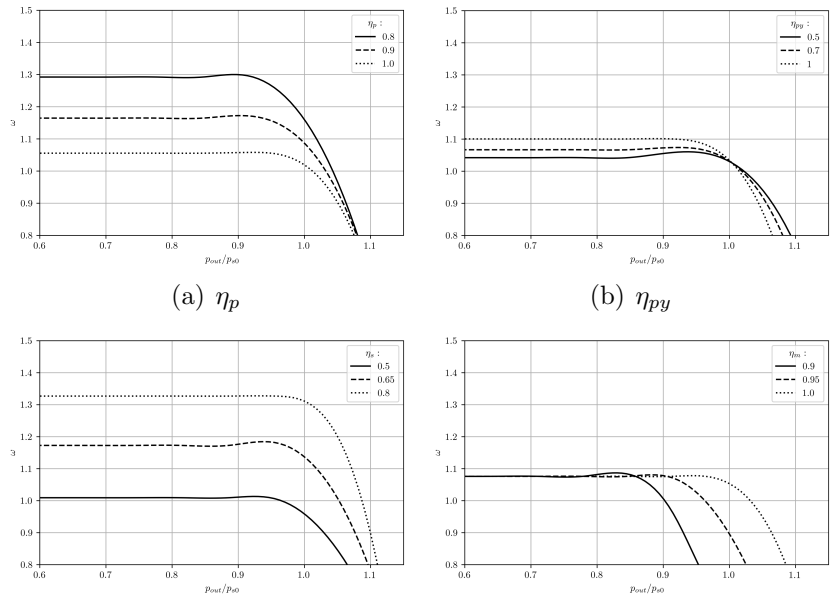

(a) η_p (b) η_{py}

(c) η_s (d) η_m

Figure 3.7: Influence of losses factors on the characteristic curve.

Subsequently, once the on-design curve segments have been properly calibrated, the efficiencies η_d and η_m are employed to adjust the entire curve, encompassing the remaining off-design data points. This approach allows the two final efficiencies to conform to the remaining data points without affecting the initial calibration.
The efficiencies combination found that best fits the operating curves to the corresponding experimental data is:

$$\eta_p = 0.98 \quad \eta_s = 0.56 \quad \eta_{py} = 0.78 \quad \eta_m = 0.99 \quad \eta_d = 0.7$$

3.6.1.1 Global Fitting

The Figure 3.8 shown the comparison between the experimental data and the appropriately calibrated 0D model is presented. It can be observed that the calibration process has led to an acceptable fit for all the curves using a single set of loss coefficients.

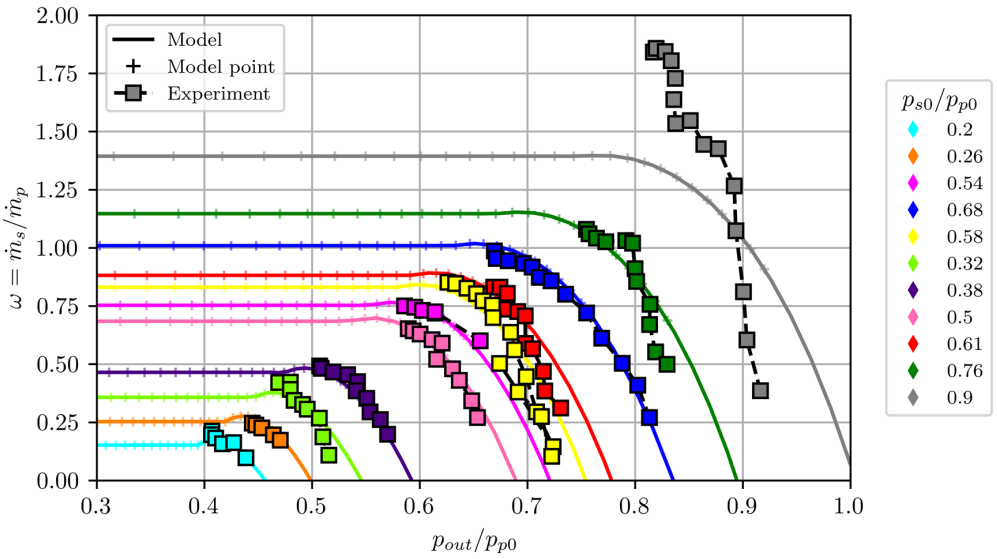

Figure 3.8: Comparison entrainment ratios between experimental and theoretical data.

The analytical curve and the corresponding experimental data for the total pressure ratio $p_{s,0}/p_{p,0} = 0.68$ overlap almost perfectly, while this alignment is less precise for the equivalent case at $p_{s,0}/p_{p,0} = 0.20$.
The overall calibration of the model is satisfactory, but from the previous observations, it is clear that it is possible to calibrate the coefficients for specific sets of experimental data since they depend on the particular operating conditions imposed.
However, the curves for the pressure ratio $p_{s,0}/p_{p,0}$ values of 0.90 and 0.76 deviate from the mathematical model.

3.7 Conclusion

This chapter has described two on-design models: the Fabri choking criterion and the Compound choking criterion.
From comparing the relative errors of the two models against the experimental on-design data, the current calibration of the model provides more accurate results with the Fabri-choking criterion. It is evident that the Compound choking criterion is the less accurate one and provides considerably inferior results compared to the Fabri choking criterion. The Fabri choking criterion yields significantly better results, and this model has been chosen for predicting the on-design conditions of the ejector. The thermodynamic model for off-design conditions was subsequently developed, enabling the determination of all ejector performances even for assigned back pressures lower than the critical pressure related to the on-design scenario.
It is important to note that the 0D model is based on crucial assumptions and relies on a simplistic approach. Furthermore, due to a lack of understanding of the complex flow phenomena within the ejector, errors in predicting entrainment by 0D models could be significant [19].

In the Chapter 2, we intruct the normalized mass flow rates definition. From that, it is advisable to exclude the curves and tests related to the cases $p_{s,0}/p_{p,0} = 0.90$ and $p_{s,0}/p_{p,0} = 0.76$, as they are not single-choked. The final graph, showing the comparison between experimental data and analytical curves under valid operating conditions following the global calibration of the thermodynamic model, is depicted in the Figure 3.9.

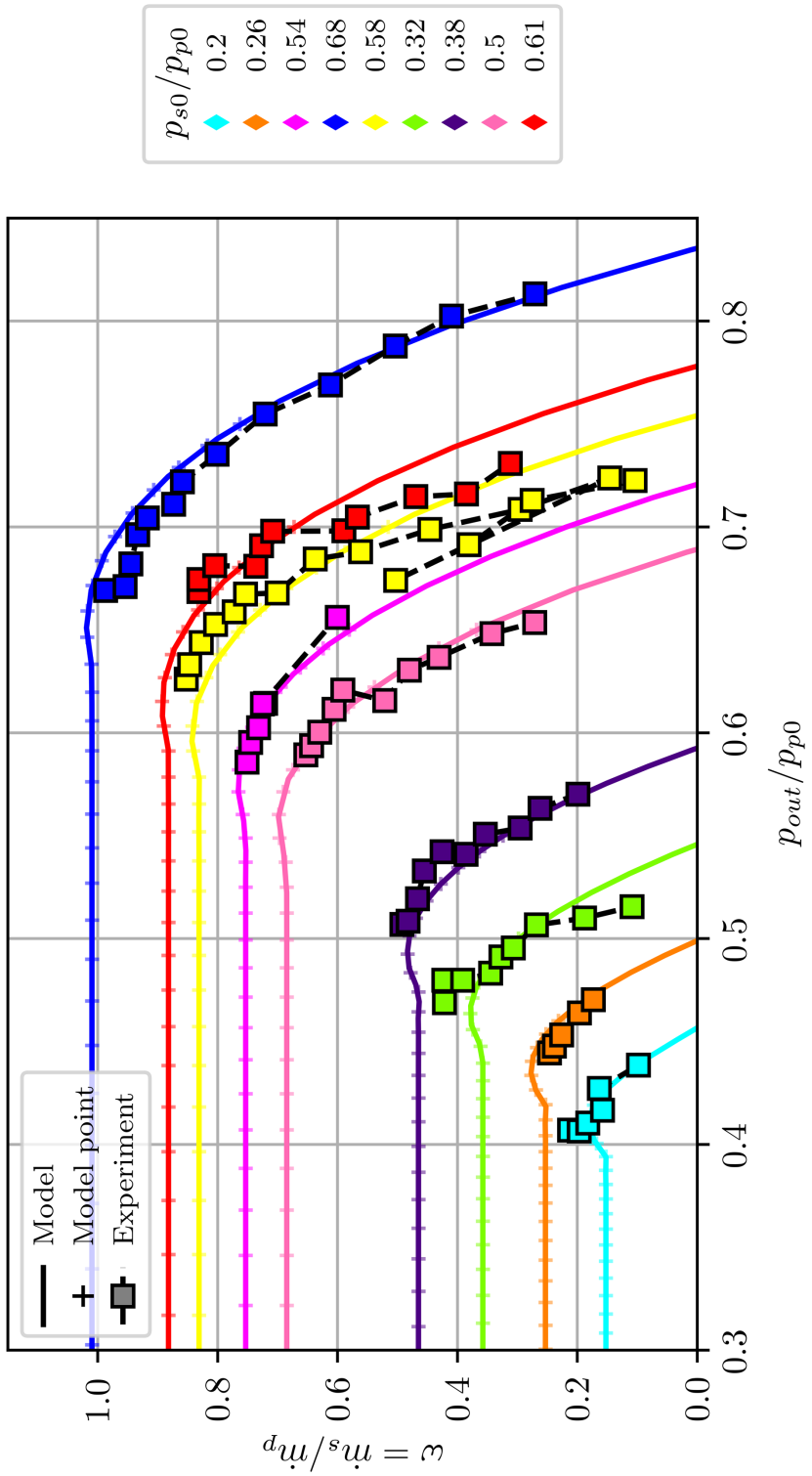

Figure 3.9: Comparison entrainment ratios Data for only choked operational conditions.

Chapter 4

CFD Analysis

4.1 Introduction

Despite the usefulness and the remarkable progress of thermodynamic models, they provide only a general understanding of ejectors. The analytical studies are unable to correctly reproduce the flow physics locally along the ejector. It is the understanding of local interactions between shock waves and boundary layers, their influence on mixing and recompression rate, that will allow a more reliable and accurate design, in terms of geometry and operation conditions.
A way of achieving this goal at a reasonable cost is through Computational Fluid Dynamics (CFD). In fact, numerical tools are a profitable way to generate results instead of a massive database of experimental campaigns that are complex and expensive in terms of time and materials.
The effectiveness of CFD lies in its ability to numerically solve the fundamental equations governing fluid flow, such as the Navier-Stokes equations. By discretizing the governing equations and employing sophisticated numerical algorithms, CFD allows to gain insights into the intricate details of fluid behavior, even in situations where analytical solutions are impractical or impossible to obtain.

The numerical simulations in this work are performed with OpenFOAM [26], which is an open-source software for CFD [27].
The open-source software library provided by OpenFOAM uses the finite volume method to solve the equations of fluid dynamics. In fact, the Finite Volume (FV) method is generally preferred for industrial CFD because it is relatively inexpensive and lends itself well to the solution of large sets of equations associated with complex flows, as well as to parallel solution by domain decomposition [28].

The numerical results have been obtained with an unsteady density-based compressible flow solver relying on central-upwind schemes of Kurganov et al. [29], named `rhoCentralFoam`, to solve systems of partial differential equations ascribed on any 3-dimensional unstructured mesh of polygonal cells. It is a central-upwind scheme that competes with the best methods previously published, and it is inherently simple and well-suited for a colocated, polyhedral finite volume framework [28].

4.1.1 Physics of the Problem

We wish to solve the standard governing fluid equations in an Eulerian frame of reference.

- Conservation of mass:

$$\frac{\partial \rho}{\partial t} + \boldsymbol{\nabla} \cdot (\rho \boldsymbol{U}) = 0 \tag{4.1}$$

- Conservation of momentum (neglecting body forces):

$$\frac{\partial (\boldsymbol{U}\rho)}{\partial t} + \boldsymbol{\nabla} \cdot (\rho \boldsymbol{U}\boldsymbol{U}) + \boldsymbol{\nabla} p + \boldsymbol{\nabla} \cdot \underline{\boldsymbol{\tau}} = 0 \tag{4.2}$$

  Where ρ is the mass density, $\boldsymbol{U}$ the fluid velocity, p the pressure and $\underline{\boldsymbol{\tau}}$ is the viscous stress tensor. Following the assumption proposed by Boussinesq [30], for viscous flows the stress tensor can be represented by:

$$\underline{\boldsymbol{\tau}} = 2\mu \, dev(\underline{\boldsymbol{D}}) \tag{4.3}$$

  It is the Newton's law assuming zero bulk viscosity, defined as positive in compression. The dynamic viscosity is represented by μ, the deformation gradient tensor $\underline{\boldsymbol{D}} = \frac{1}{2}[\boldsymbol{\nabla U} + (\boldsymbol{\nabla U})^T]$ and $dev(\underline{\boldsymbol{D}}) = \underline{\boldsymbol{D}} - \frac{1}{3} tr(\underline{\boldsymbol{D}})$ is its deviator component.

- Conservation of energy:

$$\frac{\partial (\rho E)}{\partial t} + \boldsymbol{\nabla} \cdot [\boldsymbol{U}(\rho E)] + \boldsymbol{\nabla} \cdot \boldsymbol{q} + \boldsymbol{\nabla} \cdot [(p\boldsymbol{I} - \underline{\boldsymbol{\tau}})\boldsymbol{U}] = 0 \tag{4.4}$$

  Where $E = e + \frac{1}{2}|\boldsymbol{U}|$ is the total energy density with e the specific internal energy, $\boldsymbol{q}$ is the diffusive flux of heat and $\boldsymbol{I}$ is the unit tensor. The diffusive flux of heat can be represented by Fourier's law:

$$\boldsymbol{q} = -k \boldsymbol{\nabla T} \tag{4.5}$$

  T is the temperature and k is the conductivity.

The Navier-Stokes equations are produced by substitution of the viscous and heat conduction constitutive relations, Equation 4.3 and Equation 4.5, respectively, into the governing equations.
Mean quantities conservation equations to be used in compressible flow RANS simulations, are written in terms of Favre's mass weighted averages [31]. Any dependent variable $f(t)$ can be split into mean and fluctuating components by writing $f(t) = f'(t) + \overline{f}$. Mean quantities conservation equations to be used in compressible flow RANS simulations, are written in terms of Favre's mass weighted averages.

4.1.2 Computational Method

We employ the Finite Volume approach on meshes composed of polyhedral cells characterized by an arbitrary number of faces, each featuring an arbitrary number of vertices. This results in the spatial domain being partitioned into numerous connected control volumes or cells. Typically, the mesh does not align with the coordinate system, and the count of neighboring cells may differ from one cell to another. A general observation is that a cell face is either internal, intersecting only two cells, or it forms part of an external boundary and is associated with a single cell.
The FV method is employed by formulating the differential equations to be solved as integrals over a fixed cell volume. The spatially-fixed cell volume is assumed in this context. To handle divergence and gradient terms, a generalized form of Gauss's theorem is applied, converting these terms into integrals over the cell surface. The integration process involves fluxes at cell faces, which are determined by interpolating values from the cell centers to the faces. In dealing with polyhedra possessing an arbitrary number of faces, it is preferable that the interpolation to a specific face involves only owner and neighbor cells to avoid excessive complexity. The second-order semi-discrete, non-staggered schemes proposed by Kurganov and Tadmor [32] facilitate this restriction, called `rhoCentralFoam`.
The `rhoCentralFoam` solver is designed for solving compressible, transient, and turbulent flows. It uses a central-upwind scheme for spatial discretization and supports both transient and time-dependent simulations. The solver is capable of handling flows where density variations are significant, which is common in compressible flows, and allow the shock capturing in the CFD simulations.

Regarding the time derivatives, they are discretised by a simple Euler first-order explicit scheme rather than more elaborate methods, such as higher-order Runge-Kutta time integration.

4.2 Pre-processing

4.2.1 Mesh Generation

The first step is to define the geometric domain of the simulation, which represents the physical domain where fluid flow will be analyzed.
The mesh for this case was generated using a custom Python script, that interacts with GMSH [33], a three-dimensional finite element mesh generator. All solvers developed within OpenFOAM are, by default, 3D, but can be used for 1- or 2-dimensional problems by the application of particular conditions on boundaries lying in the plane of the direction(s) of no interest.
In this study, a 2D axisymmetric computational domain is employed, revolving the 2D geometry in the $z = 0$ plane of $\pm 2.5°$ with respect to the x-axis. The first step is the declaration of geometry coordinates. It is very important to keep consistency in the numbering of the points. Starting from the definition of points in space, we proceed to declare oriented lines and splines, through which closed surfaces are defined. Subsequently, physical entities are assigned to different parts of the geometry, specifying which regions represent different materials or boundary conditions. In Figure 4.1, the details of the construction of the geometry for the secondary pipe and the primary nozzle are shown for both the convergent and convergent-divergent configurations.

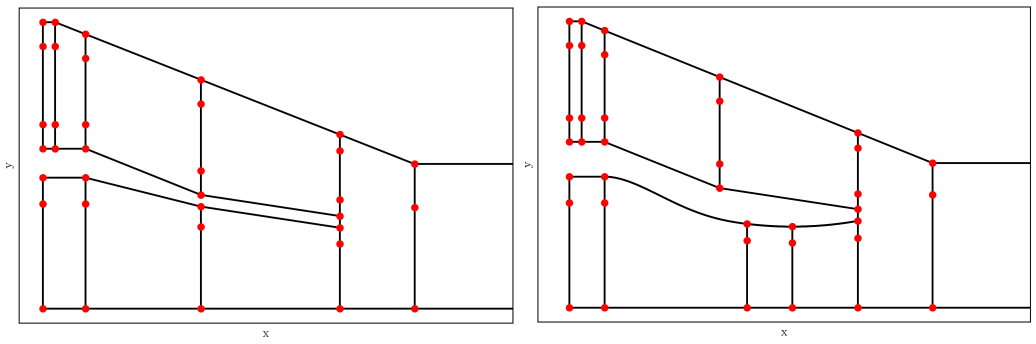

(a) (b)

Figure 4.1: Geometry Domain Detail: (a) Convergent Primary Nozzle Configuration; (b) Convergent-Divergent Primary Nozzle Configuration.

The convergent primary nozzle has a throat section exit of 14 mm, while the convergent-divergent one features a throat of 14 mm and an exit of 15 mm, wider by 1 mm compared to the simply convergent configuration, at the expense of the exit section of the secondary pipe.
The generated mesh is a structured mesh comprised of boxes. The script

that generates this mesh is feasible enough to generate any axisymmetric duct whose radii can be written as a well behaved function. The degree of resolution in the interior of the tube and along the tube axis is also highly customizable.
The Python script defines 6 physical regions that will later be used to set boundary conditions. These consist of the outer wall, the two faces of the wedge, the primary and secondary inlet and the outlet.
The file that the Python script produces was then loaded into Gmsh and the mesh was then constructed using the standard 3D meshing algorithm. The mesh file produced by GMSH was then transferred to the polymesh directory in the constant directory and converted to a format that OpenFOAM can read using the `gmshToFoam` command.
A structured mesh is adopted and refined at walls to ensure correct modeling of near-wall flow such that the boundary layer is sufficiently resolved, which occurs when y^+ of the first cell is approximately 1, where it is a non-dimensional wall distance for a wall-boundend flow, used in boundary layer theory and in defining the law of the wall, Figure 4.2.. In that case, the cells enter the viscous sublayer, allowing to accurately compute the friction at the wall. Near the walls, elements are refined in the direction normal to the

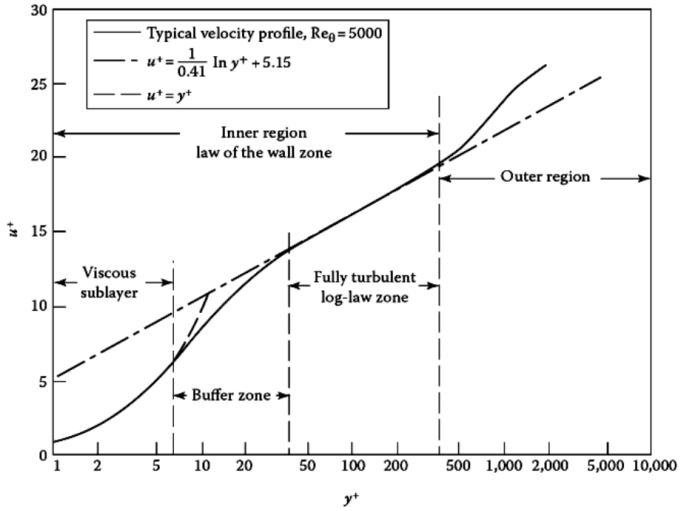

Figure 4.2: Turbulent boundary layer for a typical incompressible flow over a smooth flat plate showing various layers.
[Reprinted from *"Numerical and experimental investigations of the noise and performance characteristics of a radial fan with forward-curved blades"*, by Darvish M. [34]. © Copyright 2023 by ResearchGate GmbH.]

surface, in order to solve the wall boundary layer as accurately as possible. It allows to take in account the fluid dynamics phenomena in the viscous

sub-layer, also note that for transition modeling it needs mesh with $y^+ < 1$ where is necessary along with the requirement of fine mesh in stream-wise direction.
It is possible to derive the dimensional wall-distance y from its dimensional value y^+:

$$y^+ = \frac{u_* y}{\nu}$$

Where u_* is the friction velocity at the nearest wall. Dimensional analysis shows that at a wall a charateristic velocity, u_*, can be defined in the following way:

$$u_* = \sqrt{\tau_w / \rho}$$

Where $\tau_w = \mu \left(\frac{\partial u}{\partial y}\right)_{y=0}$ is the wall shear stress and ρ is the fluid density at the wall.
While, y is the distance to the nearest wall and ν is the local kinematic viscosity of the fluid.
To estimate the required distance y of the first cell from the wall, we compute the Reynolds number:

$$Re = \frac{\rho \cdot U_{FreeStream} \cdot L_{BoundaryLayer}}{\mu}$$

We estimate the skin friction using the Schlichting skin-friction semi empirical correlation:

$$C_f = [2 \log_{10} Re_x - 0.65]^{-2.3} \qquad \text{for} \quad Re_x < 10^9$$

This relation is derived assuming the flat plate to be completely turbulent over its entire length.
The wall shear stress is defined as:

$$\tau_w = C_f \cdot \frac{1}{2} \rho U_{fs}^2$$

Finally, the wall distance:

$$y = \frac{y^+ \mu}{\rho u_*}$$

This allows for an approximate assessment of the maximum width of the cells close the walls so that the mesh is refined enough to capture the fluid dynamics phenomena within the boundary layer.
The lines in the mesh that connect the axis to the outer wall take advantage of the *transfinite* scaling available in GMSH to increase resolution, such as near the outer wall. This command allows structuring the mesh in the vertical direction according to a geometric sequence. The distribution of cells

follows a sequence in which the ratio between the height of an element and its predecessor remains constant: $a + ar + ar^2 + ar^3 + ...$ Where a is the coefficient of each term and r is the common ratio between adjacent terms. Every coefficient in the geometric series is the same. The sum of the first n terms of a geometric series, up to and including the r^{n-1} term, is given by the closed-form formula:

$$S_n = ar^0 + ar^2 + ar^2 + ... + ar^{n-1} = \sum_{k=0}^{n-1} ar^k = \sum_{k=1}^{n} ar^{k-1} = \begin{cases} a\left(\frac{1-r^n}{1-r}\right) & \text{for } r \neq 1 \\ an & \text{for } r = 1 \end{cases}$$

The finite series is defined by any combination consisting of three of the following parameters: coefficient a, it is the first term of the series, the common ratio r, the sum S_n and the number of terms in the series n.
In the creation of a structured mesh according to the geometric series, these parameters can also be expressed in terms of the total length of the vertical curve to be discretized, the number of cells in which the curve is subdivided, the total expansion ratio, the cell-to-cell expansion ratio, also known as the common ratio, the width of the start cell, and the width of the end cell. Three out of these six values can be explicitly defined, and the remaining three values are calculated based on them [35]. Figure 4.4 show the mesh used for the present numerical simulations, respectively for the convergent and convergent-divergent configuration. A zoomed-in version of the actual meshes are also represented to show the higher grid resolution near the ejector walls.

4.2.2 Numerical Solver

The `thermophysicalProperties` dictionary is read by any solver that uses the *thermophysical* model library. A thermophysical model is constructed in OpenFOAM as a pressure-temperature system from which other properties are computed. There is one compulsory dictionary entry called `thermoType` which specifies the complete thermophysical model that is used in the simulation.
The basic thermophysical properties are specified for each species from input data.
The working fluid is dry air, so in `specie` is contained the number of moles, `nMoles`, of the specie and the molecular weight, `molWeight`, for the air. It is assumed to have the properties of a calorically perfect gas, for with

$$p = \rho RT \qquad e = c_v T = (\gamma - 1)RT$$

With:

$$R = 287.058\ J/(kg \cdot K) \qquad \gamma = 1.4$$

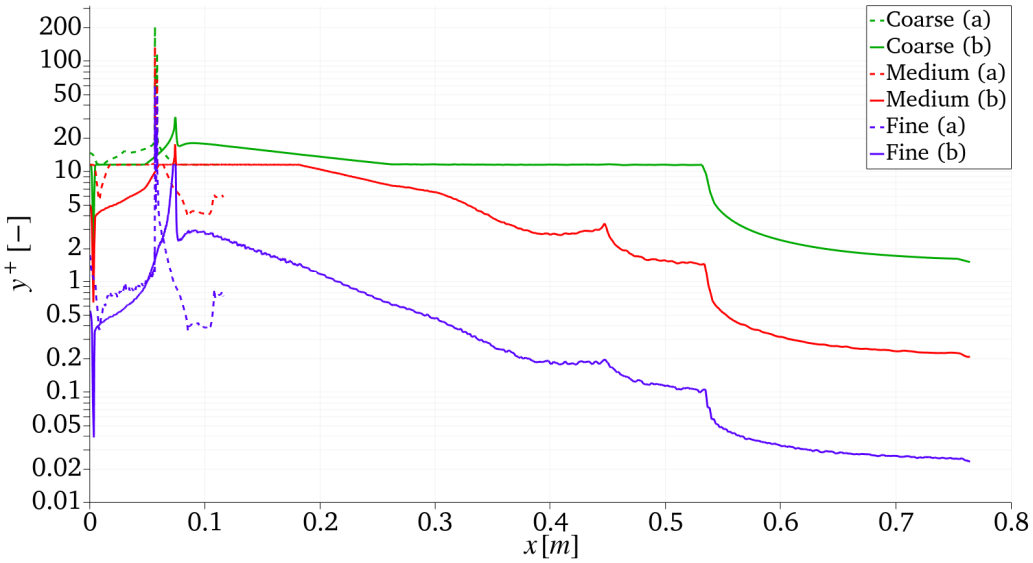

(a) Convergent Primary Nozzle

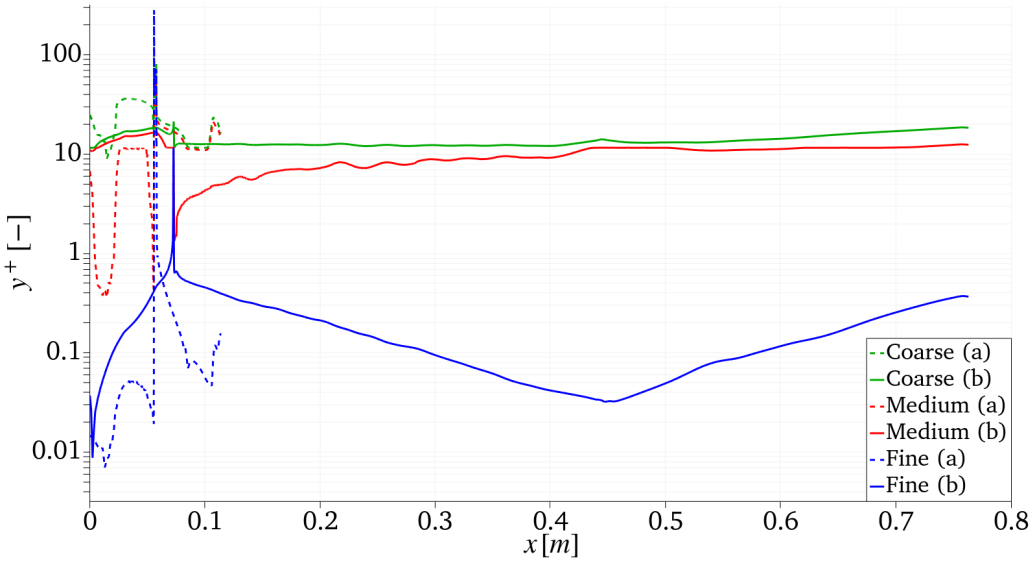

(b) Convergent-Divergent Primary Nozzle

Figure 4.3: y^+ close to wall for "Test012".

Figure 4.4: An overall vision and detail of the grid structure of the computational domain for the numerical simulations: (a) Convergent Primary Nozzle; (b) Convergent-Divergent Primary Nozzle.

Where R is the gas constant and $\gamma = c_p/c_v$, is the ratio of specific heats at constant pressure and volume, c_p and c_v respectively.
For the the transport modelling concerns evaluating dynamic viscosity μ, thermal conductivity k, and thermal diffusivity α (for internal energy and enthalpy equations). The current transport model chosen is based on the Sutherland's law, a formula for temperature-dependent transport properties. It calculates μ as a function of temperature T from a Sutherland coefficient A_s and Sutherland temperature T_s, specified by keywords `As` and `Ts`; μ is calculated according to:

$$\mu = \frac{A_s\sqrt{T}}{1 + T_s/T}$$

For air $A_s = 1.458 \cdot 10^{-6}\ kg \cdot \sqrt{K}/(m \cdot s)$ and $T_s = 110.4\ K$.
Then, in `thermodynamics` are specified the thermophysical properties of the species, derived from the isobaric specific heat $c_p = 1004.5\ J/(kg \cdot K)$ and the heat fusion $H_f = 0\ J/kg$. This scheme solves the compressible Reynolds-Averaged Navier-Stokes (RANS) equations with common approximations [36]. For the present numerical results, the effects of turbulence are accounted for using the wall-resolved k-ω Shear Stress Transport (SST) [37] turbulence model with a turbulent Prandtl number, `Prt`, set to 0.85 [38].
. In general, the k-ω SST model generally performs best [39]. The general parameters have been found to yield the best agreement with the experimental measurements concerning both global and local flow quantities in many studies [40] [41] [42] [43].
Then, the spatial discretizations of both the conservation and turbulence equations are set to be second-order accurate in the file `fvSchemes` and `fvSolution` in the *system* directory in OpenFoam.

4.2.3 Control

The time step for this simulation was chosen dynamically using the `adjust TimeStep` keyword within the control file. This allows to simulation to increase the time step until the Courant number reaches a specified limit; the Courant–Friedrichs–Lewy (CFL) condition ensures the acoustic waves and flow physics are properly tracked by the solver. The CFL number is consistently set to a range of 0.5 for all operating conditions, chosen to ensure stability. At most points during the simulation, the time step is around $1 \cdot 10^{-8}\ s$.
As previously stated, the solver employed for the CFD calculations operates in a transient mode. In this study, the convergence criterion for each simulation is based on the relative difference between the mass flow rates of

the computational domain. Once this difference between three time steps (`purgeWrite` set to 3) stabilizes to within 0.5%, the solver is considered to have reached a steady-state solution:

$$\varepsilon = \left| \frac{\dot{m}_{in} - \dot{m}_{out}}{\dot{m}_{in}} \right| < 5 \cdot 10^{-3}$$

Once the latter is stabilized between $\pm$ 0.05%, the solver is assumed to have reached the steady-state solution. To validate this criterion, the average pressure field for three next time steps is also assessed, taking into account the corresponding standard deviation. This highlights parts of the simulation which still vary considerably.
In the paper by [28], the authors state that the simulation should run at least 20 characteristic flow times to reach steady state, obtained from the average speed of the flow and the length of the domain.
An example of the characteristic time for the converging-diverging configuration for "Test012" is provided. In this case, the average velocity in the domain in x-direction is $\overline{U}_x = 211\ m/s$ and the length of the computational domain along the same axis is $L_x = 0.657\ m$. The minimum final acquisition time equals to the following value:

$$t_{end} = L_x/\overline{U}_x \cdot 20 \sim 0.062\ s$$

4.2.4 Boundary and Initial Conditions

The boundary conditions for this problem were defined using the physical regions defined the by Python script.
First of all, the geometric (constraint) patch types must be specificated in the *constant/polyMesh/boundary* file. We first need to consider that, for the purpose of applying boundary conditions, a boundary is generally broken up into a set of patches. One patch may include one or more enclosed areas of the boundary surface which do not necessarily need to be physically connected. A type is assigned to every patch as part of the mesh description, as part of the *boundary* file. It describes the type of patch in terms of geometry or a data communication link [44].
The two faces of the wedge use the `wedge` boundary condition for all parameters, making the assumption of cylindrical symmetry. It enforces a geometrical constraint, in particular a cyclic condition between a pair of boundaries for the 2D geometries.The axi-symmetric wedge planes must be specified as separate patches of wedge type. For the outer wall is imposed the `wall` patch type. For the secondary and primary inlets, and for the outlet from the diffuser, respectively indicated with `inlet` and `outlet`.

In terms of input requirements, the mandatory fields are the pressure $[Pa]$, the velocity $[m/s]$ and the temperature $[K]$, the turbulent kinetic energy $[m^2/s^2]$ and the specific turbulence dissipation rate $[1/s]$, for each physical region.

4.2.4.1 Pressure

The inlet boundary uses the `totalpressure` boundary which is useful for inlets where the velocity is not known a priori. This condition sets the pressure equal to a constant for outflow (a standard outflow boundary), but allows it to find its own value for inflow. The outlet boundary uses the `waveTransmissive` boundary to avoid spurious wave reflections off of the boundary and define the pressure difference across the ejector. The choice of the pressure difference, along with the cross sectional area of the nozzle, between the inlet and the outlet is what sets the velocity and temperature distribution within the nozzle.
The total pressure is imposed at the primary nozzle and secondary nozzle's inlet sections and the static pressure at the outlet section of the ejector, in Table 4.2.
For all tests in the conducted study, the following condition has been imposed at the outlet (with specified the static pressure for the "Test012"):

```
outlet
{
    type            waveTransmissive;
    gamma           1.4;
    fieldInf        231128;
    lInf            0.001;
    value           uniform 1000;
}
```

Where:

- `fieldInf` is the field (the pressure in this case) at infinity;
- `lInf` is the relaxation length used to calculate the strength of the reflecting wave when considering partially non-reflecting boundary conditions.

The `lInf` parameter regulates the extent of the reflected wave, ideally representing the distance after which the field will reach the `fieldInf` value

assigned by the user. This implies that the larger `lInf` the lower the reflection at the boundaries will be. However, an extremely high value of `lInf` is not recommendable since the complete lack of a constraint on the value of the pressure would lead to a full supersonic solution because of the pressure is set free, and, therefore, to a drift in the value of the pressure inside the computational domain.
The parameter `lInf` is at the user's discretion, and there is no unique method for choosing the most appropriate value to assign. In this study, investigations were conducted with two different `lInf` values: 0.1 and 0.001. It was found that for the `lInf` value of 0.001, the pressure field that converges at the outlet is overall closer to the point pressure value obtained from the experimental campaign.

4.2.4.2 Velocity

The inlet and outlet both use a `zeroGradient` boundary condition. This allows the velocity distribution to be extrapolated to the boundaries from the conditions within the nozzle, which in the most part are governed by the difference in pressure accross the ejector. `noSlip` conditions for the velocity are specified on the ejector wall.

4.2.4.3 Temperature

The inlet boundary uses a `fixedValue` condition. The outlet boundary uses a `zeroGradient` boundary condition under the same premise as the velocity; the flow is allowed to evolve naturally under a fixed temperature gradient.

4.2.4.4 Turbulent Kinetic Energy

For both inlets, the condition of `turbulentIntensityKineticEnergyInlet` is imposed. It sets the turbulent kinetic energy based on the patch velocity and user-supplied turbulence intensity sets as 5% turbulence intensity:

$$k = 1.5(\underline{\boldsymbol{I}}|\boldsymbol{U'}|)^2$$

k is defined to be half the sum of the variances (square of standard deviations) of the velocity components. At the wall, a `omegaWallFunction` condition is set, which provides a wall constraint on the turbulent kinetic energy, with default parameters. It is the low Reynolds wall function for k and it computes y^+ of the first cell, in order to compute the correct wall friction based on the y+ y^+ (different behaviour in the different regions of the BL). For the outlet, again the `zeroGradient` condition is applied, along with the `wedge` condition for the top and bottom physical groups.

4.2.4.5 Specific Turbulence Dissipation

The specific turbulence dissipation, ω is the rate at which turbulence kinetic energy is converted into thermal internal energy per unit volume and time. All boundary conditions are set as those for k, except for inlets and walls. For the primary and secondary inlets, the `turbulentMixingLengthFrequencyInlet` condition is specified. It sets the turbulent specific dissipation rate based on the patch turbulence kinetic energy and user-supplied mixing length:

$$\omega = \frac{k^{0.5}}{C_{\mu}^{0.25} L}$$

Where C_μ is a model parameter set to 0.09 [37] and L is the mixing length obtained for each inlet by $L = 0.07 \cdot D$, with D the diameter of the corresponding inlet [21].

4.2.5 Grid Convergence

The Figure 4.3 shows the trend of the value of y^+ on the wall for three mesh, one finer than the other, for the "Test012" with the C and CD configurations, in order to carry out a convergence study of the grids, which in subsequently examined in depth. In (a), the reference is made to the segment of the physical wall group that includes the primary nozzle, the step, and the upper wall of the mixing chamber. On the other hand, in (b), it denotes the segment of the physical group formed by the upper wall of the secondary inlet and the entire wall of the mixing chamber, constant area part, and the diffuser. For each case, a grid convergence study is performed to get minor differences between the final and the previous adaptation step. In our case, the method involves performing the simulation on three successively finer grids. Three grids are utilized, with the first initialized based on the initial conditions and the subsequent ones initialized from the motion field of the finer grid using the `mapfields` command.
The grid convergence study is done for three mesh sizes: *coarse*, *medium*, and *fine* mesh. In the initial mesh (coarse) domain the cells close to the primary nozzle and walls are small enough to capture the complex flow phenomenon. In order to better predict the internal flow, mesh refinement is employed. In the medium-mesh domain more cells are added at locations with significant flow changes. A common approach is to refine everywhere with a certain factor, as we did in the C configuration with a factor 2; instead, for the CD configuration, only the wall regions were refined to achieve the desired y^+ value. The fine mesh accounts a high elements number enabling the flow field features to be better resolved. The grid is also refined in the near-wall regions

to capture the boundary layer and the region between the primary nozzle exit and entry of the mixing chamber to capture the shock train with exponential stretching in the x-direction and y-direction. A summary overview of the refinement of the meshes is shown in the Table 4.1.

Hexahedra Elements Number		
	C	**CD**
Coarse	33158	93743
Medium	124703	103189
Fine	414070	141859

Table 4.1: Overview of the hexahedra elements for the three mesh for C and CD primary nozzle configuration.

The variation in Mach number on the centerline is illustrated in Figure 4.5, and it is employed to ascertain a converged solution for the grid. The results acquired from the fine mesh prove adequate for achieving grid convergence under the specified conditions. Consequently, the fine mesh is employed for all simulations.

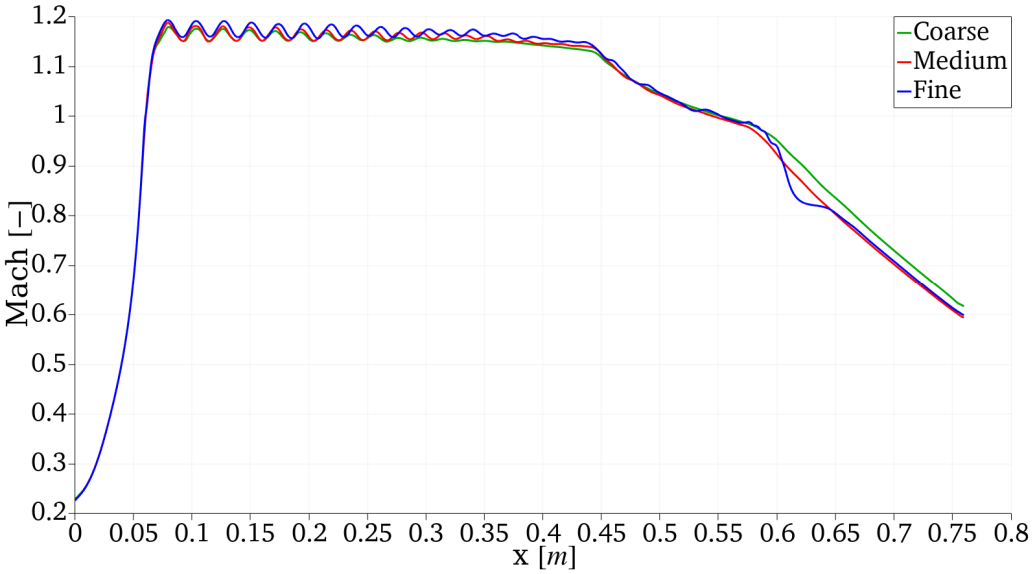

(a) Convergent Primary Nozzle

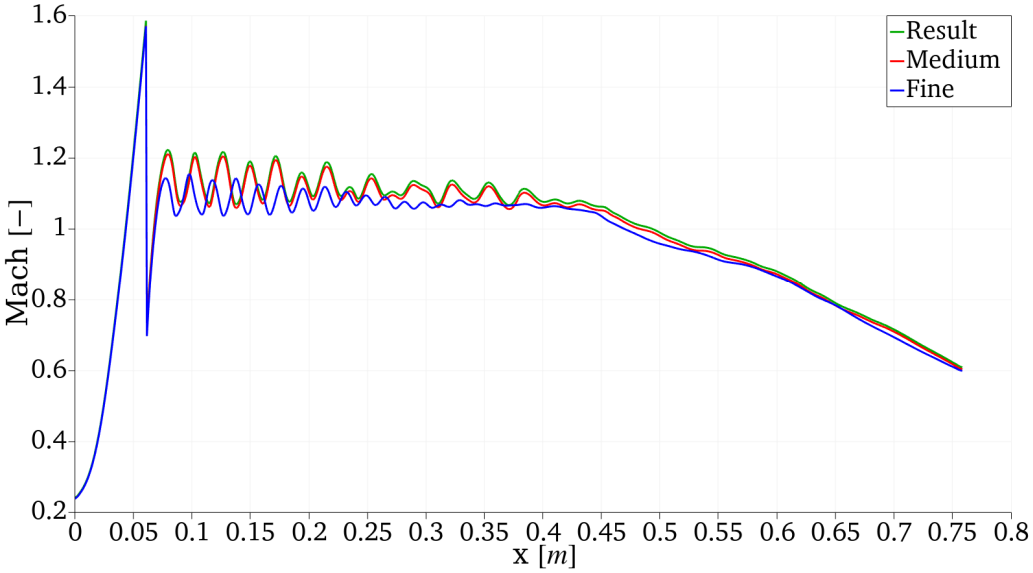

(b) Convergent-Divergent Primary Nozzle

Figure 4.5: Centerline Mach number for "Test012".

4.3 Results

Starting from the conducted experimental campaign in the Chapter 2, the set of experimental values pertaining to the operating condition $p_{s,0}/p_{p,0} = 0.54$ is selected. This set comprises four tests, and their values are detailed in Table 4.2.

Test	T_p	T_s	$p_{p,0}$	$p_{s,0}$	Π $[-]$	p_b	$\dot{m}_s$	$\dot{m}_p$
012	295	294	394584	20824	0.528	231128	0.429	0.571
013	295	293	394581	210400	0.533	234885	0.427	0.573
014	295	293	394841	210440	0.533	237863	0.419	0.573
015	294	293	395253	213397	0.540	242800	0.413	0.573
016	294	293	394446	213380	0.541	242186	0.413	0.569

Table 4.2: Input values for CFD simulations related to the experimental campaign (temperature u.m.: $[K]$; pressure u.m.: $[Pa]$; mass flow rate u.m.: $[kg/s]$).

The ER results from the CFD simulations will be compared with experimental for the ejector configurations, with a convergent and a convergent-divergent primary nozzle. Subsequently, the performances and flow topologies of the CFD simulations for cases C and CD will be compared.

In the Figure 4.6, the entrainment ratio, the mass flow rates, $\dot{m}_s$ and $\dot{m}_p$, values obtained from CFD simulations are presented for various operating conditions, varying the backward pressure for a fixed ratio of approximately $\Pi = 0.54$, as reported in the Table 4.2. CFD tests were conducted for both C and CD configurations of the ejector and compared with experimental data collected for the C configuration.

We observe that the CFD results for both configurations deviate from the experimental ones. Particularly for the C configuration of the ejector, the entrainment ratio CFD results deviate from the experimental ones on average by 15%. This behavior could be attributed to numerous factors. One of these might be the incomplete attainment of steady-state conditions for the fluid dynamic quantities of interest measured in the experimental campaign. Moreover, the overall mass flow rate involved in the ejector is close to 1 kg/s. It is possible that the observed mass flow rates in the CFD are not reachable with the compression system of the facility. Hence, the experimental and numerical conditions might differ. Additionally, CFD simulations involve a simplified modeling of the real problem, which can negatively impact the accuracy of numerical results compared to experimental ones. In fact, the real facility is affected, for example, by wall imperfections or roughness

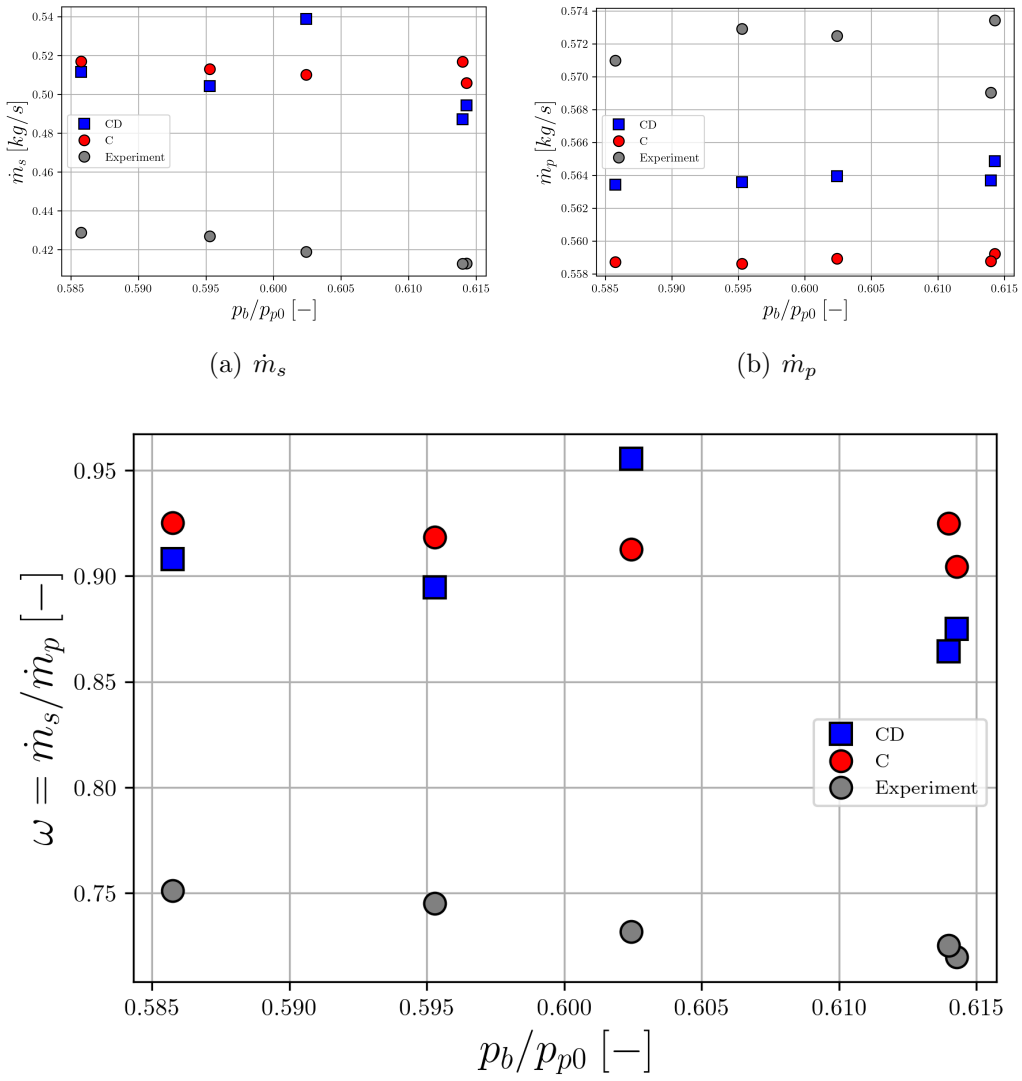

(a) $\dot{m}_s$

(b) $\dot{m}_p$

(c) ER

Figure 4.6: CFD Results for C and CD configurations compared with experimental data.

that are not taken into account in the computational simulations. Moreover, through the numerical model employed by the CFD solver, transient behaviors or numerical instabilities that are not present in physical reality may arise, affecting the convergence of the numerical simulation. CFD results are naturally sensitive to the imposed boundary conditions. In particular, point values of pressure have been set at the inlets and outlet, derived from a radial estimate of static pressure measured by sensors susceptible to errors. This enforces an average value with uncertainty across an entire computational surface in the CFD simulation. Additionally, the chosen turbulence model is expected to have a certain impact. In fact, in this study, the $k-\omega$ SST model is used, as mentioned in Section 4.2.2. Changing the turbulence model, for example, to the $k-\epsilon$ model, yield different results that might be closer to reality.
In Figure 4.6 (a), the CFD results of the secondary mass flow rate for both configurations and the experimental data for the convergent geometry are shown. It can be observed that the values of $\dot{m}_s$ are generally decreasing for larger values of p_b/p_{p0}, indicating that under these boundary conditions, the ejector is in off-design conditions for both the configurations. On the other hand, in Figure 4.6 (b), the trend of the primary mass flow rates, $\dot{m}_p$, is essentially constant in the CFD simulations. This suggests that the primary stream is at its maximum for both primary nozzle configurations and choked for all operating conditions, but the two values of $\dot{m}_p$ in the two configurations, under the same boundary conditions, do not perfectly coincide. The CD configuration has a higher value compared to case C; this could be attributed to minor friction losses along the primary duct. It is noted that the percentage error between the two configurations of the primary mass flow rate is approximately 1%. Instead, Figure 4.6 suggests that the result for "Test014" in the CD configuration is anomalous because it has not yet reached complete convergence due to time constraints.

4.3.1 Flow topology features

The mean-flow Mach number is represented for "TEST012" in Figure 4.7 with the sonic line, which is the iso-contour of mean-flow Mach number unity for the C configuration in the upper half, and CD configuration in the lower half. It can be seen that the flow becomes sonic near the throat of the primary nozzle for both of them. The supersonic region extends in the mixing duct and in the initial portion of the diffuser, where it progressively vanishes in a shock-train. For this particular case, two Compound-like regime patterns can be identified at the beginning of the mixing duct, as said in Section 3.3.2.2. In fact, the Fabri-choking pattern should feature the sonic line in a

hypothetical throat, which is not present in this case, so there is not a choked zone for the second flow. Indeed, there is no vertical part of the sonic line between the supersonic flow around the axis and the wall at the exit of the secondary pipe.
Figure 4.8 displays a numerical schlieren image of the whole ejector for the C and CD configuration, respectively in the upper and lower half, still for the "TEST012". The former is obtained by computing the axial derivative of the field flow density $\frac{\partial \rho}{\partial x}$. The schlieren image allows to visualize gasdynamic discontinuities and waves (compression waves and shockwaves being displayed in dark/black, and rarefaction fans in light/white). As seen in Figure 4.8, the primary flow is over-expanded when it exits its nozzle. That is visible in the Mach contour in Figure 4.7 and from the narrow dark area in Figure 4.8. A Prandtl-Meyer rarefaction fan then accommodates the primary flow to the secondary stream static pressure by further expanding it. The supersonic flow pattern that follows is then highly two-dimensional.
In Figure 4.9,it is also interesting to represent the derivative with respect to the y-direction of the density, $\frac{\partial \rho}{\partial y}$, to appreciate the boundary layer established at the wall and the shear layer formed between the two streams. In light color, the shear layers that develop in the flow field are highlighted, for example because the density of the primary jet is higher than that of the secondary.

In Figure 4.6, the entrainment ratios observed for the convergent configuration is bigger than the convergent-divergent configuration ones. This is contrary to the expected results. In fact, from the flow topology for the converging-diverging configuration in Figure 4.10, it exhibits a flow field with higher velocity and more significant dynamic gas structures compared to the simply converging case. The secondary inlet of the converging-diverging geometry is 1 mm narrower than in the diverging case. This results in a lower $\dot{m}_s$ value and a similar $\dot{m}_p$ (because the throat is identical) value compared to the converging case, as shown in Table 4.3.

		Test012	Test013	Test014	Test015	Test016
C	$\dot{m}_s\ [kg/s]$	0.5169	0.5131	0.5101	0.5059	0.5169
	$\dot{m}_p\ [kg/s]$	0.5587	0.5586	0.5589	0.5592	0.5588
	$\omega\ [-]$	0.9252	0.9184	0.9127	0.9127	0.9250
CD	$\dot{m}_s\ [kg/s]$	0.5116	0.5042	0.5388	0.4943	0.4872
	$\dot{m}_p\ [kg/s]$	0.5634	0.5636	0.5639	0.5649	0.5637
	$\omega\ [-]$	0.5637	0.8946	0.9555	0.8751	0.8644

Table 4.3: Primary and secondary mass flow rates, and entrainment ratios from CFD results.

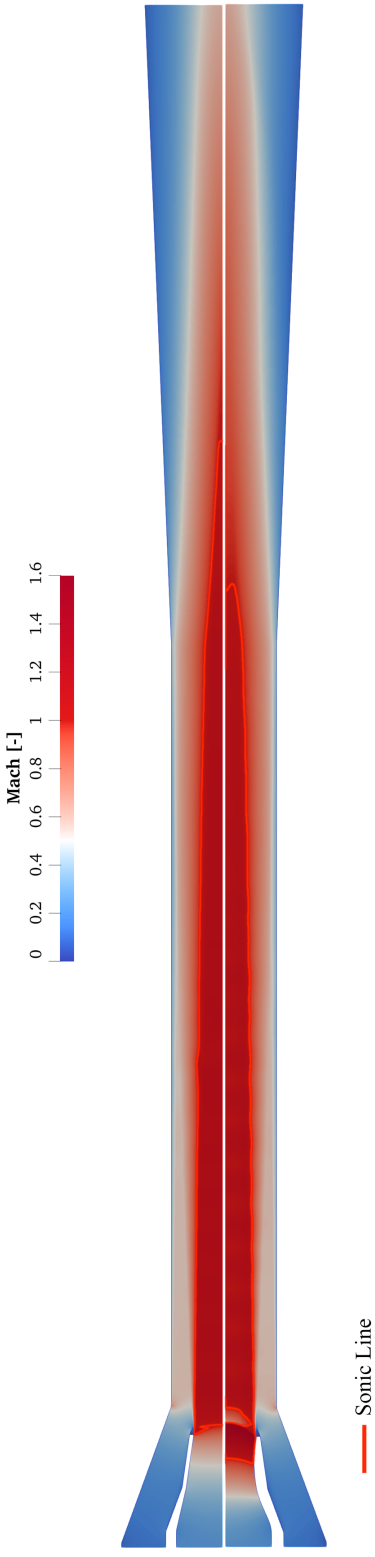

Figure 4.7: Upper half: Mean-flow Mach number field and sonic line for Convergent configuration. Lower half: Mean-flow Mach number field and sonic line for Convergent-Divergent configuration.

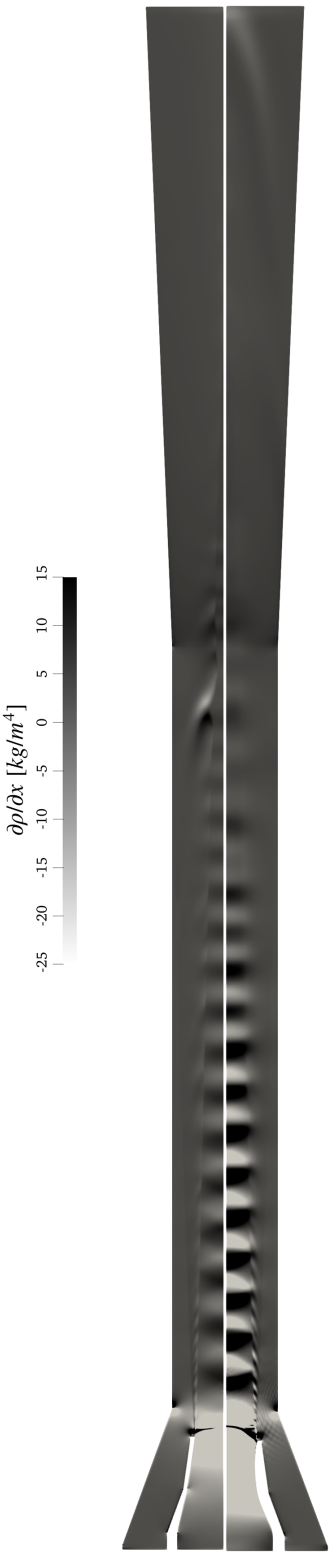

Figure 4.8: Numerical schlieren (axial derivative of the density field) image of the flow. Shock-wave and compression regions are shown in dark, expansion fans and regions are shown in light. Upper half: Convergent configuration. Lower half: Convergent-Divergent configuration.

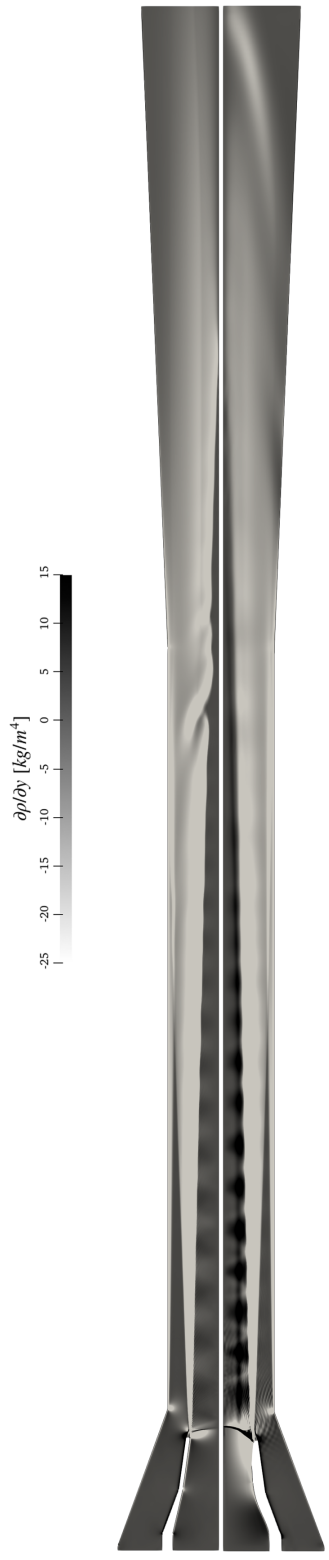

Figure 4.9: Numerical schlieren (radial derivative of the density field) image of the flow. The shear layers are shown in light. Upper half: Convergent configuration. Lower half: Convergent-Divergent configuration.

Following these observations, in Figure 4.10, it is useful to represent the velocity profile along the x-axis, density, and the product ρU_x (which contributes to the calculation of mass flow rates) at the exit section of the secondary pipe and the primary nozzle.

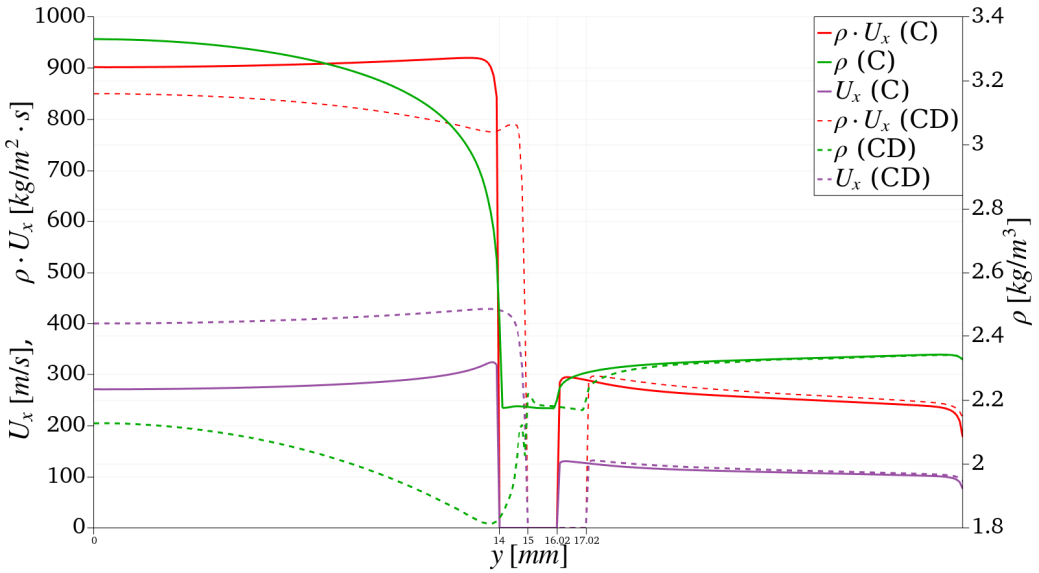

Figure 4.10: Primary nozzle and secondary pipe exit flow fields for "Test012". Exit primary nozzle (CD): $[0; 15]\,mm$; Exit secondary pipe (CD): $[17.02; 30]\,mm$ Exit primary nozzle (C): $[0; 14]\,mm$; Exit secondary pipe (C): $[16.02; 30]\,mm$ Solid Line: C configuration; Dash Line: CD configuration.

The velocity in the primary nozzle and the secondary pipe is higher for the CD configuration, unlike the density. The density is lower due to the higher expansion of the primary flow through the diverging section of the nozzle.

Chapter 5

Conclusion

From the comparison in the Figure 4.6 of experimental and numerical data, it can be concluded at the end of this Chapter that the data collected from the experimental campaign and those resulting from CFD simulations are both affected by errors that cause the two types of data to deviate from each other.

In fact, all the data collected in the experimental campaign could be subject to a systematic error attributable to various factors, such as compression capacity. Furthermore, CFD simulations were obtained with a simplified model of reality. These two different sources of uncertainty result in a discrepancy between experimental and numerical data.

Instead, from the comparison of the performances obtained with CFD between the C and CD configurations of the ejector, the complexity of the fluid dynamic phenomena involved inside the ejector is evident. In fact, contrary to initial expectations, it was determined that the difference in the cross-section area of the secondary pipe for the two configurations significantly influences the results.
Despite the slightly higher secondary velocity and the mass flux, the secondary mass flow rate decreased for the CD configuration compared to the C because of the narrower flow passage, so the CD configuration has a lower ER value than that of the C configuration, whose primary nozzle geometry is simpler and determines a larger passage section for the secondary flow. The comparison of the performances of the two configurations is not complete but would require a more in-depth CFD study in terms of the range of operating conditions, which requires greater time resources. In addition, due to time constraints, it was not possible to complete the experimental setup with the CD configuration, which would have facilitated the comparison between the two setups and could have provided more insights into the numerical results as well.

Further research is needed to explore this aspect, particularly concluding this discussion by wondering what would be expected from the performances of two configurations compared, C and CD, but with the same passage section for the secondary flow, at the expense of the throat section for the CD configuration, which would have a lower primary mass flow rate.
In particular, in future work, it would be desirable to take more regarding the maximal mass flow rate achievable in the facility, leveraging the compressor's capacity. The latter has constrained the performance of the supersonic ejector and could represent a crucial step toward matching experimental and computational fluid dynamics data.

Bibliography

1. Aphornratana, S. "Theoretical Study of a Steam-Ejector Refrigerator". *RERIC International Energy Journal* **18** (1996).
2. Aidoun, Z., Ameur, K., Falsafioon, M. & Badache, M. "Current Advances in Ejector Modeling, Experimentation and Applications for Refrigeration and Heat Pumps. Part 1: Single-Phase Ejectors". *MDPI Journals Awarded Impact Factor* (2019).
3. Zegenhagen, M. & Ziegler, F. "A one-dimensional model of a jet-ejector in critical double choking operation with R134a as a refrigerant including real gas effects". *International Journal of Refrigeration* (2015).
4. Metsue, A., Debroeyer, R., Poncet, S. & Bartosiewicz, Y. "An improved thermodynamic model for supersonic real-gas ejectors using the compound-choking theory". *Elsevier Ltd.* (2021).
5. Dong, J., Song, H., Yu, M., Yu, M. & Wang, W. Numerical Investigation of Miniature Ejector Refrigeration System Embedded with a Capillary Pump Loop. *ResearchGate GmbH.* (2017).
6. Kumar, V., Yadav, S. & Ram, S. "A comprehensive studies on constant area mixing (CAM) and constant pressure mixing (CPM) Ejectors: A review". *Elsevier Ltd.* (2022).
7. Aidoun, Z., Ameur, K., Falsafioon, M. & Badache, M. Current Advances in Ejector Modeling, Experimentation and Applications for Refrigeration and Heat Pumps. Part 1: Single-Phase Ejectors. *Inventions, MDPI* (2019).
8. Eames, I., Wu, S., Worral, M. & Aphornratana, S. "An experimental investigation of steam ejectors for applications in jet-pump refrigerators powered by low-grade heat". *J. Power Energy* **213** (1999).
9. Carlomagno, G. M. *""Elementi di gasdinamica"* (Liguori, 2009).
10. Bouhanguel, A. *"Etude numérique et expérimentale de l'interaction entre deux écoulements compressibles dans un éjecteur supersonique"* (Université de Franche-Comté, 2013).

11. Fabri, J. & Siestrunck, R. Supersonic air ejectors. *Elsevier* (1958).

12. Matsuo, K. "Investigation of supersonic air ejectors : Part 2. effects of throat-arearation on ejector performance." *Japan Society of Mechanical Engineers* **25** (1982).

13. Matsuo, K., Miyazato, Y. & Kim, H. "Shock train and pseudo-shock phenomena in internal gas flows". *Prog. Aerosp. Sci.* **35** (1999).

14. GmbH, H. M. *"Instruction Manual DVH / DVE"* English. Thorlabs (2019). 127 pp.

15. ENGINEERING, V. *DP15 Variable Reluctance Differential Pressure Transducer* English (2018).

16. A., A. Influence of temperature on ejector refrigeration technique: a review. *International Journal of Advanced Research in Engineering and Technology (IJARET)* (2020).

17. Keenan, J. H. & Neumann, E. P. A Simple Air Ejector. *Journal of Applied Mechanics* **9** (1942).

18. Keenan, J. H., Neumann, E. P. & Lustwerk, F. An Investigation of Ejector Design by Analysis and Experiment. *Journal of Applied Mechanics* **17** (1950).

19. Huang, B., Chang, J., Wang, C. & Petrenko, V. A 1-D analysis of ejector performance. *Int. J.Refrigeration22* **5** (1999).

20. Chen, W. *et al.* Theoretical analysis of ejector refrigeration system performance under overall modes. *Appl Energy* (2017).

21. Lamberts, O., Chatelain, P. & Bartosiewicz, Y. "Numerical and experimental evidence of the Fabri-choking in a supersonic ejector". *Int J Heat Fluid Flow* (2018).

22. Bernstein, A., Heiser, W. & Hevenor, C. Compound-compressible nozzle flow. *J Appl Mech* (1967).

23. Chen, X., Omer, S., Worall, M. & Riffat, S. Recent developments in ejector refrigeration technologies. *Renew Sustain Energy* (2013).

24. "The compound-choking theory as an explanation of the entrainment limitation in supersonic ejectors". *Energy* **158** (2018).

25. Delbecque, L. *"Calibration strategy of a 1D model for supersonic ejectors"* Master [120] in Mechanical Engineering (École polytechnique de Louvain, 2022).

26. Weller, H. G., Tabor, G., Jasak, H. & Fureby, C. A tensorial approach to computational continuum mechanics using object-oriented techniques. *Comput. Phys.* **12** (1998).

27. Ltd, T. O. F. *OpenFOAM* `https://openfoam.org`.

28. Greenshields, C., Weller, H. & Gasparini, L. Implementation of semi-discrete, non-staggered central schemes in a colocated, polyhedral, finite volume framework, for highspeed viscous flows. *'International Journal for Numerical Methods in Fluids* **63** (2010).

29. Kurganov, A., Noelle, S. & Petrova, G. Semi-Discrete Central-Upwind Scheme for Hyperbolic Conservation Laws and Hamilton—Jacobi Equations. *SIAM Journal on Scientific Computing* (2001).

30. Schmitt, F. About Boussinesq's turbulent viscosity hypothesis: historical remarks and a direct evaluation of its validity. *Comptes Rendus Mécanique* (2007).

31. Favre, A. Statistical equations of turbulent gases. *Problems of hidrodynamics and continuum mechanics* (1969).

32. Kurganov, A. & Tadmor, E. New high-resolution central schemes for nonlinear conservation laws and convection-diffusion equations. *Communications in Computational Physics Journal of Computational Physics* (2001).

33. Geuzaine, C. & Remacle, J.-F. Gmsh: A 3-D finite element mesh generator with builtin pre-and post-processing facilities. *Int. J. Numer. Methods Eng.* **79** (2009).

34. M., D. Numerical and experimental investigations of the noise and performance characteristics of a radial fan with forward-curved blades. *ResearchGate GmbH.* (2015).

35. OpenFOAMWiki.net. *Scripts/blockMesh grading calculation* `https://openfoamwiki.net/index.php/Scripts/blockMesh_grading_calculation`.

36. Lamberts, O., Chatelain, P. & Bartosiewicz, Y. New methods for analyzing transport phenomena in supersonic ejectors. *International Journal of Heat and Fluid Flow* **64** (2017).

37. Menter, F. Two-equation eddy-viscosity turbulence models for engineering applications. *AIAA J.* **32** (1994).

38. Wilcox, D. *Turbulence Modeling for CFD* (DCW Industries, Incorporated., 2006).

39. Mazzelli, F., Little, A. B., Garimella, S. & Bartosiewicz, Y. "Computational and experimental analysis of supersonic air ejector: Turbulence modeling and assessment of 3D effects". *Elsevier Ltd.* (2015).

40. Bartosiewicz, Y., Aidoun, Z., Desevaux, P. & Mercadier, Y. CFD-experiments integration in the evaluation of six turbulence models for supersonic ejectors modeling. *Integrating CFD and Experiments Conference, Glasgow, UK.* (2003).

41. Del Valle, J., Jabardo, J., Ruiz, F. & Alonso, J. A one dimensional model for the determination of an ejector entrainment ratio. *Int. J. Refrig.* (2012).

42. Croquer, S., Poncet, S. & Aidoun, Z. Turbulence modeling of a single-phase r134a supersonic ejector. Part 1: numerical benchmark. *Int. J. Refrig.* (2016).

43. Besagni, G. & Inzoli, F. Computational fluid-dynamics modeling of supersonic ejectors: screening of turbulence modeling approaches. *Appl. Therm. Eng.* (2017).

44. Greenshields, C. *OpenFOAM v9 User Guide - 5.2 Boundaries* `https://doc.cfd.direct/openfoam/user-guide-v9/boundaries`.

Appendix A

Analytical Model

A.1 Listing: Metsue's 0D thermodynamic model Python code

```
import numpy as np
from scipy.optimize import fsolve
from scipy import optimize as opt
import matplotlib.pyplot as plt
from scipy.interpolate import CubicSpline
import pandas as pd

ProcessedData = pd.read_excel('ProcessedData.xlsx')

### Experimental Data Set ###
i1  = np.array(range(  0,  6))
i2  = np.array(range(  6, 11))
i3  = np.array(range( 11, 17))
i4  = np.array(range( 17, 30))
i5  = np.array(range( 30, 46))
i6  = np.array(range( 46, 50))
i7  = np.array(range( 50, 59))
i8  = np.array(range( 59, 69))
i9  = np.array(range( 69, 79))
i10 = np.array(range( 79, 90))
i11 = np.array(range( 90,102))
i12 = np.array(range(102,117))

# Entrainment Ratio
ER_exp  = ProcessedData['ER']
# Back static Pressure / Primary Flow Total Pressure
tau     = ProcessedData['P3/P02']
# Secondary Flow Total Pressure  / Primary Flow Total Pressure
Pi      = ProcessedData['P01/P02']
# Secondary Flow Total Pressure
P_s0    = ProcessedData['P02 [Pa]']
# Primary Flow Total Pressure
P_p0    = ProcessedData['P01 [Pa]']

item = [i1, i2, i3, i4, i5, i6, i7, i8, i9, i10, i11, i12]
pi   = np.zeros(12)
```

```
p_s0 = np.zeros(12)
p_p0 = np.zeros(12)
for j in range(12):
    pi[j]   = np.round(np.mean( Pi[item[j]]), 2)    # [-]
    p_s0[j] = np.round(np.mean(P_s0[item[j]]),2)    # [Pa]
    p_p0[j] = np.round(np.mean(P_p0[item[j]]),2)    # [Pa]

### Thermodynamics Parameters ###
cp      = 1.005e3;      # [J/(kg K)]
cv      = 0.718e3;      # [J/(kg K)]
R       = 287.058;      # [J/(kg K)]
gamma   = 1.40;         # [-]
###  Isentropic coefficients  ###
eta_p   = 0.98;         # [-]
eta_s   = 0.56;         # [-]
eta_py  = 0.78;         # [-]
eta_m   = 0.99;         # [-]
eta_d   = 0.70;         # [-]


### Geometry ###
# Convergent Primary Nozzle COnfiguration #
r_pt = ###;             # [m]
A_pt = ###;             # [m^2]
# Exit Section
r_e  = ###;             # [m]
A_e  = ###;             # [m^2]
# Hypothetical throat
r_y  = ###;             # [m]
A_y  = ###;             # [m^2]
# Outlet Diffuser
r_d  = ###;             # [m]
A_d  = ###;             # [m^2]

### Upstrema Condition ###
# Secondary Flow
T_s0 = 300;             # [K]
h_s0 = cp*T_s0          # [J/kg]
# Primary Flow
T_p0 = 300;             # [K]
h_p0 = cp*T_p0          # [J/kg]

### Not Uniform Poin Distribution ###
N = np.size(p_p0)
def f(b, p0, M):
    L = p0*b
    alpha = 0.4;
    csi = np.linspace(0.3, L**(1/alpha), M)
    return csi**alpha;

### Backward Condition ###
M = 30
xx1  = f(0.425, p_p0[ 1-1], M)
xx2  = f(0.460, p_p0[ 2-1], M)
xx3  = f(0.650, p_p0[ 3-1], M)
xx4  = f(0.750, p_p0[ 4-1], M)
xx5  = f(0.700, p_p0[ 5-1], M)
xx6  = f(0.700, p_p0[ 6-1], M)
xx7  = f(0.500, p_p0[ 7-1], M)
xx8  = f(0.550, p_p0[ 8-1], M)
xx9  = f(0.650, p_p0[ 9-1], M)
xx10 = f(0.700, p_p0[10-1], M)
```

```
xx11 = f(0.830, p_p0[11-1], M)
xx12 = f(0.920, p_p0[12-1], M)
p_c = np.array([[xx1], [xx2], [xx3], [xx4], [xx5], [xx6], [xx7], [xx8], [xx9
    ], [xx10], [xx11], [xx12]])

### Array Initialitation ###
ER      = np.zeros([N, M])
m_s     = np.zeros([N, M])
m_p     = np.zeros(N)
p_out   = np.zeros(N)

#### Thermodynamic Model ####
def T2( T1, p1, p2):     # Isentropic Relation
    T2 = T1*((p2/p1)**((gamma-1)/gamma))
    return T2;

def h( h1, h, eta):
    h = h1-eta*(h1-h)
    return h;

def rho_ph( p, h):
    rho_ph = (cp*p)/(R*h)
    return rho_ph;

# Primary Nozzle Throat Condition
def throat(p, p0, T0, eta):
    T   = T2( T0, p0, p)
    hi  = cp*T
    h0  = cp*T0
    h   = h0-eta*(h0-hi)
    rho = rho_ph(p, h)
    V   = np.sqrt(2*(h0-h))
    return T, h, rho, V;

# Flow Rate Maximization
def max_G( pt, pp0, T0, eta):
    T_p, h_p, rho_p, V_p = throat( pt, pp0, T0, eta)
    G = V_p*rho_p
    return -G;

# Exit Primary Nozzle Condition
def exit_nozzle( p, pp0, mp):
    Te   = T2( T_p0, pp0, p)
    he   = h( h_p0, cp*Te, eta_p)
    rhoe = rho_ph( p, he)
    return Te, he, rhoe;

# Finging Root: Velocity Exit Condition
def solve_exit( pe, pp0, mp, ht, Vt ):
    Te, he, rhoe = exit_nozzle(pe, pp0, mp)
    Ve1 = np.sqrt(2*(ht-he)+Vt*Vt)
    Ve2 = mp/(rhoe*A_e)
    return np.absolute((Ve2-Ve1)/Ve2);

# Hypothetical Throat Condition
def hypothetical_throat(py, Te, pe, he, Ve, mp, ps0):
    Tpy   = T2( Te, pe, py)
    hpyi  = cp*Tpy
    hpy   = he-eta_py*(he-hpyi)
    Vpy   = np.sqrt(2*(he-hpy)+Ve*Ve)
    rhopy = rho_ph( py, hpy)
    Apy   = mp/(rhopy*Vpy)
```

```
160     Asy    = A_y-Apy
161     Tsy    = T2( T_s0, ps0, py)
162     hsyi   = cp*Tsy
163     hsy    = h_s0-eta_s*(h_s0-hsyi)
164     rhosy  = rho_ph( py, hsy)
165     Vsy    = np.sqrt(2*(h_s0-hsy))
166     return Vsy, Vpy, Asy, Apy, rhosy, rhopy;
167
168 # Compound-chocking: beta function
169 def beta(py, data):
170     Te, pe, he, Ve, mp, ps0           = data
171     Vsy, Vpy, Asy, Apy, rhosy, rhopy = hypothetical_throat( py, Te, pe, he,
        Ve, mp, ps0)
172     asy = np.sqrt((gamma*py)/rhosy)
173     apy = np.sqrt((gamma*py)/rhopy)
174     Msy = Vsy/asy
175     Mpy = Vpy/apy
176     return np.absolute(py*((Apy/(rhopy*(Vpy**2)))*(1-(Mpy**2))+(Asy/(rhosy*(
        Vsy**2)))*(1-(Msy**2))));
177
178 # Mixing Section Condition
179 def mixing( pm, mp, ms, Vpy, Vsy, py):
180     Vm    = eta_m*((mp*Vpy+ms*Vsy+(py-pm)*A_y)/(mp+ms))
181     hm    =((mp*h_p0+ms*h_s0)/(mp+ms))-(Vm*Vm)/2
182     rhom = rho_ph( pm, hm)
183     return Vm, hm, rhom
184
185 def mixing_solve( pm, data):
186     mp, ms, Vpy, Vsy, py = data
187     Vm, hm, rhom          = mixing( pm, mp, ms, Vpy, Vsy, py)
188     return np.absolute((rhom*Vm*A_y)-(mp+ms));
189
190 # Downstream Shock Wave: Section 2
191 def second( rho2, pm, Vm, rhom):
192     V2 = rhom*Vm/rho2
193     h2 = h_m+((Vm*Vm)/2)-((V2*V2)/2)
194     p2 = (h2*rho2*R)/cp
195     return V2, p2, h2;
196
197 def second_solve( rho2, data):
198     pm, Vm, rhom = data
199     V2, p2, h2   = second( rho2, pm, Vm, rhom)
200     return np.absolute((rho2-(rhom*Vm*Vm+pm-p2)/(V2*V2))/rho2);
201
202 # Area Ratio Relation
203 def ARatio( M,data):
204     A_rat = data
205     AA    = (1/M)*(((2/(gamma+1))*(1+(M**2)*(gamma-1)/2))**((gamma+1)/(2*(
        gamma-1))))
206     return AA-A_rat;
207
208 # Case 1: Zero Outlet Diffuser Velocity
209 def shock_wave_neg( Vm, hm, rhom, pm):
210     Mm  = Vm/np.sqrt(gamma*pm/rhom)
211     pm0 = pm*((1+(Mm**2)*((gamma-1)/2))**(gamma/(gamma-1)))
212     if Mm>1:
213         p20        = pm0*(((((gamma+1)*(Mm**2))/((gamma-1)*(Mm**2)+2))**(
        gamma/(gamma-1)))*(((gamma+1)/(2*gamma*(Mm**2)-(gamma-1)))**(1/(gamma-1)
        )))
214         datar2     = [ pm, Vm, rhom]
215         rho2       = fsolve( second_solve, 1, args=datar2)
216         V2, p2, h2 = second( rho2, pm, Vm, rhom)
```

```
    else:
        p20 = pm0
        p2  = pm
        h2  = hm
        V2  = Vm

    hds = eta_d * V2 * V2 / 2 + h2
    pd  = p20
    return pd;


def off(py, data):
    Te, pe, he, Ve, mp, ps0, pc = data

    Vsy, Vpy, Asy, Apy, rhosy, rhopy = hypothetical_throat(py, Te, pe, he,
    Ve, mp, ps0)
    ms=rhosy*Asy*Vsy

    # Mixing region
    datapm=[ mp, ms, Vpy, Vsy, py ]
    pm=fsolve(mixing_solve, 1e4, datapm)
    Vm, hm, rhom = mixing( pm, mp, ms, Vpy, Vsy, py)
    pd, Md = shock_wave_diff(Vm, hm, rhom, pm)
    # pd = shock_wave_neg(Vm, hm, rhom, pm)

    return np.absolute((pd-pc)/pc);

# Case 2: Not Zero Outlet Diffuser Velocity
def shock_wave_diff( Vm, hm, rhom, pm):
    Mm  = Vm/np.sqrt(gamma*pm/rhom)
    pm0 = pm*((1+(Mm**2)*((gamma-1)/2))**(gamma/(gamma-1)))
    Tm  = pm/(rhom*R)
    Tm0 = Tm*(1+((gamma-1)/2)*(Mm**2))
    if Mm>1:
        M2  = np.sqrt(((gamma-1)*(Mm**2)+2)/((Mm**2)*gamma*2-(gamma-1)))
        p20 = pm0*(((((gamma+1)*(Mm**2))/((gamma-1)*(Mm**2)+2))**(gamma/(
    gamma-1)))*(((gamma+1)/(2*gamma*(Mm**2)-(gamma-1)))**(1/(gamma-1))))
        p2  = p20*((1+((gamma-1)/2)*(M2**2))**(-gamma/(gamma-1)))
        T20 = Tm0
        T2  = T20*(((2*gamma*M2*M2)-(gamma-1))*((gamma-1)*M2*M2+2))/((gamma
    +1)*(gamma+1)*M2*M2)
        h2  = cp*T2
        V2  = M2*np.sqrt(gamma*R*T2)
    else:
        M2  = Mm
        p20 = pm0
        p2  = pm
        h2  = hm
        V2  = Vm
        T20 = Tm0

    A2ratiostar = (1/M2)*(((2/(gamma+1))*(1+(M2**2)*(gamma-1)/2))**((gamma
    +1)/(2*(gamma-1))))
    Adratiostar = (A_d/A_y)*(A2ratiostar)
    Md  = fsolve( ARatio, 0.05, args=Adratiostar)
    pd0 = p20
    pd  = pd0*((1+((gamma-1)/2)*(Md**2))**(-gamma/(gamma-1)))
    return pd, Md;



for i in range(N):
```

```
    # Primary Nozzle
    p_t, G_p, ierr, _     = opt.fminbound( max_G, 2000, p_p0[i], args=(p_p0[i
    ], T_p0, eta_p), full_output=True)
    if ierr != 0:
        print(" Pimary Nozzle Throat not converged.")
    m_p[i] = -G_p*A_pt
    T_t, h_t, rho_t, V_t = throat( p_t, p_p0[i], T_p0, eta_p)

    # Primary Nozzle Exit
    data_pe          = [p_p0[i], m_p[i], h_t, V_t]
    p_e, _, _, _     = opt.fminbound(solve_exit, p_t, p_p0[i], args=(p_p0[i],
     m_p[i], h_t, V_t), full_output=True)
    T_e, h_e, rho_e = exit_nozzle(p_e, p_p0[i], m_p[i])
    V_e              = m_p[i]/(rho_e*A_e)

    ###### Fabri-choking criterion #####
    p_y, G_s, ierr, _ = opt.fminbound(max_G, 2000, p_s0[i], args=(p_s0[i],
    T_s0, eta_s), full_output=True)
    if ierr != 0:
        print(" Hypothetical  Throat not converged.")
    V_sy, V_py, A_sy, A_py, rho_sy, rho_py = hypothetical_throat(p_y, T_e,
    p_e, h_e, V_e, m_p[i], p_s0[i])
    m_s[i,0] = rho_sy*A_sy*V_sy

    #### Compound-choking criterion ####
    # data_py=[ T_e, p_e, h_e, V_e, m_p[i], p_s0[i] ]
    # p_y=fsolve(beta, 1e4, data_py)
    # V_sy, V_py, A_sy, A_py, rho_sy, rho_py = hypothetical_throat(p_y, T_e,
     p_e, h_e, V_e, m_p[i], p_s0[i] )
    # m_s[i,0]=rho_sy*A_sy*V_sy

    # Mixing Section condition
    data_pm     = [ m_p[i], m_s[i,0], V_py, V_sy, p_y ]
    p_m         = fsolve( mixing_solve, 1e4, data_pm)
    V_m, h_m, rho_m = mixing( p_m, m_p[i], m_s[i,0], V_py, V_sy, p_y)
    p_out, M_d  = shock_wave_diff( V_m, h_m, rho_m, p_m)
    # p_out      = shock_wave_neg( V_m, h_m, rho_m, p_m)
    M_m = V_m/np.sqrt(gamma*p_m/rho_m)
    M_2 = np.sqrt(((gamma-1)*(M_m**2)+2)/((M_m**2)*gamma*2-(gamma-1)))

    for k in range(M):
        if p_c[ i, 0, k]>p_out:
            data_off    = [ T_e, p_e, h_e, V_e, m_p[i], p_s0[i], p_c[i,0,k] ]
            p_yy        = fsolve(off, 1e4, data_off)
            # V_sy_off, V_py_off, A_sy_off, A_py_off, rho_sy_off, rho_py_off
     = hypothetical_throat(p_yy, T_e, p_e, h_e, V_e, m_p[i])
            # m_s[i,k] = rho_sy_off*A_sy_off*V_sy_off
            T_py_off    = T2(T_e, p_e, p_yy)
            h_pyi_off   = cp*T_py_off
            h_py_off    = h_e-eta_py*(h_e-h_pyi_off);
            V_py_off    = np.sqrt(2*(h_e-h_py_off)+V_e**2)
            rho_py_off  = rho_ph(p_yy, h_py_off)
            A_py_off    = m_p[i]/(rho_py_off*V_py_off)
            A_sy_off    = A_y-A_py_off;
            T_sy_off    = T2( T_s0, p_s0[i], p_yy);
            h_syi_off   = cp*T_sy_off;
            h_sy_off    = h_s0-eta_s*(h_s0-h_syi_off);
            rho_sy_off  = rho_ph( p_yy, h_sy_off)
            V_sy_off    = np.sqrt(2*(h_s0-h_sy_off))
            m_s[i,k]    = rho_sy_off*A_sy_off*V_sy_off
        else:
            m_s[i,k]    = m_s[i,0]
```

```
331         ER[i,k] = m_s[i,k]/m_p[i]
```

Listing A.1: Metsue's 0D thermodynamic model with experimental data sets for convergent primary nozzle configuration

Below are the flowcharts underlying the algorithms for the implementation of the thermodynamic model used in this study for the two different criteria used.

A.2 On-Design Model

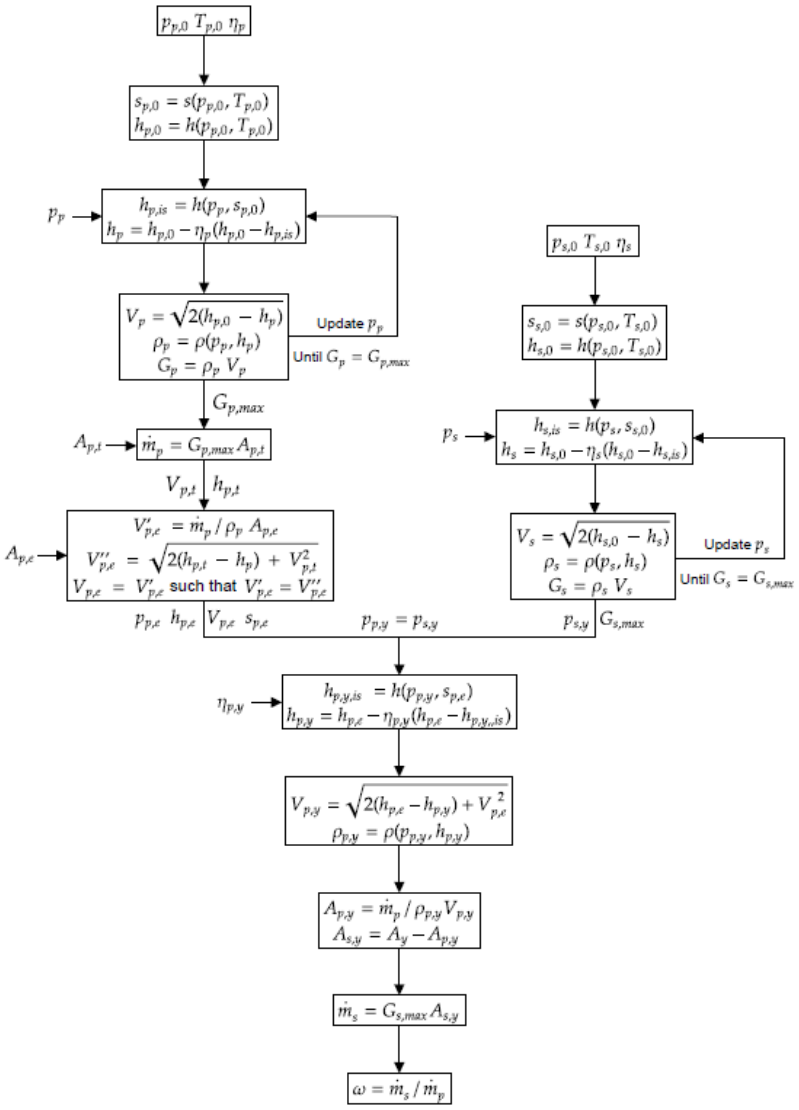

Figure A.1: Flowchart of the model for on-design operation using the Fabri-choking criterion.

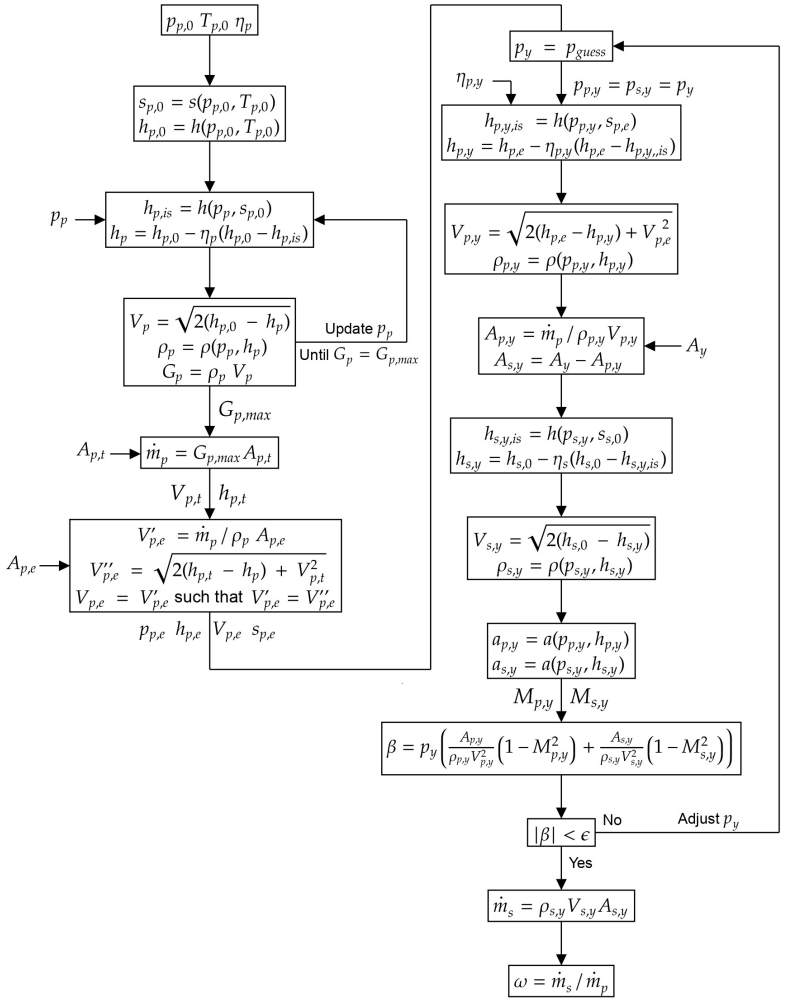

Figure A.2: Flowchart of the model for on-design operation using the compound-choking criterion.

A.3 Off-Design Model

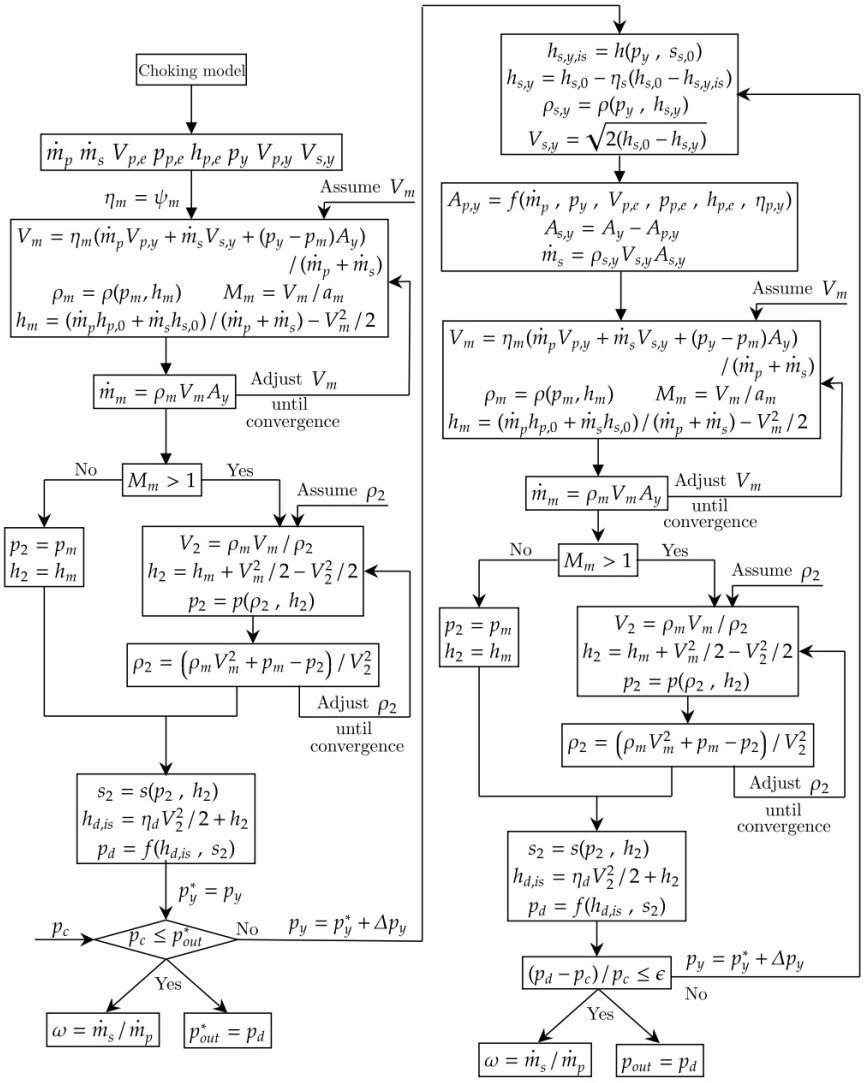

Figure A.3: Flowchart of the model for off-design operation conditions.

A.4 Velocity Outlet Diffuser

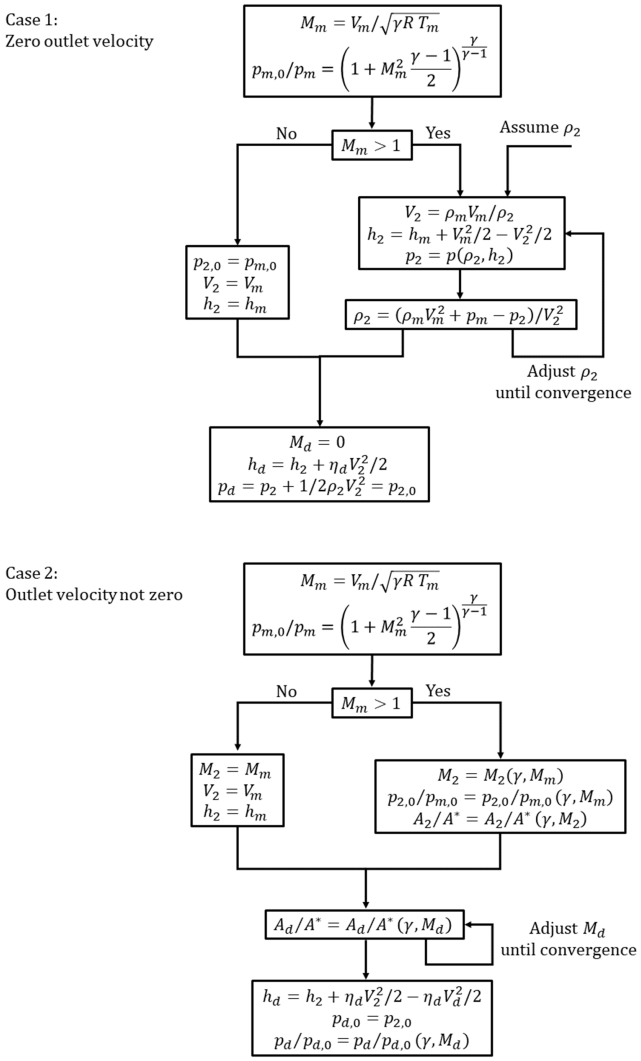

Figure A.4: Flowchart of "Case 1" and "Case 2" for the diffuser outlet velocity.

Appendix B

Experimental Study

B.1 Calibration Curve Pressure Transducers.

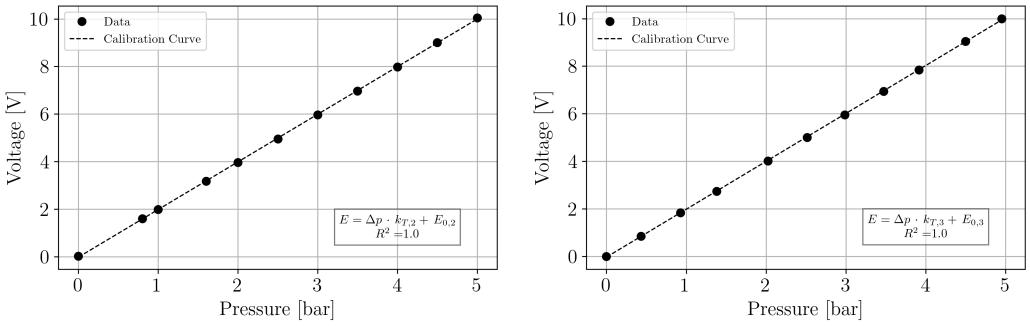

(a) (b)

Figure B.1: Calibration Curve: (a) "Validyne 2"; (b) "Valydine 3".

B.2 Error Propagation in the measuring chain.

Below are the mathematical steps for deriving the formulas for evaluating error propagation in the measurement chain.

$$\frac{\partial p_0}{\partial p} = \frac{\partial}{\partial p}\left\{ p\left[1 + \frac{\gamma - 1}{2}\left(\frac{\sqrt{R}}{S\sqrt{\gamma}}\,\frac{\dot{m}\sqrt{T}}{p}\right)^2\right]^{\frac{\gamma}{\gamma-1}}\right\}$$

Defining the groups of constants with respect to the static pressure:

$$A = \frac{\gamma - 1}{2} \qquad B = \frac{\sqrt{R}}{S\sqrt{\gamma}} \qquad C = \frac{\gamma}{\gamma - 1}$$

Rewriting the expression:

$$\frac{\partial p_0}{\partial p} = \frac{\partial}{\partial p}\left\{ p\left[1 + A\left(\frac{B\sqrt{T}\dot{m}}{p}\right)^2\right]^C\right\} = \frac{\partial p_0}{\partial p}\left\{ p\left[1 + A\frac{TB^2\dot{m}^2}{p^2}\right]^C\right\}$$

Use the product rule:

$$\frac{\partial p_0}{\partial p} = \left[1 + A\frac{TB^2\dot{m}^2}{p^2}\right]^C - \frac{2ACTB^2\dot{m}^2}{p^2}\left(1 + A\frac{TB^2\dot{m}^2}{p^2}\right)^{C-1}$$

$$\frac{\partial p_0}{\partial p} = \left[1 + \frac{\gamma - 1}{2}\frac{TR\,\dot{m}^2}{\gamma p^2 S^2}\right]^{\frac{\gamma}{\gamma-1}} - \frac{RT\dot{m}^2}{S^2p^2}\left(1 + \frac{\gamma - 1}{2}\frac{TR\,\dot{m}^2}{\gamma p^2 S^2}\right)^{\frac{1}{\gamma-1}}$$

Similarly for the static temperature:

$$\frac{\partial p_0}{\partial T} = \frac{CAB^2\dot{m}^2}{p}\left[1 + \frac{AB^2T\dot{m}^2}{p^2}\right]^{C-1}$$

$$\frac{\partial p_0}{\partial T} = \frac{R\dot{m}^2}{2S^2p}\left[1 + \frac{\gamma - 1}{2}\frac{TR\,\dot{m}^2}{\gamma p^2 S^2}\right]^{\frac{1}{\gamma-1}}$$

And mass flow rate:

$$\frac{\partial p_0}{\partial \dot{m}} = \frac{2CAB^2T}{p}\dot{m}\left[1 + \frac{AB^2T\dot{m}^2}{p^2}\right]^{C-1}$$

$$\frac{\partial p_0}{\partial \dot{m}} = \frac{R\dot{m}}{S^2p}\left[1 + \frac{\gamma - 1}{2}\frac{TR\,\dot{m}^2}{\gamma p^2 S^2}\right]^{\frac{1}{\gamma-1}}$$

These terms contribute to the uncertainty of the total pressure measurement, δp_0, which in turn accumulates in the error on the additional measures of interest.
The partial derivatives of the additional groups with respect to the quantities affected by uncertainty involved are reported:

$$\frac{\partial \Pi}{\partial p_{s,0}} = \frac{1}{p_{p,0}} \qquad \frac{\partial \Pi}{\partial p_{p,0}} = -\frac{p_{s,0}}{p_{p,0}^2}$$

$$\frac{\partial(p_b/p_{p,0})}{\partial p_b} = \frac{1}{p_{p,0}} \qquad \frac{\partial(p_b/p_{p,0})}{\partial p_{p,0}} = -\frac{p_b}{p_{p,0}^2}$$

$$\frac{\partial \omega}{\partial \dot{m}_s} = \frac{1}{\dot{m}_p} \qquad \frac{\partial \omega}{\partial \dot{m}_p} = -\frac{\dot{m}_s}{\dot{m}_p^2}$$

Starting from these relationships, the formulas are built to quantitatively evaluate the propagation of the error on the measurements of interest in the measurement chain.

B.3 Normalized Mass Flow Rate

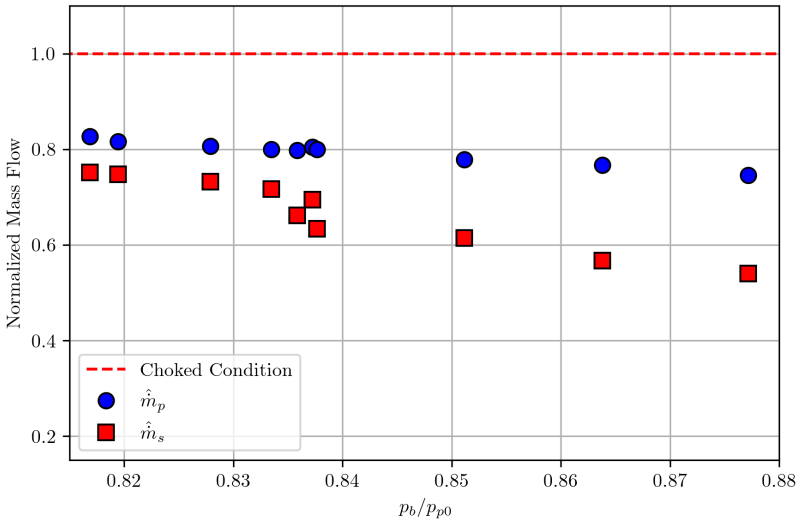

Figure B.2: Normalized Mass Flows for $p_{s,0}/p_{p,0} = 0.90$.